The electronic structure and magnetic interactions in the mixed transition-metal oxide La(Co,Ni)O_3 studied by x-ray absorption spectroscopies

Zur Erlangung des akademischen Grades eines

DOKTORS DER NATURWISSENSCHAFTEN

von der Fakultät für Physik des

Karlsruher Instituts für Technologie (KIT)

genehmigte

DISSERTATION

von

Meng-Jie Huang, MSc

aus Taipei

Tag der mündlichen Prüfung: 11.11.2016

Referent: Prof. Dr. Hilbert von Löhneysen

Korreferent: Prof. Dr. Matthieu Le Tacon

Abstract

Transition-metal oxides have attracted a lot of attention because they exhibit a variety of intriguing physical properties. Among the transition-metal oxides, $LaCoO_3$ is a very special compound which shows different spin states and spin-state transitions. Further, the physical properties can be controlled by changing temperature, replacement of rare-earth element, electron- or hole-doping, or by applying strain.

The ground state of $LaCoO_3$ is a non-magnetic insulator because the lowest energy configuration is $t_{2g}^{6}e_{g}^{0}$ ($S = 0$). However, the partial substitution of Co by Ni in $La(Co,Ni)O_3$ (LCNO) will induce a ferromagnetic behavior. A number of models have been proposed for explaining the nature of the magnetic behavior in the past decades, but it is still a puzzle.

In order to understand the origin of the ferromagnetism in $La(Co,Ni)O_3$, I have studied the electronic structure and magnetic interaction in this compound in a very direct way: by using x-ray absorption (XAS) and x-ray magnetic circular dichroism (XMCD) along with multiplet simulations. Samples were synthesized by the sol-gel method and structurally and magnetically characterized by XRD and SQUID.

XAS clearly indicates a mixed-valence state for both Co and Ni, with both valences increasing monotonously with Ni content, x. While the gradual spin-state transition of Co^{3+} from low-spin (LS) to high-spin (HS) is preserved for low x it is suppressed in the high Ni-content samples. Regarding the spin configuration of Ni we find it stabilized in a “mixed” spin state, unlike the purely LS state of Ni in $LaNiO_3$. XMCD identifies the element-specific contributions to the magnetic moment and interactions. In particular, we find that it must be the coexistence of the HS state in both Co^{3+} and Ni^{3+} that induces t_{2g}-based ferromagnetic interaction via a “double-exchange-like” mechanism. Other species carrying a high spin moment were found to

be present but do not contribute to ferromagnetism in LCNO. Many aspects of these findings are in contrast to literature.

Zusammenfassung

Übergangsmetall-Oxide werden nach wie vor äußerst intensiv untersucht, denn sie zeigen ein breites Spektrum sehr ungewöhnlicher physikalischer Eigenschaften. Aufgrund seiner verschiedenartigen Spinzustände und Spinübergänge ist $LaCoO_3$ ein besonders interessantes Übergangsmetalloxid. Seine Eigenschaften können darüber hinaus durch Temperature, Substitution auf dem Seltenen-Erd-Platz (La), Elektronen- oder Lochdotierung sowie durch Verspannung verändert werden.

Im Grundzustand ist $LaCoO_3$ ein nichtmagnetischer Isolator, denn die energetisch tiefstliegende Elektronenkonfiguration ist $t_{2g}^{6}e_{g}^{0}$ mit einem Gesamtspin $S = 0$. Ersetzt man Co in $La(Co,Ni)O_3$ (LCNO) jedoch zum Teil mit Nickel, so wird dies ferromagnetisches Verhalten hervorrufen. Eine ganze Reihe von Modellen für den Magnetismus in LCNO wurde in den vergangenen Jahrzehnten vorgeschlagen – eine Klärung steht jedoch weiterhin aus.

Um den Grund für den Ferromagneitmus in $La(Co,Ni)O_3$ zu verstehen, habe ich die elektronische Struktur und die magnetische Wechselwirkung in diesen Substanzen auf sehr direkte Weise untersucht: nämlich mit Röntgenabsorption (XAS) und mit Röntgen-Zirkulardichroismus (XMCD), ergänzt durch Multiplettrechnungen. Die Proben wurden mittels der Sol-Gel-Methode synthetisiert und ihre Struktur und der Magnetismus mit Röntgenbeugung und SQUID charakterisiert.

XAS findet klare Hinweise auf einen gemischtvalenten Zustand für Co ebenso wie für Ni; beide Valenzen wachsen mit steigendem Nickelgehalt x monoton an. Während der allmähliche Spinübergang von Co^{3+} von einem Niedrigspin-Zustand (LS) hin zu einem Hochspin-Zustand (HS) für geringe Dotierungsgrade x erhalten bleibt, wird er bei den Proben mit hohem Nickelgehalt unterdrückt. Für Ni

stellt sich eine stabile “gemischte” Spinkonfiguration heraus – im Gegensatz zu $LaNiO_3$, wo Ni sich vollständig in einem LS-Zustand befindet. Mittels XMCD wurden die elementspezifischen Komponenten des gesamten magnetischen Moments sowie der magnetischen Wechselwirkungen bestimmt. Insbesondere finden wir, dass es die Koexistenz des HS-Zustandes sowohl in Co^{3+} als auch in Ni^{3+} sein muß, die zu der verantwortlichen ferromagnetischen Wechselwirkung führt; diese findet zwischen t_{2g}-Orbitalen und mittels eines Mechanismus statt, der dem Doppelaustausch sehr ähnlich ist. Weitere Spezies mit hohem Spinmoment wurden zwar beobachtet, tragen jedoch nicht zum Ferromagnetismus in LCNO bei. Viele dieser Ergebnisse stehen im Gegensatz zu bisher publizierten Schlußfolgerungen.

Contents

Chapter 1

Introduction

1.1 Transition-metal oxides

Transition-metal (TM) oxides are a very interesting branch of solid state physics, as they show a variety of intriguing physical properties such as colossal magnetoresistance, ordering of spin, charge and orbitals, thermally driven spin-state transitions, metal-insulator (MI) transitions, and high-T_C superconductivity. This spectacular behavior can be attributed to the strong interplay between the spin, orbital, charge, and lattice degrees of freedom. Among transition-metal oxides, materials with perovskite ABO_3 structure (A: rare earth element; B: transition metal) continue to gain intense attention. The perovskite materials cover a very wide range from good metals to strong insulators; some of them even show metal-insulator transitions. They also exhibit a variety of magnetic interactions, such as ferro-, ferri-, antiferro-, para- or diamagnetic behavior. Change of temperature or pressure, electron- or hole-doping or applying a strain are functional ways of manipulating the physical properties of ABO_3. The ABO_3 structure in cubic symmetry is shown in Fig. 1.1. In this structure, the transition-metal ion occupies the central B-site and is surrounded by six O^{2-} anions. The understanding of the local electronic structure has been assisted greatly by the Zaanen-Sawatzky-Allen (ZSA) phase diagram [1], which will be discussed in detail in Chapter 3. A very special compound which shows different spin states and spin-state transitions is the cobaltate $LaCoO_3$ (LCO). In the ZSA diagram, LCO turns out to be located in the region of highly mixed character between Mott-Hubbard insulators and charge-transfer insulators. This mixed character causes interesting spin-state transitions as well as transport and magnetic phase transitions in $LaCoO_3$ as a func-

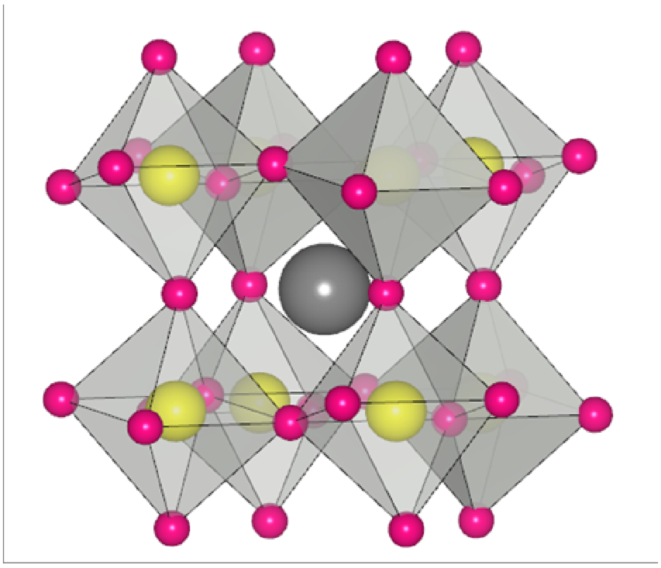

Figure 1.1: Perovskite-related ABO_3 structure in cubic symmetry. Yellow spheres represent the transition metal at the central B sites of BO_6 octahedra, pink spheres represent oxygen and the gray spheres represents the rare-earth element at the A sites.

tion of temperature or of doping by charge carriers [2-13]. So, one can expect that the physical properties will change if we replace the Co ion by another transition metal. In this thesis, I have investigated the local electronic structure and magnetic interaction as Co ions are replaced by Ni ions.

1.1.1 $LaCoO_3$

To be a little more specific, the temperature-dependent spin-state transition and magnetic behavior in $LaCoO_3$ (LCO) is going to be presented in this section. The Co ion in LCO has a valence of +3 ($3d^6$ configuration), and is in O_h symmetry. The ground state is a non-magnetic insulator because the lowest energy configuration is $t_{2g}{}^6 e_g{}^0$ with total spin $S = 0$. For a $3d^6$ configuration in O_h symmetry, three different spin states are, in principle, allowed: a low-spin state (LS, $t_{2g}{}^6 e_g{}^0$) with $S = 0$, an intermediate-spin state (IS, $t_{2g}{}^5 e_g{}^1$) with $S = 1$, and a high-spin state (HS, $t_{2g}{}^4 e_g{}^2$) with $S = 2$. A most interesting question is: why does LCO undergo a spin-state transition so easily? In O_h symmetry, the ground state will be either LS or HS depending on which energy dominates: the crystal-field energy 10 D_q or the exchange energy J_{ex}. Figure 1.2 (a) and (b) shows these two different situations: $10D_q > J_{ex}$ and $10D_q < J_{ex}$. In the case of $10D_q > J_{ex}$, the LS state has the lowest energy. On the other hand, the HS state will be favored if $10D_q < J_{ex}$. In this respect, LCO is very special because its $10D_q$ is almost equal to J_{ex}. This is why even small changes, like temperature changes, can drive a spin-state transition in this compound. This situation is shown in Fig. 1.2 (c). So one

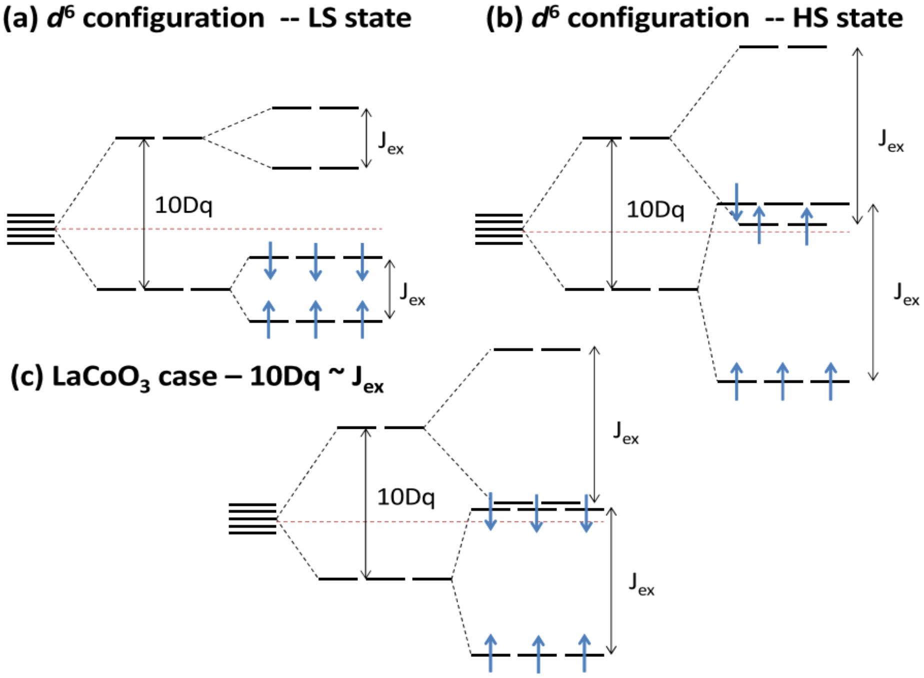

Figure 1.2: (a) In the case of $J_{ex} < 10D_q$, a d^6 system favors the low spin state (LS). (b) When $J_{ex} > 10D_q$, d^6 system is stable in high spin state (HS). (c) In $LaCoO_3$, the spin state can be easily switched owing to comparable values for J_{ex} and $10D_q$.

can easily manipulate the spin state of Co^{3+} by changing temperature, applying strain on LCO, doping by other ions at the A site or B site *etc.* [13] Furthermore, $LaCoO_3$ is a nonmagnetic, small-gap insulator at low temperature because Co^{3+} LS dominates [13-15]. With increasing temperature, the fraction of HS gradually increases, and LCO becomes paramagnetic above 50 K. An insulator-metal transition appears at 500 K, possibly due to a further spin-state transition from HS-LS to IS. In recent years, ferromagnetic ordering in LCO has been observed below about 85 K in strained epitaxial thin films [15-17], nano-particles [18] as well as nano-wires [19]. For the epitaxial films at least [15], the HS-LS spin-state transition (for decreasing temperature) was shown to be more or less suppressed, and the HS fraction stays high even for low temperature and enables ferromagnetism. The suppression of the HS-LS transition results from the increase of the Co-O bond length (decreasing $10D_q$). All this shows that altering the spin state of Co^{3+} in the LCO system can control the transport and magnetic properties.

1.1.2 $LaNiO_3$

$LaNiO_3$ (LNO) is the only compound among the nickelate $R$$NiO_3$ family (R: rare earth) which shows a paramagnetic metallic phase with $R\bar{3}c$ structure at all measured temperatures [20, 21]. In the literature, it has been reported that the metal-insulator transition temperature is directly connected to the Ni-O-Ni bond angle [22-29]. All members of the $R$$NiO_3$ except $LaNiO_3$ exhibit a metal-insulator transition (MIT) in the temperature range from 100 K ($PrNiO_3$) to 600 K ($YNiO_3$). The phase diagram is shown in Fig. 1.3. In this figure, a red line depicts the boundary between the metallic and the insulating phase and the inset sketches the local bond environment of two adjacent NiO_6 groups in the metallic

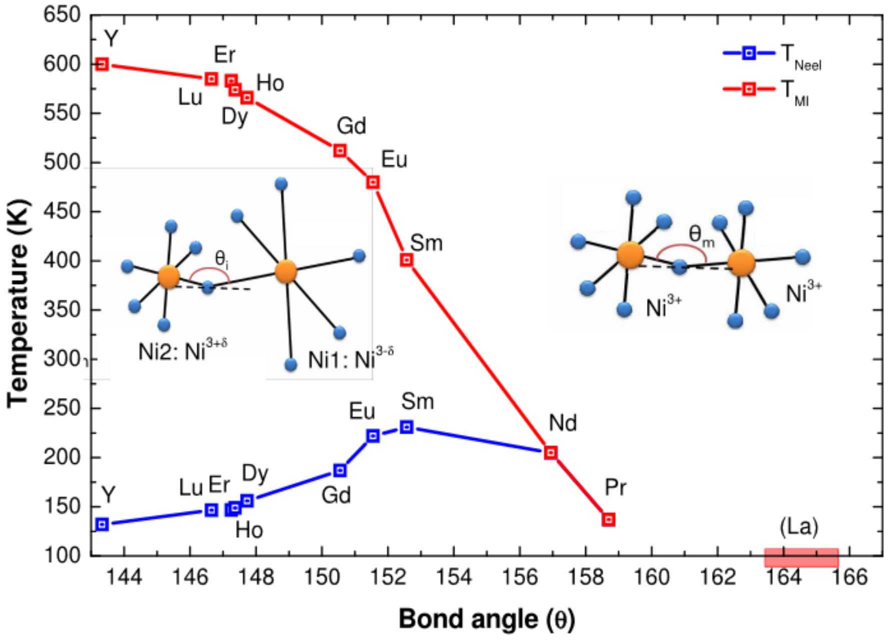

Figure 1.3: Resistive and magnetic transitions as a function of average bond angle ⟨Ni-O-Ni⟩. Reproduced from Ref. [28]. The range of the bond angle observed for La(Co,Ni)O_3 is also indicated (see Chapter 4).

and the insulating phase. The conduction band in LNO is formed by the hybridization between a Ni^{3+} e_g orbital and an O $2p$ orbital. When the rare-earth element R is replaced, it is plausible that the average Ni-O-Ni bond angle (θ) decreases as the size of the R^{3+} ion decreases. A smaller Ni-O-Ni bond angle will reduce the bandwidth resulting in an insulating phase. Based on neutron diffraction, synchrotron diffraction, and x-ray spectroscopies measurements [30-33], $R\mathrm{NiO_3}$ shows a charge-ordering (charge-disproportionation) behavior in the insulating phase. There, the energy gap is defined by the charge-transfer energy between the occupied O-$2p$ valence band and unoccupied Ni-$3d$ conduction band.

1.1.3 $\mathbf{LaCo_xNi_{1-x}O_3}$

Since the physical properties can be controlled in the LCO and the LNO system by changing temperature, replacement of rare-earth element, electron- or hole-doping, or by applying strain, one would expect that partial substitution of Co by Ni in LCO should affect both the magnetism and the transport properties. In fact, the mixed transition-metal perovskite $LaCo_xNi_{1-x}O_3$ (LCNO) has drawn much attention because the substitution of Co by Ni induces ferromagnetism, even though both parent compounds are not ferromagnetic [34]. Further intriguing behavior similar to the $La_{1-x}Sr_xCoO_3$ family of compounds [10-12, 35-37] is also found in the LCNO system. According to temperature-dependent resistance measurements, a metal-insulator transition has been observed around $x = 0.4$ in the LCNO system [38, 39]. Further, “glassy” ferromagnetism and giant magnetoresistance have been reported around the metal-insulator transition [38, 39, 41-46]. There are already a lot of efforts on investigating the local electronic structure and magnetic interaction in the LCNO system. However, two main issues are still not clear so far: the evolution of the valence state and the spin state of Co and Ni in this series, and the character of the magnetic interaction. A number of models have been proposed for explaining the mechanism of transport and magnetic behavior in the past decades, but it is still a puzzle. In order to solve this puzzle, I have studied the electronic structure and magnetic interaction in the LCNO system in a very direct way: by using x-ray absorption and x-ray magnetic circular dichroism.

1.2 Scientific goals and outline of this thesis

In the mixed transition-metal oxide family $\mathrm{LaCo}_x\mathrm{Ni}_{1-x}\mathrm{O}_3$, both end members (parent compounds) are nonmagnetic. Ferromagnetism can be very easily induced in LaCoO_3 even by applying only a little strain. Therefore, it will be very interesting to study the magnetic properties when Co ions are partially replaced by Ni ions in the LCO compound. Previous works have reported that ferromagnetism can be induced in the LCNO system as mentioned above, but the origin of the ferromagnetism is still unclear. Since one already knows that a sufficiently high fraction of Co^{3+} HS can induce ferromagnetic ordering at low temperature in the LCO compound, the ferromagnetism in the LCNO system may perhaps also be attributed to a similar reason: the fraction of Co^{3+} HS in LCNO may be high enough to support ferromagnetism. In order to solve this question, the local electronic structure and the ferromagnetic interaction of the mixed transition-metal oxide $\mathrm{LaCo}_{1-x}\mathrm{Ni}_x\mathrm{O}_3$ has been investigated by x-ray absorption spectroscopies.

This thesis is organized as follows: First, we introduce the technique of x-ray absorption spectroscopy and x-ray magnetic circular dichroism in Chapter 2. Then, Chapter 3 covers the theoretical method of multiplet calculations. Chapter 4 to Chapter 6 present and discuss the experimental results of $\mathrm{LaCo}_{1-x}\mathrm{Ni}_x\mathrm{O}_3$. Finally, in Chapter 7, the conclusion and summary as well as possible future directions are given.

Chapter 2

Experiments

The concepts of x-ray absorption spectroscopy (XAS) and x-ray magnetic circular dichroism (XMCD) are presented in this chapter. They are very useful tools to probe the local electronic and the ferromagnetic properties of materials. All XAS and XMCD measurements were performed at IFP's WERA beamline at the ANKA synchrotron light source.

2.1 ANKA synchrotron facility

A synchrotron radiation facility mainly contains five components: electron gun, linear accelerator (LINAC), booster ring, storage ring and beamline. These parts are indicated in Fig. 2.1. The electron gun produces the electron beam, and the electron beam is accelerated by the LINAC. The accelerated electron beam next enters the booster ring for increasing the energy to a highly relativistic value. Finally, the electron beam is stored in the storage ring, where it is maintained on a closed path for many hours. In order to keep the electron beam circulating, an array of bending magnets is used, each forcing the electron path to a sector of a circle. In such curves, the electrons experience a velocity change (acceleration), causing them to emit synchrotron radiation in the tangential direction. Figure 2.2 (a) shows the schematic of the synchrotron radiation produced by a bending magnet.

The synchrotron facility ANKA has been put into operation at the Forschungszentrum Karlsruhe (Karlsruhe Research Center; now: Campus Nord, Karlsruhe Institute of Technology, KIT) in 2003. ANKA is an improved 2nd-generation synchrotron with a beam energy of 2.5 GeV. The accelerator complex consists of a 53 MeV microtron as a preaccelerator, a 500 MeV booster synchrotron and a 2.5 GeV storage ring. The

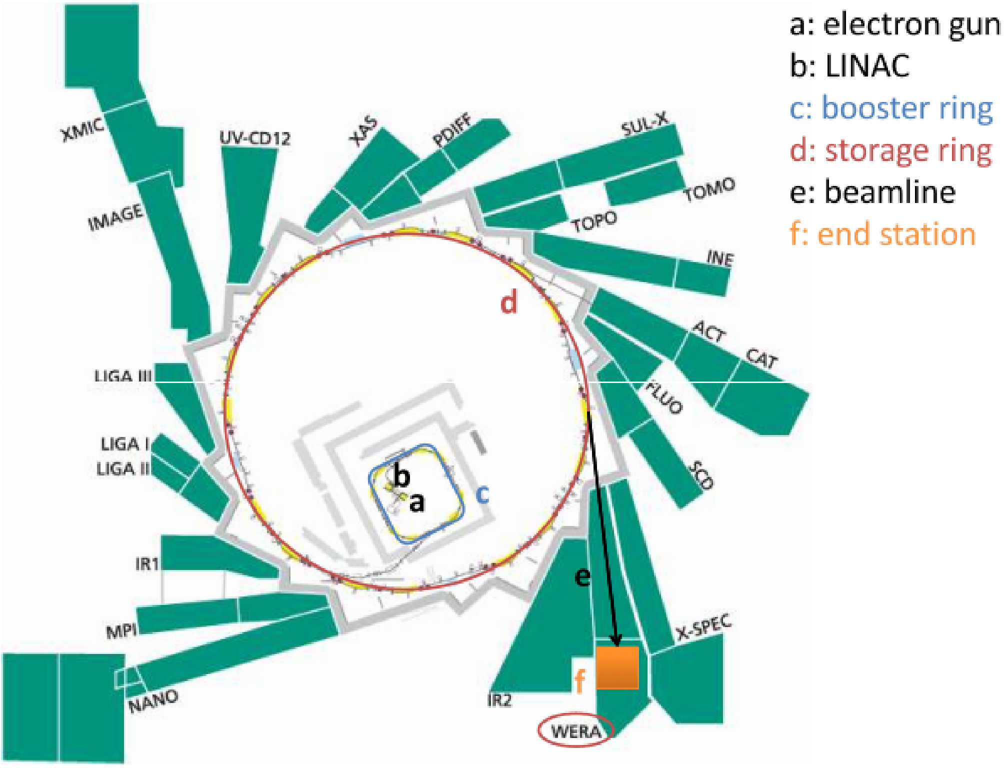

Figure 2.1: Schematic layout of the ANKA synchrotron at KIT, from Ref. [47]. The major parts of the synchrotron facility are indicated: (a) electron gun, (b) LINAC, (c) booster ring, (d) storage ring, (e) beamline, and (f) end station.

storage ring has a circumference of 110.4 m, and there are twenty-two end-stations which cover a wide range of functionalities. The injector has a repetition rate of 1 Hz and the booster current is about 5 mA. Injection into the storage ring is two times a day; a nominal current of up to 200 mA is accumulated in the storage ring at 500 MeV and then ramped to 2.5 GeV. The lifetime of the stored beam at 2.5 GeV is normally 16 hours at a ring current of 150 mA.

2.1.1 Linearly and circularly polarized light

The polarization of the synchrotron beam depends on the "line of sight", the emission direction relative to the ring plane [48]. The different lines

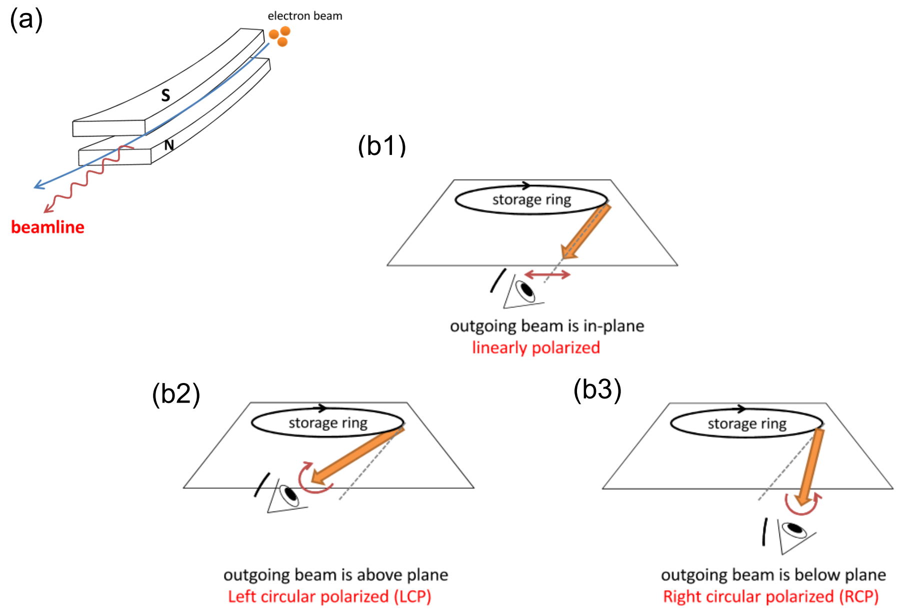

Figure 2.2: (a): Sketch of a bending magnet. The traveling direction of electron beam (blue line) is bent by the bending magnet, leading to the emission of synchrotron radiation. (b1), (b2) and (b3) shows the scheme of linear, left and right polarized light, respectively. This plot is reproduced from Ref. [48].

of sight which correspond to different polarizations are shown in Fig. 2.2 (b). The synchrotron beam is linearly polarized if it is emitted within the electron orbit plane (Fig. 2.2 (b1)). The electric field vector $\overrightarrow{E}$ of the synchrotron beam appears to oscillate in the horizontal plane. On the other hand, if one sees the outgoing beam from above the plane, the electrons will move in an elliptical orbit in a clockwise manner. Relative to the direction of propagation of the synchrotron beam, the $\overrightarrow{E}$ vector will rotate counterclockwise. This is the left circularly polarized (LCP) light, and the angular momentum is $-\hbar$. The opposite situation is that one observes the synchrotron beam from below the electron orbit. In this case, one obtains right circularly polarized (RCP) light with the angular momentum $\hbar$.

2.1.2 Beamline WERA

The WERA[1] beamline at ANKA is especially designed for soft x-ray experiments in the energy range of 100 to 1500 eV. The layout of the WERA beamline is shown in Fig. 2.3. This beamline is owned and operated by the Institut für Festkörperphysik (Institute of Solid-State Physics), KIT. The WERA beamline possesses multipurpose end-stations for important electron spectroscopies and spectromicroscopy, including PES, ARPES, NEXAFS, PEEM and XMCD. It facilitates combinatory studies of the electronic and magnetic structure which have particular promise for strongly correlated, thin-film, and nanoscale materials. All end-stations and the beamline are kept in ultra-high vacuum (UHV) with a base pressure of 10^{-10} mbar. The beam is produced by a bending magnet, and radiation with linear or circular polarization can be selected by moving the height of a polarization aperture. With typical settings, the degree of polarization is typically 95% for linear polarization and about 79%, 82%, and 83% for circular polarization at the O-K, Co-$L_{2,3}$, and Ni-$L_{2,3}$ edges.

The monochromator provides the well-defined and scanable photon energies necessary for x-ray absorption experiments. At WERA, a spherical-grating design [49] is used. Three different gratings (350, 700, and 1400 lines/mm) cover the soft x-ray range 100 - 1500 eV. The typical energy resolution is $\Delta E/E \sim 2\times10^{-4}$, with a maximum $\Delta E/E < 10^{-4}$ verified at the N-K edge. The energy resolution for different x-ray energies can be optimized by moving the entrance and exit slit.

In this thesis, all element-specific absorption spectroscopies were performed at the NEXAFS and XMCD chambers (see Fig. 2.3). The energy resolution for O-K, Co-L_3, and Ni-L_3 were set to 0.15 eV, 0.25 eV and 0.3 eV, respectively. The samples can be cooled down to ~20 K and ~10 K at the NEXAFS and XMCD chamber, respectively. The XMCD chamber possesses a fast-ramp magnet and was built by the MPI-IS group[2]. This fast-ramp magnet allows us to apply ± 7 T on the samples with a ramp rate of up to 1.5 T/s.

---

[1] WERA is an abbreviation for 'Weichröntgen-Analytik-Anlage', soft x-ray analytics facility.

[2] PD Dr. E. Goering and his group, Max-Planck institute for Intelligent Systems, Stuttgart.

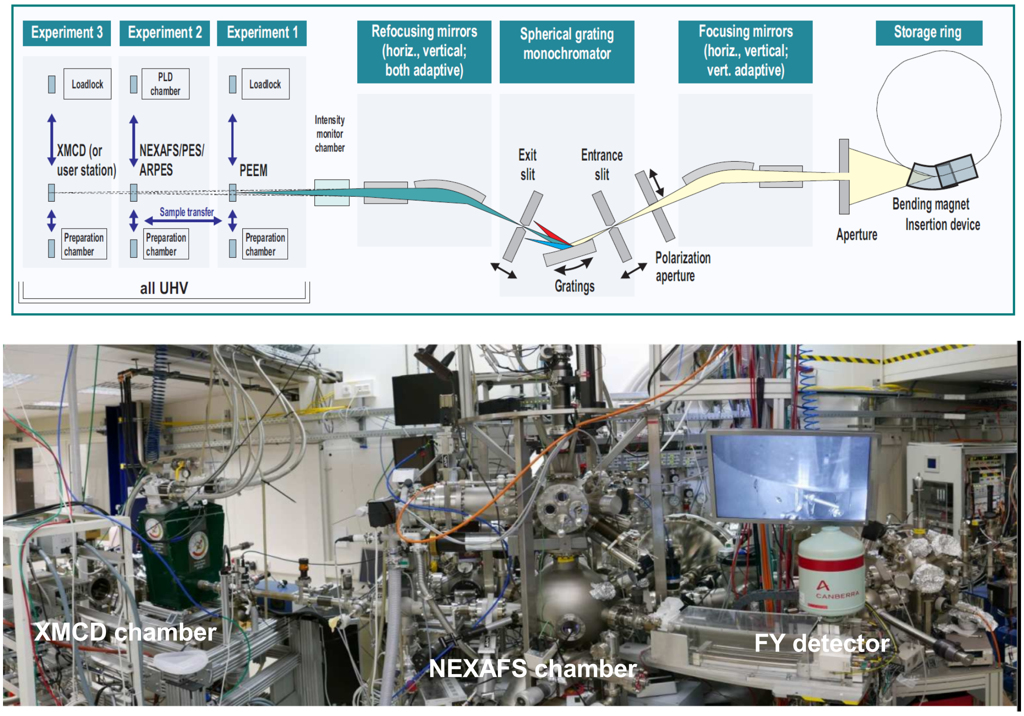

Figure 2.3: Upper panel: Layout of the WERA beamline. Lower panel: Experimental endstations of the WERA beamline. In this picture, the XMCD chamber, NEXAFS chamber and FY detector are displayed.

2.2 X-ray absorption spectroscopy

2.2.1 The absorption coefficient and absorption edges

When an electromagnetic wave goes through a material with thickness d, the intensity of the incident beam will decay exponentially. Figure 2.4 (a) illustrates the absorption process. The absorbing power of the material is described by the linear absorption coefficient μ, which has the dimension 1/length and is element-specific. Generally speaking, μ can be determined by comparing the intensity of the outgoing beam I_t after passing through a material with thickness d to that of incident beam I_0, such that

$$\frac{I_t}{I_0} = e^{-\mu d}. \tag{2.1}$$

This is the well-known Beer-Lambert formula for linear absorption. If one rewrites Eq. 2.1, one obtains

$$I_t = I_0 \cdot e^{-\mu d} = I_0 \cdot e^{-\rho_a \sigma d}. \tag{2.2}$$

σ is the x-ray absorption cross-section [length^2/atom]. ρ_a is the atomic number density defined as $N_A \cdot \rho_m/\mathrm{A}$ [atoms/length^3], where N_A is Avogadro's number and A is atomic mass number. Table 2.1 lists the relevant parameters for Co and Ni.

Element	ρ_m (kg/m^3)	A (g/mol)	ρ_a (atoms/nm^3)	V (Å^3)
Co	8900	58.93	90.9	11
Ni	8908	58.69	91.4	10.9

Table 2.1: The mass density ρ_m, atomic mass number A, atomic number density ρ_a and atomic volume V for Co and Ni. From Ref. [50].

When the incident x-ray energy is scanned from low energy to high energy the absorption signal is generally decreasing, approximately as the inverse third power of the incident photon energy [48]. Figure 2.4 (b) shows the absorbance as a function of energy of Pb for example, and the generally decreasing behavior of the absorbance with photon energy. Notably, one also can see that there are several abrupt steps in the absorption spectrum. These abrupt increases in absorption cross-section are caused by the so-called "absorption edges". An absorption edge corresponds to the binding energy of core electrons. When the incident beam has sufficient photon energy to eject electrons from this core level to an unoccupied valence state, one can observe a sharp rise in the absorption spectrum. According to Fermi's Golden Rule, the transition rate from an initial state ψ_i to a final state ψ_f can be written as

$$W_{fi} = \frac{2\pi}{\hbar} |\langle \psi_f | H_T | \psi_i \rangle|^2 \delta_{E_f - E_i - \hbar\omega}. \tag{2.3}$$

H_T is the transition operator which describes the interaction of the electromagnetic field of the x-ray photon with the absorbing atom. The δ function ensures the conservation of energy. The transition rate is proportional to the squared matrix element. Quadrupole transitions can, in general, be neglected in the soft x-ray range since they are several hundred times weaker than the dipole transition. The dipole matrix element has a non-zero value only if the orbital quantum number of ψ_f differs by 1 from that of ψ_i. In Fig. 2.4 (b), one can see three absorption edges, K,

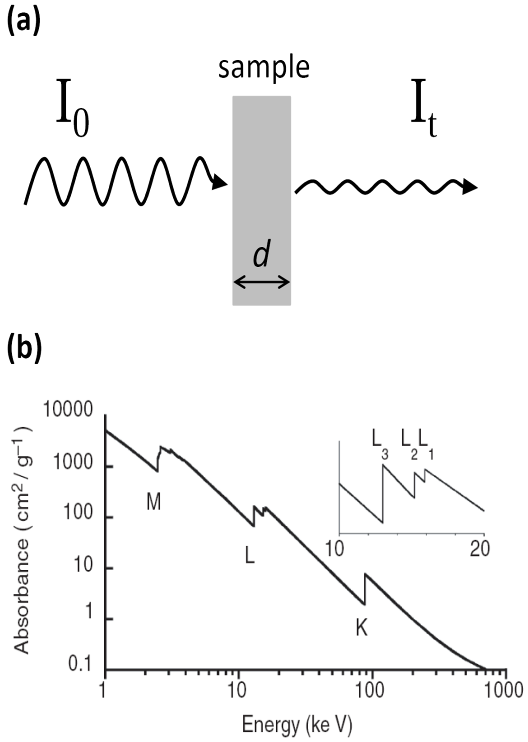

Figure 2.4: (a) When the incident beam goes through a material with thickness d, the intensity of the incident beam will be reduced exponentially by the material. (b) Absorbance as a function of energy of Pb. In general, the absorption coefficient μ varies approximately as the inverse third power of the photon energy. The inset shows the absorption at the L edges. From [48].

L and M edges corresponding to transition of electrons from $n = 1$, 2 and 3, respectively. If we closely examine Fig. 2.4 (b), the M and L edges are, in fact, split into to 5 and 3 peaks, respectively. The inset of Fig. 2.4 (b) shows the three distinct L edges, named L_3, L_2 and L_1 in the order of increasing energy. The L_1 edge corresponds to the excitation of a $2s$ level (into $3p$ levels), and the $L_{2,3}$ edges correspond to the transition from the $2p$ levels into $3d$ levels, according to dipole selection rules. This is why for TM oxides, the d-shell properties of the TM are best probed by $L_{2,3}$-edges absorption spectroscopy. Soft x-ray absorption spectroscopy is advantageous for investigating $3d$ TM oxides because the soft x-ray energy range covers the $L_{2,3}$ edges of all TMs (from 350 eV for Sc to 1100 eV for Zn), as well as the K edge of oxygen. Figure 2.5 (b) shows $L_{2,3}$ absorption edges of TM from Ti to Zn including the K edge of O. Figure 2.5 (a) depicts a simple model for the electronic transitions at the L and K edges for TM. The $L_{2,3}$ edges are dominated by the $2p$ spin-orbit coupling, which splits the XAS spectrum into two main peaks L_3 and L_2. The L_3 and L_2 structures are corresponding to $2p_{3/2} \rightarrow 3d$ and $2p_{1/2} \rightarrow 3d$ transitions, respectively.[3]

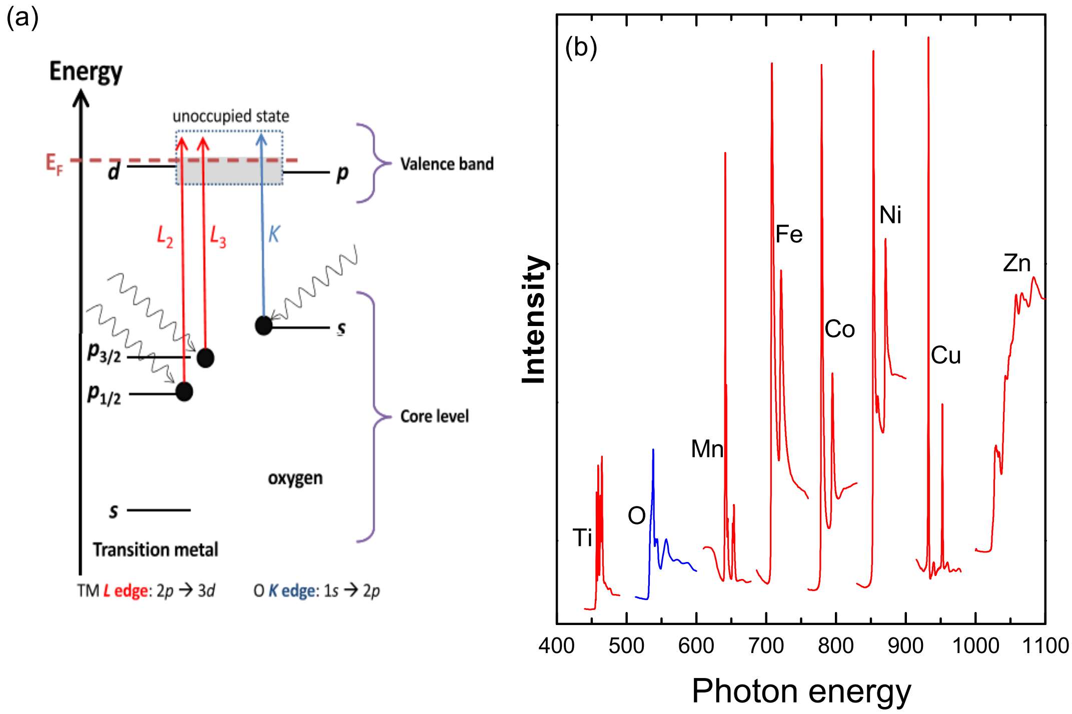

Figure 2.5: (a) shows the x-ray absorption scheme of $L_{2,3}$ and K edges. (b) shows the $L_{2,3}$ absorption edges of different transition-metal compounds, along with an example for an O-K edge. Each element has its absorption edges at different, specific energies, making x-ray absorption spectroscopy an element-selective technique.

2.2.2 Measurement of x-ray absorption spectra

The direct way to perform x-ray absorption spectroscopy is the transmission mode. This mode is sketched in Fig. 2.6 (a). One can measure the intensity loss of the incident beam passing through the sample to obtain the absorption spectrum (see the inset). Transmission mode is a standard measurement technique for the hard x-ray range. In the soft x-ray range, owing to the strong interaction between soft x-rays and the

---

[3] In this work, we plot the x-ray absorption spectra as "intensity" in arbitrary units, following the common practice within the XAS and synchrotron radiation community. When necessary, normalized spectra are shown after using the normalization procedure introduced in Section 2.4.2.

sample, it is almost impossible to perform absorption measurements in the transmission mode. Instead, in the soft x-ray range, we usually use the electron-yield (EY) mode and fluorescence yield (FY) mode. Both are indirect ways for determining μ and measure the decay products of the core hole. When a core-level electron is stimulated by the incident x ray to the outer shell, it creates a hole in the core level (core hole). The recombination of the core hole will cause secondary products of the absorption process - electrons, ions, and photons - to escape from the sample surface. The purpose of yield mode is collecting the signal of these escaping particles. The yield mode is usually classified into the Auger-electron yield, total-electron yield (TEY) and fluorescence yield (FY).

Auger-electron yield (AY)

Auger electron emission is a single-step process: The core hole induced by absorption may recombine nonradiatively with an outer-shell electron, and simultaneously excites another outer-shell electron. This process is shown in the inset of Fig. 2.6 (b) which illustrates the ejection of an Auger electron from the same outer shell. Because the AY mode only probes the un-scattered electrons with the element-specific Auger electron energy, it is a highly surface-sensitive technique. The AY mode is also an energy-selective method because one can collect the Auger electrons in a specific Auger decay channel of the core hole.

Total-electron yield (TEY)

TEY mode is used widely in the soft-x-ray range because of the easy set-up and the relative large signal. The set-up and absorption process can also be seen in Fig. 2.6 (b). On their way to the surface, most Auger electrons will scatter with other electrons, causing an avalanche of electrons to be emitted. They are called “secondary electrons” (see the brown block in the Fig. 2.6 (b)), and the TEY mode collects all the scattered “secondary electrons”. In contrast to Auger-electron yield, TEY is not a energy-selective technique since we collect all the escaping electrons. The TEY mode is not a highly surface-sensitive method but still probes only a surface region. The estimated probing depth of the TEY mode in the soft x-ray range is $\sim$ 5-10 nm. On the other hand, the TEY mode and Auger-electron yield are not suited for measuring poorly conducting or insulating samples. In this kind of sample, the recharging process of TEY mode will cause a build-up of charge near the sample surface resulting in a small, time-dependent, and history-dependent TEY signal with increasing x-ray exposure time.

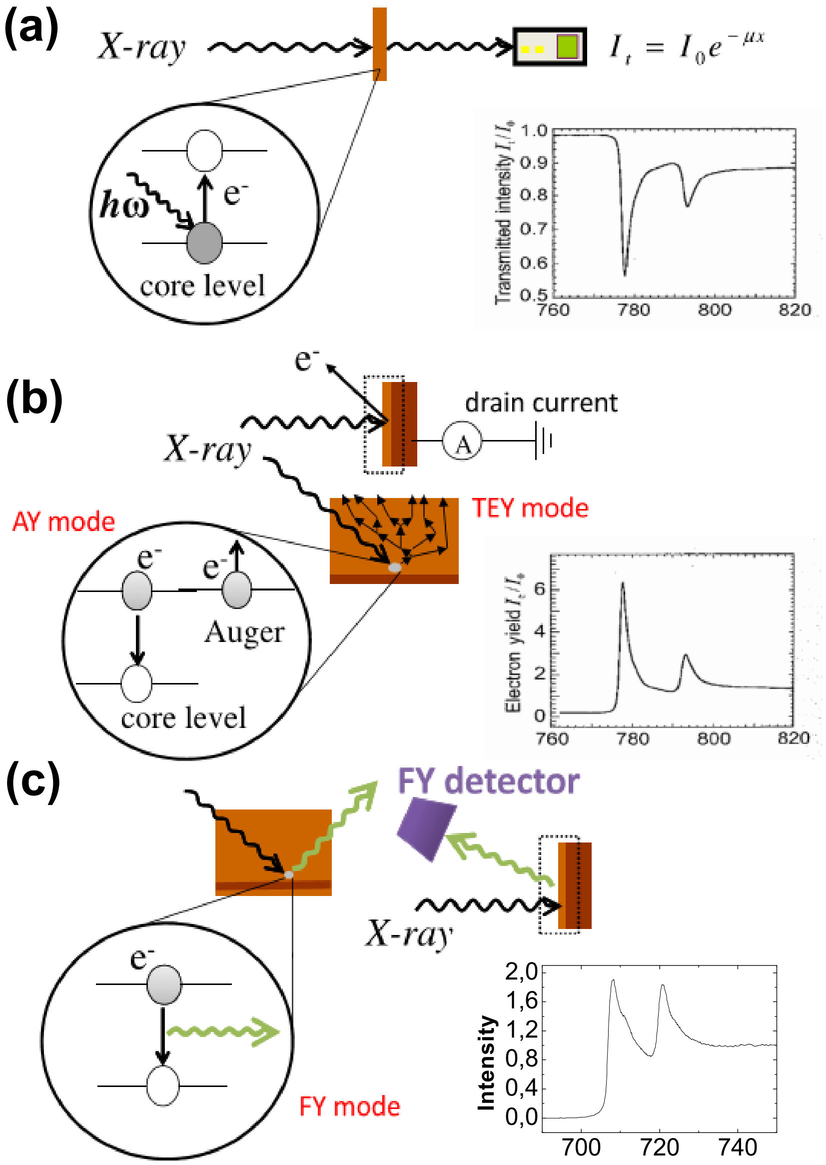

Figure 2.6: The setup of (a) transmission mode, (b) electron yield mode and (c) fluorescence yield mode. The mechanism behind these three techniques is explained in the text. This plot is reproduced from Ref. [50].

Fluorescence yield (FY)

Besides the TEY mode, the FY mode is another general technique used for absorption measurements. The idea behind the FY mode is measuring the emission of the fluorescence photon. The measurement set-up can be seen in Fig. 2.6 (c). Similar to the Auger-electron yield and TEY mode, the fluorescence efficiency [51] is also, in principle, proportional to the absorption coefficient. There are two clear advantages of using the FY mode. First, the FY mode can probe the sample deeper (~ 100 nm) than the TEY mode, making it more bulk-sensitive. Second, the FY mode can be used even for an insulating sample since we detect the emission photon instead of collecting the escaping electrons.

2.3 X-ray magnetic circular dichroism

X-ray Magnetic Circular Dichroism (XMCD) is a powerful and excellent technique for probing the element-specific spin and orbital moment of a sample directly. The XMCD phenomenon has first been predicted in 1975 by Erskine and Stern for the $M_{2,3}$ edges of Ni [52]. Experimentally, XMCD was first found in 1983 by Schütz *et al.* at the Fe K edge [53] and in 1995 by Chen *et al.* at the $L_{2,3}$ edges [54]. The idea behind the XMCD technique is utilizing light with different circular polarization to create spin-polarized "photoelectrons" in the absorption process, which then can use to analyze the spin-split valence density of state (DOS).

2.3.1 Principle and technique

In this section, a brief induction of XMCD effect is given, which follows Ref. [50]. Magnetic materials are characterized by having a partially filled valence band. The "exchange interaction" will split the $3d$ valence band into spin-up and spin-down sub-bands with different energy. In general, the bandwidth is usually a few eV and the splitting of $3d$ band is of the order of an electron volt. In ferromagnetic materials, the density of states of $3d$ valence electrons forms two bands for the different directions of the spin. Figure 2.8 (a) shows the splitting of the density of states, and this simplest band-like model of the ferromagnetic metal is usually called "Stoner model" [61]. Red and blue regions represent the occupied $3d$ state with spin up and spin down, respectively. In this case, there are more electrons with spin up occupying the $3d$ valence band. Hence, the magnetization of this configuration is spin up (upward). In a ferromagnetic TM oxide, if $2p$ electrons are stimulated to $3d$ empty bands by right-circular-polarized (RCP) and left-circular-polarized (LCP) the absorbing cross-section can be expressed simply as

$$|\langle 2p^5 3d^{n+1}|x \pm iy|2p^6 3d^n\rangle|^2 \tag{2.4}$$

Solving this equation and according to the selection rules, we can estimate the relative cross sections for absorbing of RCP and LCP light. One can see in Fig. 2.7 that there will be different absorption cross sections for ferromagnetic materials for RCP and LCP. By absorbing RCP light, the relative cross section for m_j = 1/2, -1/2 and -3/2 in $2p_{3/2}$ state stimulated to m_l = 0, -1, -2 (Δm = -1) in $3d$ spin-down empty band is 1 : 6 : 18, respectively. On the other hand, in the case of absorbing LCP light, the relative cross sections are 6 : 6 : 3. Figure 2.7

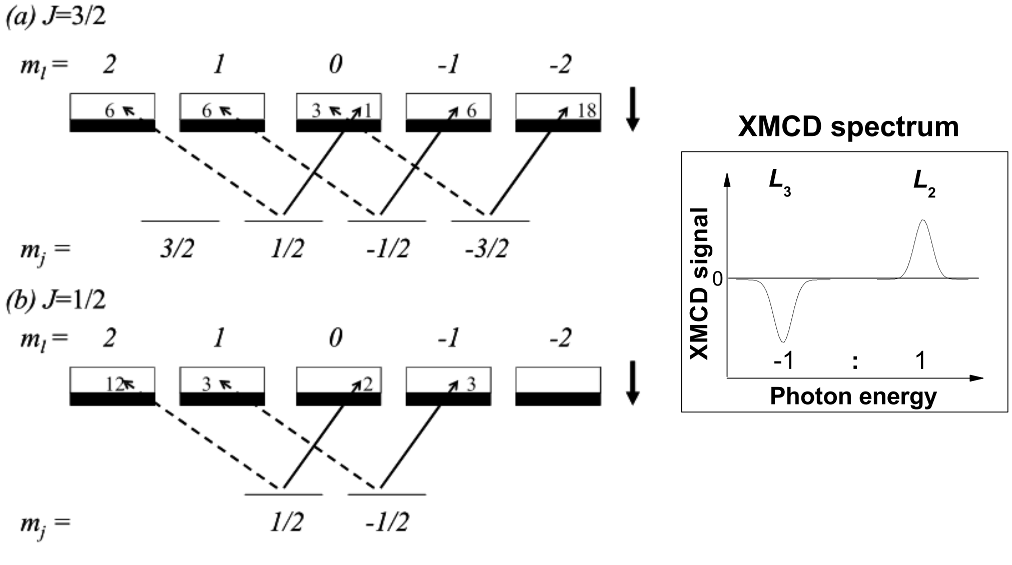

Figure 2.7: Relative cross section for absorbing of RCP and LCP light. Solid and dashed line represents the transition process of electron stimulated by the RCP and LCP light. The inset shows the XMCD signal obtained from the simplest model. The XMCD intensity of L_3 and L_2 is -1 : 1.

(a) shows the relative cross section for $2p_{3/2} \rightarrow 3d$ by absorbing RCP light. According to this simple estimation, one can see that the cross section of $2p_{3/2} \rightarrow 3d$ stimulated by RCP and LCP light is (1+6+18) : (6+6+3) = 25 : 15. Similarly, one also can get the cross section of $2p_{1/2} \rightarrow 3d$ stimulated by RCP and LCP light is (2+3) : (12+3) = 5 : 15 (see Fig. 2.7 (b)). The different cross section between RCP spectrum and LCP spectrum defines the XMCD signal. Therefore, by utilizing this simplest model, one can obtain a XMCD spectrum (shown in Fig. 2.7 inset) and the ratio of XMCD effect at L_3 and L_2 is -1 : 1. In fact, this simple model cannot quantitatively explain the experimentally observed XMCD spectrum because many-body effects, $3d$ spin-orbital interaction and the energy-band effect of $3d$ electrons are not taken into account in this model. In order to study the magnetic properties, XMCD sum rules have been proposed and verified experimentally to describe the relation between MCD spectrum and magnetic moments in the ground state of the ferromagnetic material [55]. The XMCD sum rules will be discussed in the next section.

To perform an XMCD measurement, we use the beam with different circular polarization to preferentially excite spin-up or spin-down electrons. The right circularly polarized (RCP) beam (μ^+) mainly excites the spin-up electrons, while the left circularly polarized (LCP) beam (μ^-) mainly excites the spin-down electrons. Figure 2.8 (a) clearly shows the excitation process of spin-up and spin-down electrons. The XMCD measurement is mostly sensitive to the magnetic moments aligned parallel to the vector of circular polarization, and the signal scales as $\cos\theta$. θ is the angle between the magnetic moment and the polarization vector which, for circular polarization is parallel or antiparallel to the propagation vector. Therefore, magnetic moments perpendicular to the light propagation vector will not contribute to the XMCD, and the same will occur for antiferromagnetically coupled moments that will cancel out contributions of their individual sublattices to the XMCD signal. Therefore, in order to enhance the XMCD signal, a magnetic field was applied in the direction of the beam, thus aligning all the ferromagnetically coupled magnetic moments parallel to the light propagation vector. In practice, one has to apply a magnetic field on the studied sample to magnetically saturate the sample when performing the XMCD measurement. The setup of the XMCD measurement is simply shown in Fig. 2.8 (b). The XMCD data are collected as follows: positioning the sample in a

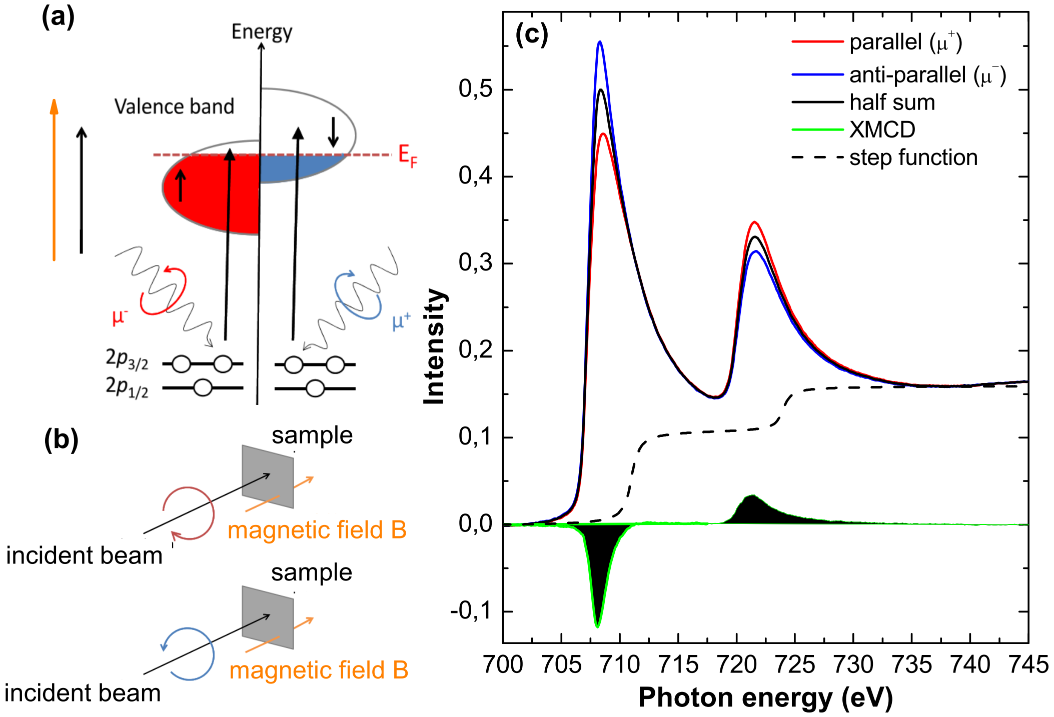

Figure 2.8: (a) The Stoner model of ferromagnetic $TM3d$ shell. (b) The XMCD spectra (green line) is obtained by subtracting the anti-parallel spectra (blue line) from the parallel spectra (red line). By utilizing the sum rules, one can obtain the individual orbital (m_L) and spin (m_S) moment in μB per atom directly.

magnetic field which is parallel to the incident beam. Then one records the absorption spectra with RCP/LCP beam. Depending on the light polarization direction more electrons of one spin direction are excited to the unoccupied states than those of the other spin direction due to the different occupied number in the $3d$ valence band. The dichroism is then given by the difference of the RCP spectrum and the LCP spectrum. Figure 2.8 (c) shows the standard XMCD spectrum: the red line represents the RCP spectrum, the black line represent the LCP spectrum and the green line is the so-called “XMCD spectrum”. Vice versa, in principle, the same result can be achieved by utilizing the light with fixed circular polarization, and switching the applied magnetic direction.

2.3.2 Sum rules: spin and orbital moment

As discussed above, the electronic transition in the absorption process is spin-selective by utilizing a circularly polarized beam. Hence, the

XMCD spectrum reflects directly the spin and orbital polarization. By utilizing well-established XMCD sum-rules [54, 55, 56, 57, 58, 59, 60], one can determine the individual spin and orbital moments. The XMCD sum rules for $L_{2,3}$ edges are given by

$$m_{orb} = -\frac{4\int_{L3+L2}(\mu^+ - \mu^-)d\omega}{3\int_{L_3+L_2}(\mu^+ + \mu^-)d\omega} \cdot (10 - n_{3d}), \tag{2.5}$$

and

$$m_{spin} = -\frac{6\int_{L_3}(\mu^+ - \mu^-)d\omega - 4\int_{L_3+L_2}(\mu^+ - \mu^-)d\omega}{\int_{L_3+L_2}(\mu^+ + \mu^-)d\omega} \cdot (10 - n_{3d}) \cdot (1 + \frac{7\langle T_Z \rangle}{2\langle S_Z \rangle})^{-1}, \tag{2.6}$$

where n_{3d} is the $3d$ electron occupation number of the transition-metal ion under consideration. μ^+ and μ^- (red and blue line in Fig. 2.8 (c)) are the absorption intensities for RCP and LCP light, respectively. "L_3" and "L_2" denote the integrated area of L_3 and L_2. $\langle T_Z \rangle$ is the expectation value of the magnetic dipole operator and can be neglected in a polycrystalline sample. In this thesis, the sum rules were used to analyze the XMCD for separating the contribution of spin and orbital magnetic moment of Co and Ni ions.

2.4 Data analysis

2.4.1 Measurement of reference

For energy calibration, we have also done XAS measurements of a reference crystal, NiO, whose main peak position at the Ni-L_3 edge (853 eV) is precisely known from EELS measurements. In practice, the reference NiO sample is laterally moved into the "monitor chamber" (upstream of the end-station), cutting about 5 % intensity of the incident beam. We measured the reference signal right before and after every single XAS scan at other absorption edges.

2.4.2 XAS spectrum in TEY mode

In this section, I introduce the data-analysis procedure of XAS, and the Co-$L_{2,3}$ XAS spectrum of $LaCo_{0.5}Ni_{0.5}O_3$ is used as an example. One measures the incoming intensity I_0 through the use of a gold mesh which absorbs a certain fraction of the intensity of the incident beam.

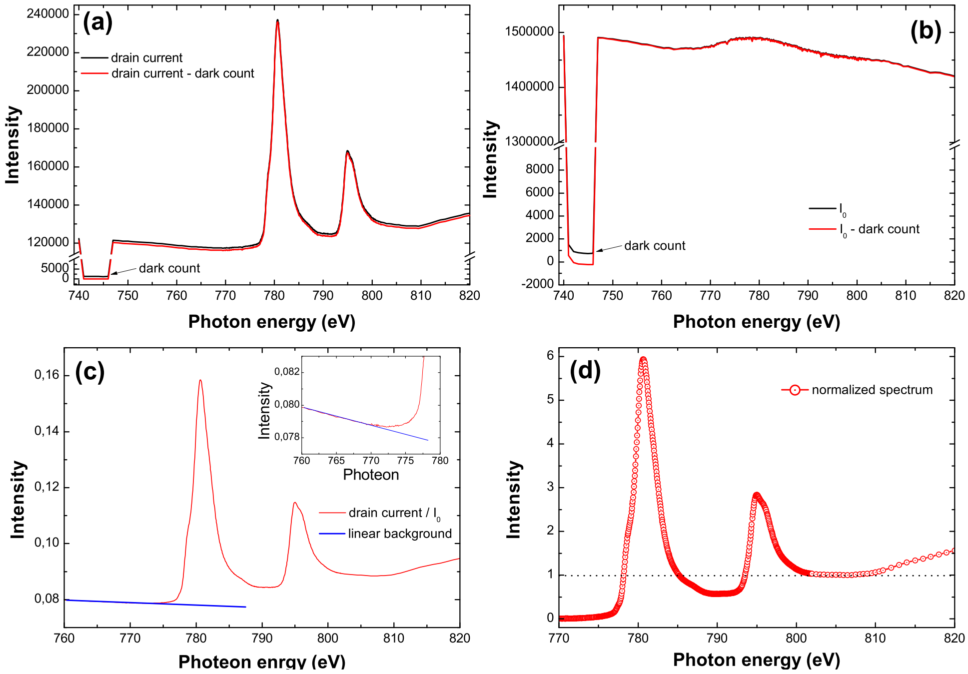

Figure 2.9: Normalization procedure of Co-$L_{2,3}$ XAS spectrum. The detail of this procedure is described in the text.

The remaining beam will hit the sample, and then one can measure the charging current ("drain current", TEY mode) of the sample. The drain current from the gold mesh, on the other hand, is proportional to I_0. Electronic apparatuses may show a small signal, a small current even in the absence of incoming beam. This kind of offset and/or noise causes the so-called "dark count" and must be eliminated from the raw data of all channels. In order to record the dark current, one can close a valve upstream of the I_0 chamber for a few seconds and perform the measurement for all channels. In Fig. 2.9 (a) and (b), the contribution of the dark count is shown in the energy range from 741 eV to 746 eV. To eliminate the dark count, one can subtract the dark count from the raw TEY and raw I_0 spectra (black line in the Fig. 2.9 (a) and (b)), and the resulting spectra are shown in red. After subtracting the dark count, the TEY-channel is divided by the I_0-channel, and the resulting spectrum is shown in Fig. 2.9 (c). Then, a (usually) linear background in the pre-edge range (760 - 765 eV) is subtracted from the I_0-normalized spectrum, and finally, the result is normalized to 1 in the post-edge range (803 - 806 eV).

2.5 Sample preparation and characterization

2.5.1 Sol-gel method

LCNO ceramics with x in the range x = (0.0, 1.0) were synthesized by utilizing the sol-gel method [62, 63], which was taught to me by Dr. D. Fuchs[4]. High-purity La_2O_3, Co, and Ni powder were used as the precursors. First, La_2O_3 powder was dried at 800 °C for 8 hours. The dried La_2O_3 was dissolved together with Co and Ni powder in a stoichiometric ratio in diluted nitric acid (32% HNO_3 of 70 ml) (see Fig. 2.10 (a)). Diluted citric acid (30 ml deionized water + 5 g citric acid powder) was then added, and we concentrated this solutions by a slow evaporation at 100 °C while stirring. Next, the resulting xerogel (see Fig. 2.10 (b)) was fired at 250 °C for 5 hours and at 500 °C for 10 hours in air to remove the carbonaceous species. After grinding in a mortar, the powders were further sintered in air at 950 °C for 30 hours and at 1050 °C for 48 hours (the resulting powder are shown in the Fig. 2.10 (c)). Finally, the powders were pressed into pellets. To ensure good oxygen stoichiometry the pellet samples were further sintered at 1050 °C in a flow of oxygen for 48 hours. The pressed samples after sintering in flowing oxygen are shown in Fig. 2.10 (d).

The sample structures of all LCNO compounds were determined in octahedral (O_h) symmetry by powder x-ray diffraction at room temperature, and the detailed structural analysis is discussed in Chapter 4.

2.5.2 Powder x-ray diffraction

X-ray powder diffraction (XRD) patterns were recorded by Dr. D. Fuchs at room temperature using a STOE diffractometer in Bragg-Brentano geometry and Mo-$K\alpha_1$ radiation. The x-ray powder diffraction patterns were recorded with monochromatized Mo-$K\alpha_1$ radiation in the 2Θ range of 5° to 55°. The x-ray generator was operated at 40 kV and 40 mA. The monochromator used was Germanium (220). The data were collected with a step size of 0.01°. To obtain the lattice parameters and atomic positions, XRD patterns were fitted using the Rietveld refinement technique [64].

---

[4] Institut für Festkörperphysik, Karlsruher Institut für Technologie

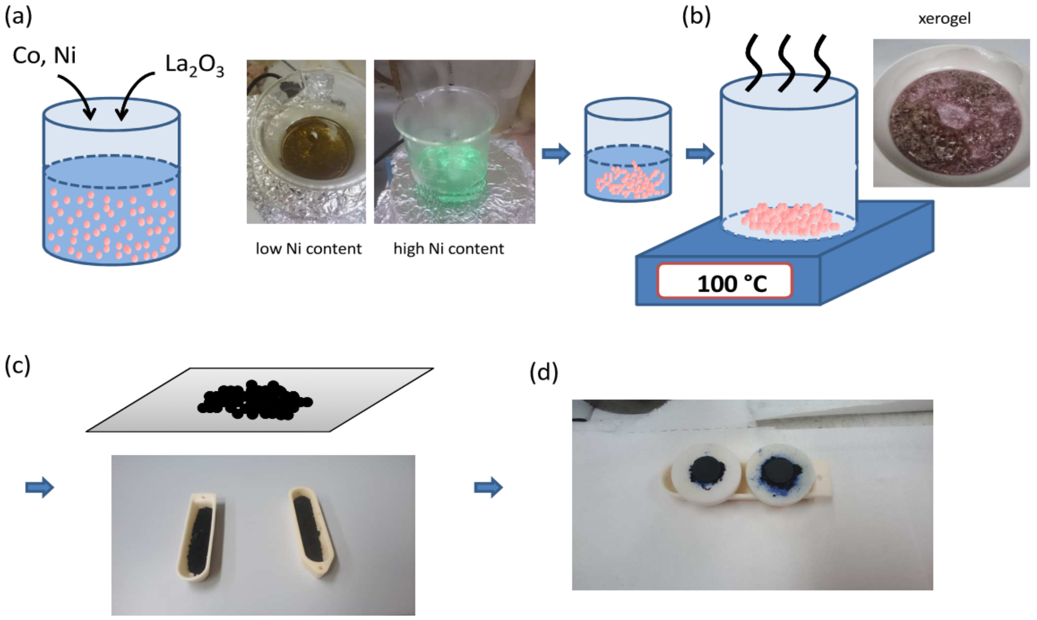

Figure 2.10: Sintering procedure. Detailed description of sintering is explained in the text.

2.5.3 Magnetic characterization

Temperature-dependent magnetic measurements of M(T) in LCNO have been performed with a superconducting quantum interference device (SQUID) magnetometer. The ferromagnetic behavior for the appropriate compsitions has been confirmed and one can derive the ferromagnetic transition temperature T_C from the M(T) results. The discussion of magnetic behavior will be presented in Chapter 6.

Chapter 3

Theory: multiplet calculations

Due to the dipole selection rules, the XAS process is very sensitive to which final state of $2p^5 3d^{n+1}$ can be reached from the initial state $2p^6 3d^n$ and with what intensity [65, 66]. This makes the XAS technique particularly useful for determining the spin, orbital, and valence state of ions [13, 67]. In this chapter, we first introduce the models for the Mott-Hubbard and the charge-transfer insulator. Then, we explain the physics behind multiplet calculations. Finally, the use of the CTM4XAS program and a simple example are briefly presented.

3.1 Mott-Hubbard insulator and Charge-transfer insulator

3.1.1 Hubbard model and Mott-Hubbard insulator

Interesting electronic and magnetic properties in transition-metal oxides are mainly dominated by a competition between a tendency towards delocalization due to band formation and a tendency towards localization due to the repulsive Coulomb interaction between the electrons. The metal-insulator transition (MIT) associated with these effects has attracted a lot of attention in the past. The Hubbard model is the first theoretical model for explaining the insulating behavior of partially filled d orbitals in transition-metal oxides. The key problem in understanding the MIT behavior is clarifying the competition between the hopping energy (kinetic energy) of electron and the on-site Coulomb repulsion energy. The Hamiltonian of the Hubbard model is given by,

$$H_{Hub} = -T \sum_{\sigma=\uparrow,\downarrow} [(c^{\dagger}_{1\sigma} c_{2\sigma} + c^{\dagger}_{2\sigma} c_{1\sigma}) + U(n_{1\uparrow} n_{1\downarrow} + n_{2\uparrow} n_{2\downarrow})]. \tag{3.1}$$

The first term in this equation describes the kinetic energy of electrons, which drives electrons to be delocalized. The parameter T is the strength of the hopping integral. The second term describes the on-site Coulomb repulsion energy U, and the energy U is defined as

$$U = E(d^{n+1}) + E(d^{n-1}) - 2E(d^n) \tag{3.2}$$

In the case of $U > T$, a half-filled $3d$ band will split into two bands: the upper Hubbard band (UHB) and the lower Hubbard band (LHB). The LHB is filled with $3d$ electrons and the UHB is empty, leading to a so-called "Mott-Hubbard insulator". The energy gap is defined by UHB - LHB. The electronic structure of a Mott-Hubbard insulator is sketched in Fig. 3.1 (a).

3.1.2 Charge-transfer insulator

The overlap of the d orbitals of the transition metal and the p orbitals of the ligand (oxygen) upon hybridization is also a crucial factor. When a transition-metal ion hybridizes with the ligand, the electrons will be hopping between transition metal and ligand depending on the hybridization strength. This redistribution of electrons indeed influences the physical properties. Therefore, it must be taken into account in describing the MIT behavior. The energy cost to move an electron from the ligand to the transition-metal ion is the so-called "charge-transfer energy (Δ)", and is defined as

$$\Delta_{d^n} = E(d^{n+1}\underline{L}) - E(d^n) \cong \Delta_{d^{n+1}} - U. \tag{3.3}$$

$\underline{L}$ denotes a ligand hole residing at the oxygen site. It is important to note that a small or even negative value for Δ corresponds to a large charge transfer from/to a ligand hole, whereas a large value for Δ effectively "forbid" any charge transfer. The introduction of Δ leads to a distinction of two types of insulators: the Mott-Hubbard insulator and the charge-transfer insulator. Figures 3.1 (a) and (b) schematically depict the difference between (a) a Mott-Hubbard insulator and (b) a charge-transfer insulator. As explained above, the partially filled d orbital is split into a totally filled LHB and an empty UHB owing to the on-site d-d Coulomb repulsion energy U causing the Mott-Hubbard insulator. On the other hand, if the Coulomb repulsion energy U is larger than the charge-transfer energy Δ, the LHB moves below the ligand p

orbital causing a charge-transfer insulator. Therefore, the energy gap of Mott-Hubbard insulator and charge-transfer insulator is determined by U (UHB - LHB) and Δ (UHB - p orbital), respectively.

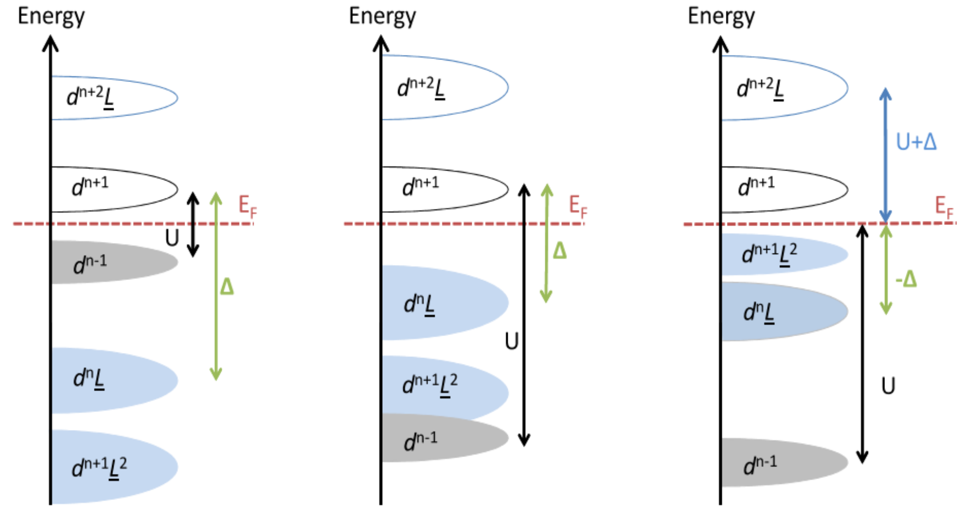

(a)Mott-Hubbard insulator (b) Charge-transfer insulator (c) negative charge transfer

Figure 3.1: Schematic diagram of DOS for (a) Mott-Hubbard insulator, (b) Charge-transfer insulator and (c) negative charge-transfer insulator. The filled and empty grey band represents the occupied and unoccupied TM-$3d$ band, and the filled and empty blue band represents occupied and unoccupied the O-$2p$ band. Reproduced from Ref. [68].

3.1.3 Negative charge-transfer energy

The charge transfer energy decreases with increasing valence state of the transition-metal ion. It can even become negative in the case of compounds with unusually high valence state. Figure 3.1 (c) exhibits the electronic structure of negative charge-transfer case. In this special case, *i.e.* small or negative charge-transfer energy, the energy gap is strongly dependent on the p-d hybridization strength. It is not only determined by U or Δ. The p-d hybridization is very sensitive to the bond length and bond angle since the d electron hopping is mediated by the ligand p orbital. Hence, the transport properties and magnetic interaction are significantly influenced by the small or negative charge-transfer energy.

3.1.4 Zaanen-Sawatzky-Allen (ZSA) phase diagram

The band gap and electronic structure of transition-metal oxides is highly dependent on the parameters U, Δ and the $3d$-$2p$ hybridization strength T. Zaanen, Sawatzky and Allen have discussed the connection between these three parameters and a metal-insulator transition, and the results are summarized in the ZSA phase diagram [1], see Fig. 3.2. In this diagram, the blue line separates the metallic phase (area C and area D) from the insulating phase (area A and area B). In Area A, it is Mott-Hubbard insulator and E$_{gap}$ $\propto$ U since $U \ll \Delta$. The charge-transfer insulator belongs to Area B and E$_{gap}$ $\propto$ Δ since $U \gg \Delta$. A more complicated situation is in the intermediate region (AB). In this region, U is comparable with Δ, resulting in a highly mixed $3d$-$2p$ character near the Fermi level. Compounds which fall into this region possess very rich physical properties.

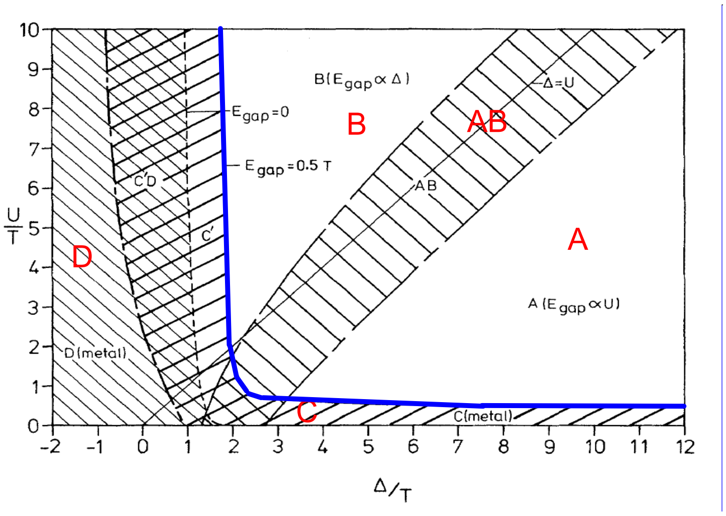

Figure 3.2: Zaanen-Sawatzky-Allen phase diagram. The solid blue line separates the metallic phase from the insulating phase. Area A: Mott-Hubbard insulator. Area B: charge-transfer insulator. Area C: d-band metals. Area D: p-type metals. This plot is reproduced from Ref. [1].

3.2 Atomic multiplet theory

In transition-metal ions, owing to the strong interaction between $3d$ electrons, strong overlap between the wave-functions of the core hole and the valence electrons, and the interplay between U and Δ, the single-particle model fails to apply. The Hamiltonian of N electrons in a sub-shell of the free atom is given by

$$H = \sum_{i=1}^{N}(\frac{p_i^2}{2m} - \frac{Ze^2}{r_i}) + \sum_{i=1}^{N}\xi(i) l_i \cdot s_i + \sum_{i,j}\frac{e^2}{8\pi\epsilon_0 r_{ij}}. \tag{3.4}$$

The first term denotes the kinetic energy and the Coulomb interaction between electrons and nucleus of N electrons. The second term is the spin-orbit coupling H_{SO} of each electron, and the third term describes the electron-electron interaction H_{ee}. For a $3d^N$ configuration, the number of microstates is obtained by 10!/(10-N)!N!. The microstates can be classified by their spin moment S, orbital moment L and total angular moment J, combined into the so-called "term symbol $^{2S+1}L_J$". One can calculate the matrix elements of the different terms with the electron-electron interaction (H_{ee}) to obtain the relative energies, and the matrix elements are given as:

$$\langle ^{2S+1}L_J | \frac{e^2}{r_{12}} | ^{2S+1}L_J \rangle = \sum_k f_k F^k + \sum_k g_k G^k. \tag{3.5}$$

Following the definitions in Ref. [69], F^k and G^k are the Slater-Condon parameters of the Coulomb repulsion and exchange interaction. respectively. The Slater-Condon parameters and spin-orbital coupling effects in p and d states of Co^{3+}, Co^{4+}, Ni^{2+} and Ni^{3+} are listed in Table 3.1.

Co^{3+}	ξ_d	F^2_{dd}	F^4_{dd}	ξ_{2p}	F^2_{pd}	G^1_{pd}	G^3_{pd}
$2p^6 3d^6$	0.074	12.662	7.916				
$2p^5 3d^7$	0.092	13.421	8.394	9.746	7.899	5.947	3.384
Co^{4+}							
$2p^6 3d^5$	0.082	13.638	8.572				
$2p^5 3d^6$	0.101	14.372	9.034	9.746	8.544	6.525	3.716
Ni^{2+}							
$2p^6 3d^8$	0.083	12.233	7.597				
$2p^5 3d^9$	0.102	13.005	8.084	11.507	7.720	5.783	3.290
Ni^{3+}							
$2p^6 3d^7$	0.091	13.276	8.294				
$2p^5 3d^8$	0.112	14.021	8.763	11.506	8.349	6.329	3.602

Table 3.1: The Slater-Condon parameters and spin-orbital coupling effect in p and d state of Co^{3+}, Co^{4+}, Ni^{2+} and Ni^{3+}. All values are in eV, and taken from Ref. [69]

In practice, it turns out that the atomic multiplet theory alone cannot accurately explain the electronic structure of $3d$ transition-metal oxides. In fact, the effects caused by the surrounding ligands cannot be neglected. It is necessary to take them into account.

3.3 Crystal-field theory and ligand-field theory

Crystal-field (CF) theory is a simple model which only considers the electrostatic influence of the neighboring atoms on the central *TM* ion. In the CF theory, one treats the central *TM* ion and neighboring atoms as point charges. The crystal-field potential can be expressed as

$$V(\overrightarrow{r}) = \frac{1}{4\pi\varepsilon_0} \int \frac{\rho(\overrightarrow{R})}{|\overrightarrow{R} - \overrightarrow{r}|} d^3R. \tag{3.6}$$

The formula can be expanded in the spherical harmonics form since the basis wave functions are expanded on spherical harmonics ($\psi(r,\theta,\phi) = R_{n,l}(r)Y_l^m(\theta,\phi)$). That is,

$$V(\overrightarrow{r}) = \frac{1}{4\pi\varepsilon_0} \sum_{l=0}^{\infty} \sum_{m=-l}^{l} \frac{4\pi}{2l+1} \int \rho(\overrightarrow{R}) Y_l^m(\theta,\phi) \frac{r_<^l}{r_>^{l+1}} Y_l^{m*}(\theta,\phi) d^3R. \tag{3.7}$$

ρ denotes the charge density of the surrounding ions, and $\overrightarrow{R}$ represents the relative distance between the central *TM* ion and the surrounding ions. The crystal-field potential can be rewritten as

$$V(\overrightarrow{r}) = \sum_{l=0}^{\infty} \sum_{m=-l}^{l} A_l^m r^l C_l^m(\theta,\phi). \tag{3.8}$$

In this equation, $A_l^m = \frac{1}{4\pi\varepsilon_0} \int \frac{1}{R^{l+1}} \rho(\overrightarrow{R}) C_l^{m*}(\theta,\phi) d^3R$ and $C_l^m(\theta,\phi) = \sqrt{\frac{4\pi}{2l+1}} Y_l^m(\theta,\phi)$. The strength of the crystal-field interaction between the *TM* ion and the surrounding ions is given in the radial part. This interaction can be estimated based on the Hartree-Fock approximation via Cowan's code [69]. The angular term leads to a limited number of nonzero matrix elements in crystal-field theory. The matrix element $< Y_{l_j}^{m_j} | Y_l^m | Y_{l_i}^{m_i} >$ is nonzero only if $|l_i - l_j| \leq l \leq |l_i + l_j|$ is fulfilled and if $l_i + l_j + l$ is even. For *TM* $3d$ electrons, $l_i = l_j = 2$. That is, only $l =$ 0, 2 and 4 need to be taken into account. In octahedral (O_h) symmetry, the *TM* $3d$ orbital will split into a three-fold degenerate t_{2g} and a two-fold degenerate e_g manifold (see the blue frame of Fig. 3.3). The energy splitting between t_{2g} and e_g is denoted by $10D_q$. The t_{2g} wave function is obtained by linear combinations of $d_{\pm1}(Y_2^{\pm1})$ or $d_{\pm2}(Y_2^{\pm2})$, and the e_g wave function is the result of linear combinations of $d_{\pm2}(Y_2^{\pm2})$ for $d_{x^2-y^2}$ and $d_0(Y_2^0)$ for $d_{3z^2-r^2}$. For the e_g orbitals, the p_σ orbitals of the surrounding ligands are pointing directly toward the d orbital of the central *TM* ion. The interaction between ligand and central *TM* ion is stronger for e_g states than for t_{2g} states. Therefore, the e_g sub-band is considerably wider than the t_{2g} sub-band.

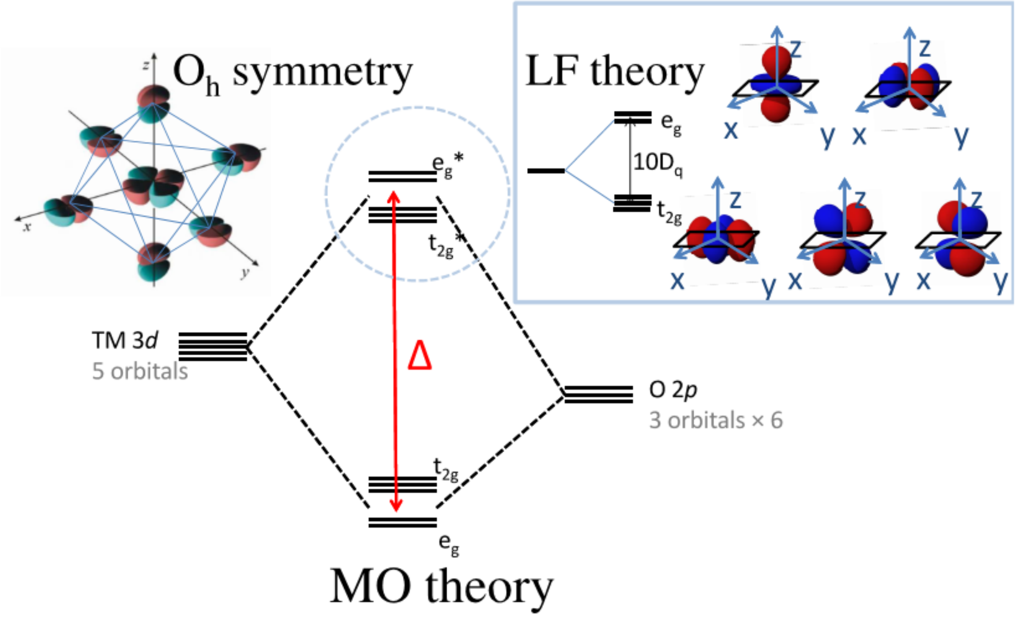

Figure 3.3: The molecular orbital (MO) theory and ligand-field (LF) theory (blue frame) in O_h symmetry. MO theory mainly describes the linear combination of 5 *TM* $3d$ atomic orbitals and 18 O $2p$ atomic orbitals (3 $2p$-orbitals × 6 oxygens). MO orbitals are divided into bonding orbitals, anti-bonding orbitals and non-bonding orbitals. The t_{2g} and e_g represent the bonding wavefunction, and the t_{2g}^* and e_g^* represent the anti-bonding wavefunction, respectively.

3.3.1 Hybridization

In practice, due to the strong $2p$-$3d$ mixing, the CF theory is still not a suitable theory for the *TM* oxides, especially for the late *TM* oxides or a *TM* ion with small or negative charge-transfer energy. The d electrons are delocalized due to the electron hopping between the central *TM* ion and the ligands. The hopping behavior of electrons is explained in Fig. 3.3. The composition of the bonding and antibonding wavefunctions depends on the strength of the hybridization. If the hybridization is small the lower-energy bonding states are mainly oxygen $2p$ in character while the higher-energy antibonding state are mostly $3d$ like. However, if the hybridization is strong enough, the electrons get a chance to hop between *TM* and ligands. In this case, the hybridization strength needs to be taken into account. The main purpose of ligand-field (LF) theory is to explain the electronic states and energies of transition-metal ions when surrounded by ligands. Beyond the CF theory, the hybridization effect is further considered in the LF theory. LF theory is a simplified application of the molecular-orbital theory (MO) to a central transition metal. In contrast to the molecular orbital theory, the LF theory only focuses on the energy splitting of the orbitals of the central transition metal under the influence of the field from surrounding ligands. Hence, the LF theory is highly dependent on the symmetry of the structure.

In the transition-metal oxides, the hybridization strength indeed influences the physical properties and needs to be taken into account in the multiplet calculations. Without hybridization, *TM* oxides can be described from the viewpoint of an ionic model as follows:

$$R^{3+}(TM)^{3+}(O^{2-})_3, \tag{3.9}$$

and the ground state is

$$|\Psi\rangle_{ionic} = |3d^n\rangle. \tag{3.10}$$

In this case, the physical properties would be determined by the ionic ground state. However, due to the highly covalent nature of the bonding between *TM* and O, the ionic model is unrealistic. In practice, we must consider the charge transfer from ligand (O^{2-}) to *TM*. Hence, a simple ground state model should be described by mixing of two configuration as

$$|\Psi\rangle_{covalent} = \alpha|3d^n\rangle + \beta|3d^{n+1}\underline{L}\rangle \tag{3.11}$$

and

$$\alpha^2 + \beta^2 = 1. \tag{3.12}$$

For this system, the Hamiltonian of the ground state is

$$H_g = \begin{pmatrix} 0 & T \\ T & \Delta \end{pmatrix}. \tag{3.13}$$

Δ is the charge-transfer energy which separates the two configurations $|3d^n\rangle$ and $|3d^{n+1}\underline{L}\rangle$, and T is the $3d \rightarrow \underline{L}$ transfer integral representing the mixture of $|3d^n\rangle$ and $|3d^{n+1}\underline{L}\rangle$. In the case that Δ is small or even becomes negative, the $|3d^{n+1}\underline{L}\rangle$ configuration will dominate the ground state. For Co^{4+} ($3d^5$) and Ni^{3+} ($3d^7$), the charge-transfer energy Δ is about -3 eV and 1.0 eV for Co^{4+} and Ni^{3+}, respectively. So, taking into account hybridization is indeed crucial for the LCNO system.

3.4 Multiplet calculation

Multiplet calculations of XAS spectrum are method to simulate the final state wave function for the XAS process, and the final state wave function can be expressed as

$$|\Psi\rangle_{final} = \alpha_f|\underline{c}3d^{n+1}\rangle + \beta_f|\underline{c}3d^{n+2}\underline{L}\rangle + ... \tag{3.14}$$

$\underline{c}$ and $\underline{L}$ denote the core and ligand hole, respectively. For the $L_{2,3}$ edges, the core hole is in the $2p$ state. The sum of the square of all coefficients must be equal to 1 (${\alpha_f}^2 + {\beta_f}^2 + ... = 1$). According to the brief introduction of the multiplet calculation in the previous sections, the input parameters for the multiplet calculation are:

1, The configuration of the initial and the final state.

2, The reduction of the Slater integrals. The values of the Slater integral (F^2_{dd}, F^4_{dd}, F^2_{pd}, G^1_{pd}, and G^3_{pd}) are listed in Table 3.1. In the CTM4XAS program, all Slater integral numbers are set as default. Generally, in the solid, the electron-electron interaction is partially screened and the Slater integral numbers are usually reduced to 80% of their “original” atomic values. This default value of 80% may be changed in special circumstances, for instance if screening effects are particularly strong.

3, Crystal-field energy ($10D_q$) and the energy splitting for the e_g and the t_{2g} bands. In the LCNO case, the additional energy splittings do not need to be taken into account since the space group is O_h for all LCNO compounds.

4, The Coulomb repulsion energy (U_{dd} and U_{pd}), the charge-transfer energy (Δ), and the $3d \rightarrow \underline{L}$ transfer integral.

3.4.1 CTM4XAS and CTM4DOC

In this thesis, all multiplet calculations and electronic configurations were performed by utilizing the CTM4XAS [75] and CTM4DOC [76] programs. The CTM4XAS program is a very powerful tool which allows us to simulate the XAS spectrum shape. The program was developed by Thole [77-79] and is maintained and further developed by de Groot [75, 80-82]. The CTM4DOC program allows one to calculate the electronic configurations in detail both in the ground state and excited state in *TM* systems.

In the following sections, two cases are shown to demonstrate the use of CTM4XAS and CTM4DOC.

3.4.2 The effect of $10D_q$ in Co^{3+} ion with O_h symmetry

Since the spin state of Co^{3+} is so sensitive to the crystal-field energy $10D_q$, it is also a good example for demonstrating the effect of changing it. Figure 3.4 shows the simulation spectra of Co^{3+} for different values of $10D_q$ varying from 0.0 eV to 2.4 eV [1]. In this simulation, we can observe a significant change in the multiplet structure (spectrum shape) when the $10D_q$ value is changed from 1.2 eV to 1.4 eV. In order to understand the meaning of this change, the electronic configuration calculations have been also performed by utilizing the CTM4DOC program. The corresponding electronic configurations are listed in Table 3.2. When the $10D_q$ value is below 1.2 eV, the electronic configuration is dominated by the $|t_{2g}{}^4 e_g{}^2\rangle + |t_{2g}{}^4 e_g{}^3 \underline{L}\rangle$ (HS + HS with one ligand hole) ground state. On the other hand, when the $10D_q$ value is above 1.4 eV, the electronic configuration is dominated by the $|t_{2g}{}^6 e_g{}^0\rangle + |t_{2g}{}^6 e_g{}^1 \underline{L}\rangle$ (LS + LS with

---

[1] Simulation parameters: Slater integral = 80%, Δ = 3 eV, U_{dd} = 5 eV, U_{pd} = 6.5 eV, and $pd\sigma$ = -1.7 eV.

one ligand hole) ground state. Accordingly, one can directly see that there is a spin-state transition when the $10D_q$ is changing from 1.2 eV to 1.4 eV. From this simulation, one can also learn that the multiplet structure in a measured XAS spectrum with different spin-states will be quite different, providing "fingerprints" that allow us to separate the contributions of HS and LS in the Co^{3+} spectrum. Therefore, XAS measurements are a good approach to investigate the spin state of certain element since it is so spin-state sensitive.

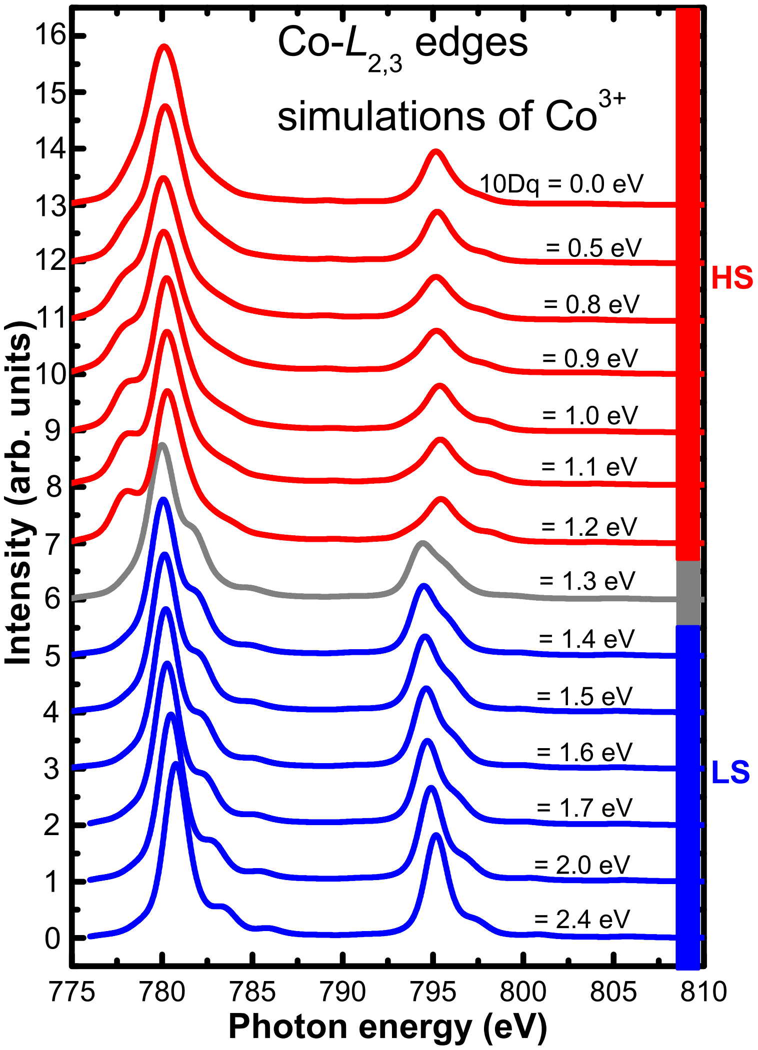

Figure 3.4: Multiplet structure of Co^{3+} in the case of $10D_q$ varying from 0.0 eV to 2.4 eV. Δ = 3 eV, $pd\sigma$ = -1.7 eV [14, 71], and Slater integral = 80% are used for this calculation. The spectra are vertically offset for clarity.

	Strongest components of the electronic configuration of Co^{3+}				
$10D_q$	$\vert t_{2g}{}^4 e_g{}^2\rangle$	$\vert t_{2g}{}^4 e_g{}^3 \underline{L}\rangle$	$\vert t_{2g}{}^5 e_g{}^2 \underline{L}\rangle$	$\vert t_{2g}{}^6 e_g{}^0\rangle$	$\vert t_{2g}{}^6 e_g{}^1 \underline{L}\rangle$
0.0 eV	73.96	20.16	5.50		
0.5 eV	74.76	19.11	5.94		
0.8 eV	75.12	18.49	6.22		
0.9 eV	75.23	18.29	6.31		
1.0 eV	75.33	18.09	6.41		
1.1 eV	75.42	17.89	6.51		
1.2 eV	75.51	17.69	6.61		
1.3 eV	7.98			53.11	29.28
1.4 eV	3.05			59.16	32.26
1.5 eV	2.35			60.45	32.63
1.6 eV	2.18			61.25	32.74
1.7 eV	2.08			61.88	32.76
2.0 eV	1.87			63.30	32.57
2.4 eV	1.66			64.73	32.06

Table 3.2: The corresponding electronic configuration of Co^{3+} in O_h symmetry for $10D_q$ varying from 0.0 eV to 2.4 eV. All number showing in this Table is in %.

3.4.3 Charge-transfer energy - An example of a d^8 configuration

The charge fluctuations in the initial and final state results in the charge transfer behavior between the central *TM* ion and the surrounding ligands. Charge transfer leads to the formation of weak satellites and to changes of the multiplet structure in the XAS spectrum. To demonstrate the charge-transfer effect, we show a series of calculations for a d^8 system, NiO. The charge-transfer energies Δ were varied from 11.0 eV to -3 eV. Figure 3.5 (a) shows the experimental XAS spectrum of NiO. In the NiO, Ni ions are in O_h symmetry with Ni^{2+} (d^8 configuration) and $10D_q$ is about 1.9 eV. In the simulation results, one first can find that the simulated spectra with Δ in the range of 3.0 eV to 11 eV well reproduce the double-peaked feature both at the L_3 and L_2 edge. In contrast, when Δ is small ($\Delta = 1.0$ eV), the simulated spectra cannot fit the experimental data well at the L_2 edge. Further, for negative Δ, there is only a single peak at both the L_3 and L_2 edge. By this first observation, one knows that the value of Δ is in the range of +3.0 eV to 11 eV. If we discuss the spectral shape in more detail, one can observe a satellite peak following the Ni-L_3 peak in the experimental data (as indicated by the arrow). Comparing the simulated spectra with experimental data, we find that only the simulated spectra with Δ = 7.0 eV, 9.0 eV and

11 eV can reproduce the satellite peak very well. When we reduce the value of Δ, one can clearly see that the energy position of the satellite peak is moving. If the charge-transfer energy is further reduced into the negative range, the satellite peak will split into two peaks. According to this simple example, it is indeed crucial to account for hybridization in the late *TM* oxides or for a *TM* ion with a high-valence state.

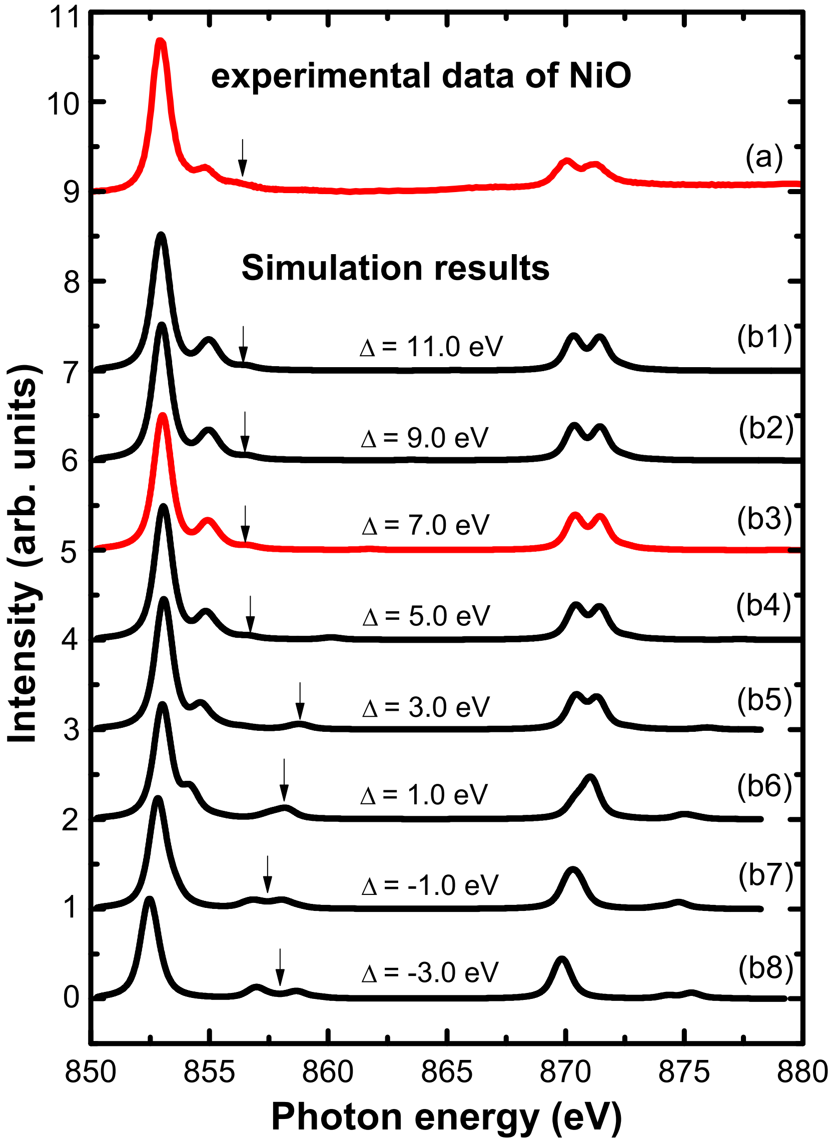

Figure 3.5: (a) XAS spectrum of NiO at Ni-$L_{2,3}$ edges. (b1) to (b6) show the simulation result in different charge-transfer energy in the range of 11 eV to -3 eV. Arrows indicate the small charge-transfer satellites (see text), and the spectra are vertically offset for clarity.

Chapter 4

Results I: Structural analysis of $\mathrm{LaCo}_{1-x}\mathrm{Ni}_x\mathrm{O}_3$ – XRD results

Magnetic and transport properties of TM oxides of the type $AB\mathrm{O}_3$ strongly depend on the orbital overlap of the anion and the B-site transition-metal, and thus, on the $\langle TM\text{-O}\rangle$ distance and the $\langle TM\text{-O-}TM\rangle$ superexchange angle. The changes in the crystallographic structure upon Ni substitution for Co were investigated. Since the ionic size of Ni is (generally) larger than that of Co, one can expect a significant change in structure when the Co ions are substituted by Ni ions in the LCO system. These changes directly influence the hybridization between O and the central transition metal, affecting the hopping process (Co/Ni-O-Co/Ni). In this chapter, I will discuss the effect of Ni substitution on the structure in the LCNO system.

4.1 Sample characterization

Results of the powder x-ray diffraction (XRD) measured at room temperature are shown in the left of Fig. 4.1. All Rietveld refinements were performed by Dr. M. Merz[1]. For all substitution levels, the diffraction pattern can be refined within the space group $R\bar{3}c$. According to the refinement results, all LCNO compounds were single phase, and no secondary or amorphous phases were detected.

The standard $AB\mathrm{O}_3$ perovskite structure is cubic with $Pm\bar{3}m$ sym-

---

[1] Institut für Festkörperphysik, Karlsruher Institut für Technologie

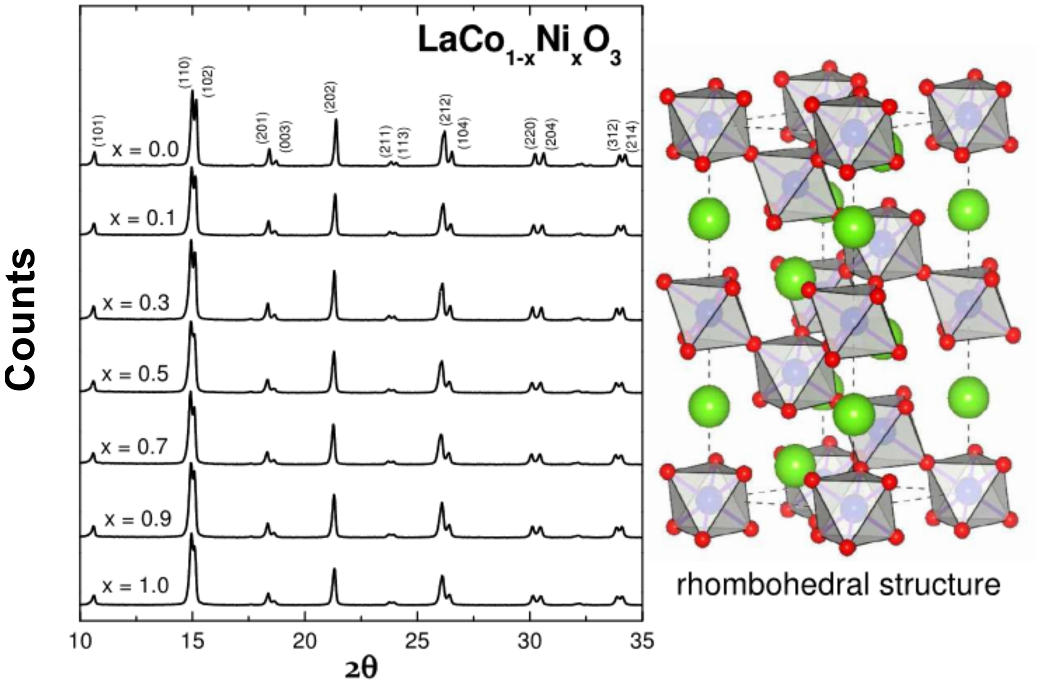

Figure 4.1: Left: x-ray diffraction patterns of all studied LCNO samples. Right: The rhombohedral structure of LCNO systems.

metry: a corner-sharing $B\text{O}_6$ octahedron with the B atom at the center site. Compared to the perovskite structure in cubic symmetry, the $B\text{O}_6$ octahedra are tilted for the $R\overline{3}c$ symmetry (see Fig.s 1.1 and 4.1). In order to investigate the structural change upon Ni doping in detail, a refinement analysis of all LCNO samples was undertaken and one example of the Rietveld refinement is shown in Fig. 4.2. In this figure, the observed and calculated XRD pattern at 300 K, the difference between them, and the Bragg-peak positions are shown. The lattice parameters a and c, the fractional atomic positions, the average bond distances $\langle TM\text{-O}\rangle$, the average bond angles $\langle TM\text{-O-}TM\rangle$, the unit-cell volumes, and the reliability factors derived from the refinements are listed in Table 4.1. Low reliability factors, absence of secondary and amorphous phases, and low background intensity indicate a good quality of all the LCNO compounds. According to the refined data, we found that the lattice parameters a and c and the unit-cell volume increase with increasing $x$up to $x \leq 0.7$, and decrease when $x > 0.7$. The order of the radii of

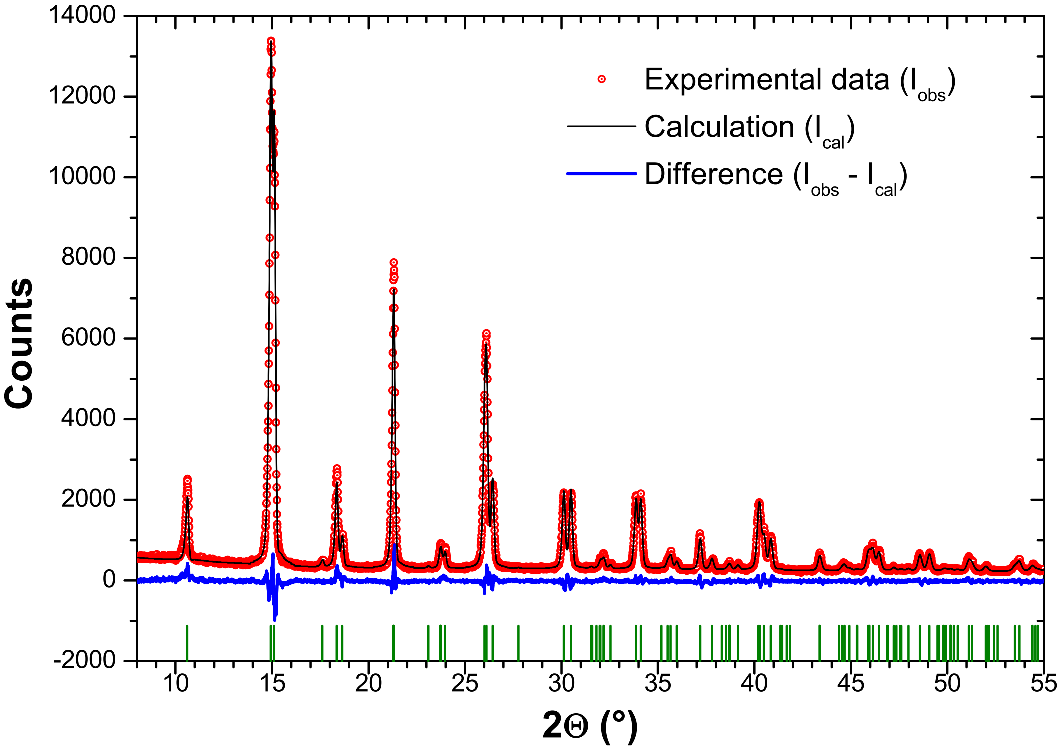

Figure 4.2: The plot of the experimental (red points) data for $x = 0.5$ together with the calculated pattern (black line). The blue line and the green bars represent the difference and the Bragg-peak positions, respectively. From difference pattern, it indicates a good refinement for $LaCo_{0.5}Ni_{0.5}O_3$ measured at room temperature.

the Co and Ni species is: $r_{Ni^{2+}} > r_{Co^{3+},HS} \approx r_{Ni^{3+},HS} > r_{Ni^{3+},LS} > r_{Co^{3+},LS} > r_{Co^{4+},HS}$. The values of the radii for the different species are listed in Table 4.2. Among the possible reasons for the expansion of the unit-cell volume are an LS-HS spin-state redistribution at the Co and/or the Ni site and the substitution of Co by Ni^{2+} which has a larger ionic radius compared to Co^{3+} and Ni^{3+}, leading to a valence-state change. Since the most critical factors which directly influence the physical properties are the average bond length $\langle TM\text{-O}\rangle$ and the average bond angle $\langle TM\text{-O-}TM\rangle$, I will discuss the effect of Ni substitution on $\langle TM\text{-O}\rangle$ and $\langle TM\text{-O-}TM\rangle$ in detail in the following sections.

		Space group: $R\bar{3}c$						
		$x = 0.0$	$x = 0.1$	$x = 0.3$	$x = 0.5$	$x = 0.7$	$x = 0.9$	$x = 1.0$
	a (Å)	5.4385(2)	5.4472(2)	5.4570(2)	5.4597(3)	5.4629(2)	5.4548(3)	5.4509(3)
	c (Å)	13.0863(5)	13.1081(5)	13.1209(6)	13.1399(7)	13.1475(6)	13.1423(6)	13.1376(7)
	$\langle TM\text{-O}\rangle$ (Å)	1.9311	1.9338	1.9370	1.9391	1.9383	1.9331	1.9319
	$\langle TM\text{-O-}TM\rangle$ (°)	163.68	163.84	163.64	163.55	164.35	165.70	165.70
	Unit-cell volume (Å^3)	386.5	388.9	390.8	391.7	392.4	391.5	390.3
	R_{wp} (%)	10.8 %	9.66 %	10.6 %	11.2 %	10.6 %	10.6 %	10.6 %
O	x	0.5504(8)	0.5494(7)	0.5500(7)	0.5508(8)	0.5488(8)	0.5441(8)	0.5445(8)
	z	0.25	0.25	0.25	0.25	0.25	0.25	0.25

Table 4.1: The lattice parameters a and c, average bond lengths $\langle TM\text{-O}\rangle$, average bond angles $\langle TM\text{-O-}TM\rangle$, unit-cell volumes, reliability factors and fractional positions of O as a function of Ni concentration. For the Rietveld refinements, the La, Co/Ni, and O atom is placed at (0,0,0.25), (0,0,0), and (x,0,z) respectively.

Radius							
Co^{3+} HS	Co^{3+} LS	Co^{4+} HS	Ni^{2+}	Ni^{3+} HS	Ni^{3+} LS	La^{3+}	O^{2-}
0.61 Å	0.545 Å	0.53 Å	0.69 Å	0.60 Å	0.56 Å	1.36 Å	1.4 Å

Table 4.2: Ionic radii of different species. For *TM*, the sixfold coordination is used. From Ref. [83, 84].

4.2 Average bond length and bond angle

The average bond-lengths $\langle TM\text{-O}\rangle$ and the average bond angles $\langle TM\text{-O-}TM\rangle$ derived from the Rietveld refinements are plotted in Fig. 4.3 (a) and (b). Upon partial replacement of Co by Ni, the average bond lengths firstly increase for $x \leq 0.5$ but decrease again for $x > 0.5$. Simultaneously, the average bond angles slightly decrease with x for $x \leq 0.5$ but increase significantly for $x > 0.5$. In other words, for $x \leq 0.5$ the change of $\langle TM\text{-O}\rangle$ dominates, while for $x > 0.5$, changes in both $\langle TM\text{-O}\rangle$ and $\langle TM\text{-O-}TM\rangle$ are important. Firstly, we discuss the regime for $x \leq 0.5$, starting from the ($x = 0.0$) parent compound LCO. For LCO, it is known that Co^{3+} LS is the dominant species [15-17]. With increasing x, the increasing $\langle TM\text{-O}\rangle$ will cause a decrease in the crystal-field energy, $10D_q$, and therefore one may expect that the fraction of Co^{3+} HS will gradually increase. In the regime for $x > 0.5$, the situation is more complicated. If one ignores for a moment the change of $\langle TM\text{-O-}TM\rangle$, one might have expected $\langle TM\text{-O}\rangle$ to continue to increase with x. The fact that $\langle TM\text{-O}\rangle$ decreases instead might indicate a spin-state redistribution back to more LS species (compared to $x = 0.5$). Whether the change in $\langle TM\text{-O-}TM\rangle$ plays a role in the spin-state redistribution is not clear. However, the decrease of $\langle TM\text{-O-}TM\rangle$ with decreasing x indicates an increased tendency for charge disproportionation (see Section 1.1.2), suggesting that a change in valence states is also important in this regime.

4.3 Summary of structural analysis

The doping-dependent structural changes have been investigated by utilizing the XRD technique. The average bond-length $\langle TM\text{-O}\rangle$ increases from 1.9310 Å for $x = 0.0$ to 1.9390 Å for $x = 0.5$ and then decreases to 1.9318 Å for $x = 1.0$. The increase of the bond length (up to $x = 0.5$) may induce a spin-state redistribution resulting in an enhanced magnetic moment: Co^{3+} LS ($S = 0$) $\rightarrow$ Co^{3+} HS ($S = 2$) and/or Ni^{3+}

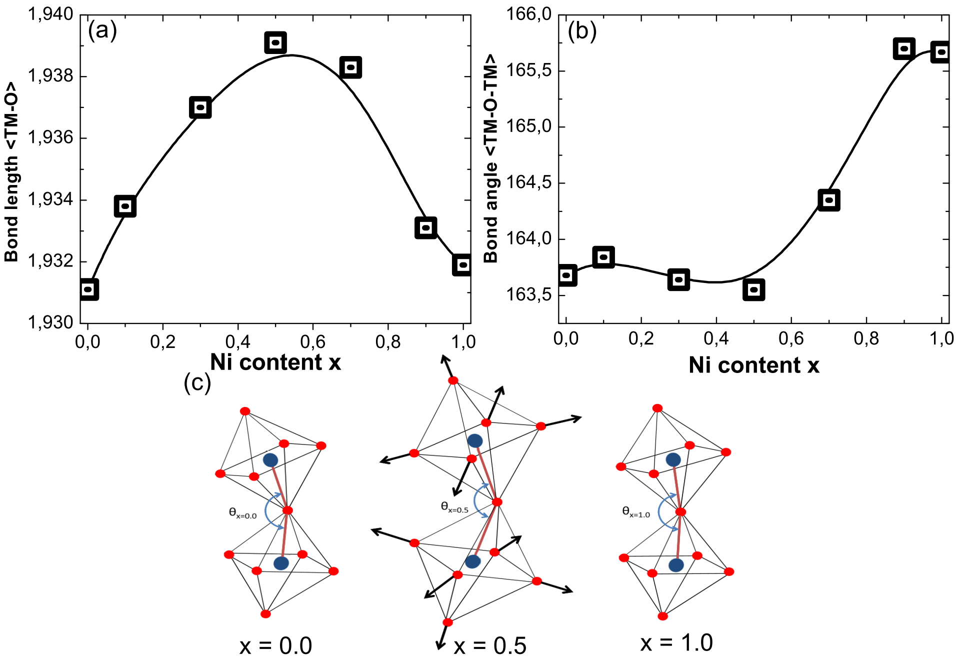

Figure 4.3: (a) The change of the average bond-length $\langle TM\text{-O}\rangle$ as a function of Ni content. (b) The change of average bond-angle $\langle TM\text{-O-}TM\rangle$ as a function of Ni content. (c) Sketches of the distortion and expansion in structure from LaCoO$_3$ to LaNiO$_3$.

LS ($S = 1/2$) → Ni^{3+} HS ($S = 3/2$). For higher x, the bond length decreases again and the reverse process may take place. Previous works [85] have reported that the maximum magnetic moment in the LCNO system appears at $x = 0.5$. This finding resembles the doping-dependent evolution of the average bond lengths. The possible spin-state redistribution upon Ni substitution will be more directly investigated by XAS measurements - see next chapter. The largest average bond length $\langle TM\text{-O}\rangle$ for $x = 0.5$ strongly implies that the average ionic size of the B-site atom in LaCo$_{0.5}$Ni$_{0.5}$O$_3$ must be larger than that for the other compositions. The ionic radius of Ni^{3+} LS is very close to the one of Co^{3+} LS (Ni^{3+} LS is 0.56 Å and Co^{3+} LS is 0.545 Å) It suggests that the average bond length should be comparable for the two end members, *i.e.* LaCoO$_3$ and LaNiO$_3$. This can be confirmed by our XRD results. Since we have observed that the average bond length is largest at $x = 0.5$, we can conclude that there should be a spin-state redistribution at the Co and/or the Ni site because the radius of Co^{3+} HS (Ni^{3+} HS) is larger than that of Co^{3+} LS (Ni^{3+} LS).

The average bond-angle $\langle TM\text{-O-}TM \rangle$ slightly decreases from 163.7 degree for x= 0.0 to 163.5 degree for x= 0.5 and significantly increases to 165.7 degree for x= 1.0. $\langle TM\text{-O-}TM \rangle$ is larger for the high Ni-content sample. The larger bond angle will give rise to a stronger overlap between the e$_g$ orbital of central TM ion and O σ band. This implies that the electrons are more easily hopping from one site to the other.

Chapter 5

Results II: Local electronic structure in $LaCo_{1-x}Ni_xO_3$ – XAS results

In this chapter, I apply XAS to investigate the changes upon Ni substitution on the local electronic structure of Co and Ni in the LCNO system. From the XRD results, we know that the average bond length and bond angle is changed with Ni substitution, and we expect the local electronic structure to change as a consequence. XAS measurements were performed at the Co-/Ni-L edges for directly probing the $3d$ electronic structure of Co/Ni near the Fermi level. Further, due to the hybridization between Co/Ni and O, performing XAS measurements at the O-K edge as well is equally important. Hence, we will discuss the local electronic structure combining the O-K, Co- and Ni-$L_{2,3}$ edges. As the temperature is also a key factor which influences the local electronic structure, we also have performed temperature-dependent XAS measurements on this system. To the best of our knowledge, these are the first XAS measurements at the Co- and Ni-$L_{2,3}$ edges in the LCNO system.

5.1 Spectroscopic observation of spin-state transition

Before investigating the complex LCNO system, we would first like to explain the XAS spectrum of the O-K and the Co-$L_{2,3}$ edges for the undoped system, *i.e.* $LaCoO_3$. As mentioned in Chapter 1, it is well-known that there is a temperature-dependent spin-state transition in LCO. This transition can be directly observed in XAS spectrum, particularly well at the O-K edge [15]. Therefore, we start our discussion with O-K XAS.

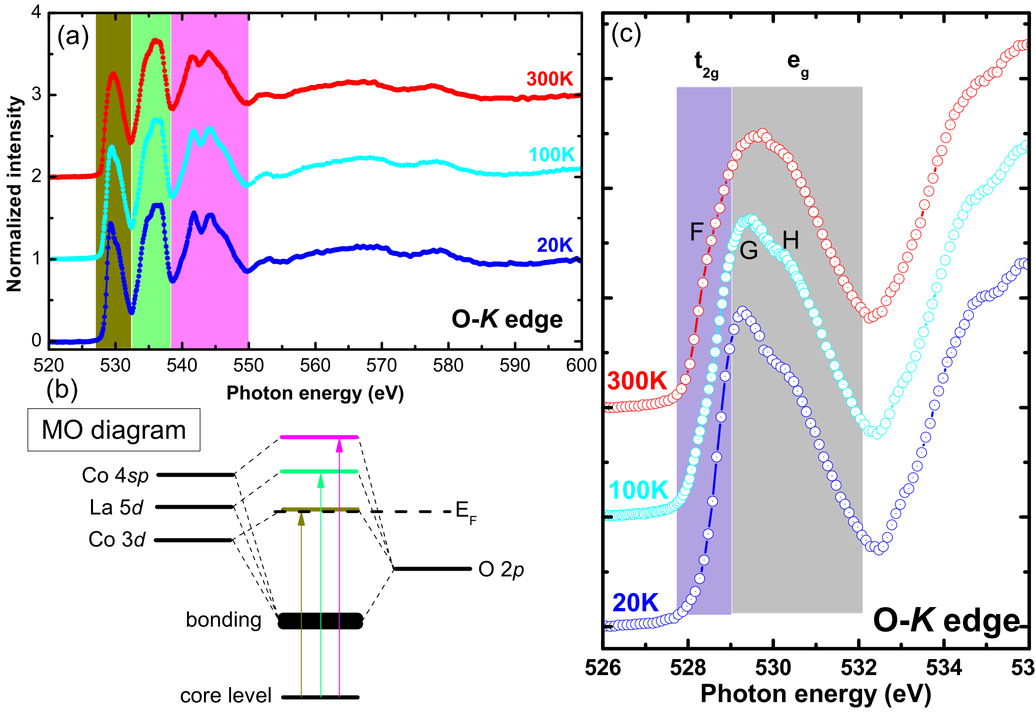

Figure 5.1: (a) The normalized O-*K* XAS of LaCoO$_3$ measured at 300 K, 100 K and 20 K. (b) Simple model of the XAS absorption processes. The dark yellow area corresponds to the transition from the core level to O-2p states hybridized with Co-3d states. The green area corresponds to the transition from the core level to the mixed state of O-2p and La-5d. The pink area corresponds to the transition from the core level to the hybridization states of O-2p and Co/Ni-4sp. (c) The O-*K* XAS of LCO concentrated on the important energy range close to E$_F$: the so-called "pre-edge" (the dark yellow area in Panels (a) and (b)). The pre-edge structure can provide very useful information on the local electronic structure of the central transition metal since it is a hybridized state between O-2p and *TM*-3d orbitals. The spectra in (a) and (c) are vertically offset for clarity.

Figure 5.1 shows (a) overview spectra of the O-*K* edge of LaCoO$_3$ at 300 K, 100 K, and 20 K in the bulk-sensitive FY detection, (b) a simple sketch of the transition processes of XAS and (c) the XAS spectra in the pre-edge region. In the O-*K* XAS of Panel (a), we see three main groups of features. The dark yellow area is the so-called "pre-edge" peak. It corresponds to the transitions from the O 1s core level to the O 2p orbitals hybridized with 3d orbitals of Co and Ni ($3d^{n+1}\underline{L} \rightarrow 1\underline{s}3d^{n+1}$; $\underline{L}$ denotes a ligand hole residing at the oxygen site, and $\underline{s}$ denotes the O 1s core hole created by the incident x-ray). The green area is assigned to the mixed states of O-2p and La-5d origin, whereas the pink area in the higher energy region is attributed to the hybridization of O 2*p* and Co/Ni 4*sp* states. The MO diagram in Fig. 5.1 shows the XAS processes for these three different regions. At the O-*K* XAS in the remainder of this thesis, we only focus our discussion to the pre-edge region from 527 to 532 eV which directly reflects the nature of the spin state and valence state of the *TM* ions. On the other hand, owing to the weak core-hole interaction at O-*K* edge, the XAS spectrum closely reflects the shape of the O-projected density of states. It gives a possibility of connecting directly to the projected band structure [86-88].

In the O-*K* pre-edge XAS of Fig. 5.1 (c), one can see a continuous change in the spectral shape with temperature. At low temperature (T = 20 K), the O-*K* pre-edge shows a double-peak structure (peak G and H). With an increase of temperature, spectral weight is gradually transferred from the high energy side to the low energy side (from peak G to peak F). This spectral weight transfer is a consequence of the well-established spin-state transition: when the six electrons of Co^{3+} totally occupy the t$_{2g}$ level, *i.e.* when ion is in the LS state, the core level electrons can only be excited to the empty e$_g$ levels (corresponding to the blue arrow in the Fig. 5.2). For this electronic configuration, one will hardly see any spectral weight in the t$_{2g}$ levels of LaCoO$_3$. This is indeed observed at low temperature since the ground state of LaCoO$_3$ is predominantly in an LS state. On the other hand, if the Co ions partially turn to the HS state gradually with temperature the t$_{2g}$ level becomes partially unoccupied, which means that the transition from the core level to t$_{2g}$ becomes possible (refer to the shorter red arrow in Fig. 5.2, shoulder F). The possibility of a transition from the core level to t$_{2g}$ can be observed for the 100 K spectrum and more clearly at the room temperature LaCoO$_3$ O-*K* spectrum, where the spectral weight in the t$_{2g}$ region is more pronounced. At the same time, the spectral weight in the e$_g$ region is reduced a little because some of the e$_g$ states are now occupied due to the spin-state transition.

Further, we examine the Co-$L_{2,3}$ XAS spectra. Figure 5.3 shows the Co-$L_{2,3}$ XAS measured at 300 K and 20 K together with EuCoO$_3$ and Sr$_2$CoO$_3$Cl (both taken from Ref. [67]) as the reference for Co^{3+} LS and Co^{3+} HS. The measured spectra of LaCoO$_3$ are consistent with previous work [14]. At the Co-$L_{2,3}$ edges XAS we can see two groups of peaks; the first group of peaks A, B and C (L_3) and the second group of peaks D and E (L_2). The inset of Fig. 5.3 shows a simple model of the $L_{2,3}$

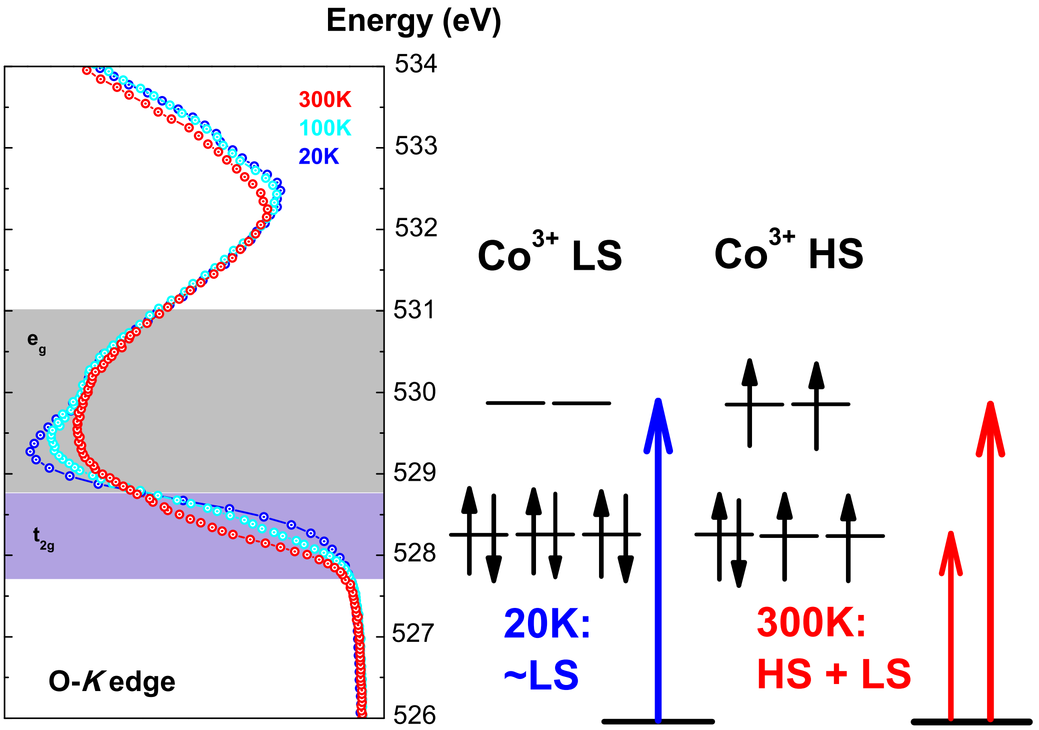

Figure 5.2: Left: This simple sketch displays the electron transition from core level to unoccupied states of Co^{3+} LS and Co^{3+} HS. Right: The temperature-dependent O-*K* XAS of LaCoO$_3$. With an increase of temperature, the spin state is gradually transferred from LS (20 K) to HS + LS (300 K). This spin-state transition can be clearly observed in O-*K* XAS.

absorption process. The line shape of 20 K spectrum is almost identical to that of EuCoO$_3$. It means that the Co^{3+} LS state is quite dominant in LCO at very low temperature. When the temperature increases, we see a slight increase (decrease) in the intensity of peak A (peak C). If we compare EuCoO$_3$ with Sr$_2$CoO$_3$Cl, one can find that the spectral weight will transfer from peak C to peak A at L_3 and from peak D to peak E at L_2 when the spin state is changed from LS to HS. This observation clearly tells us that the room temperature LCO system must be in a mixed spin state. This result is consistent with the observation at the O-K edge XAS.

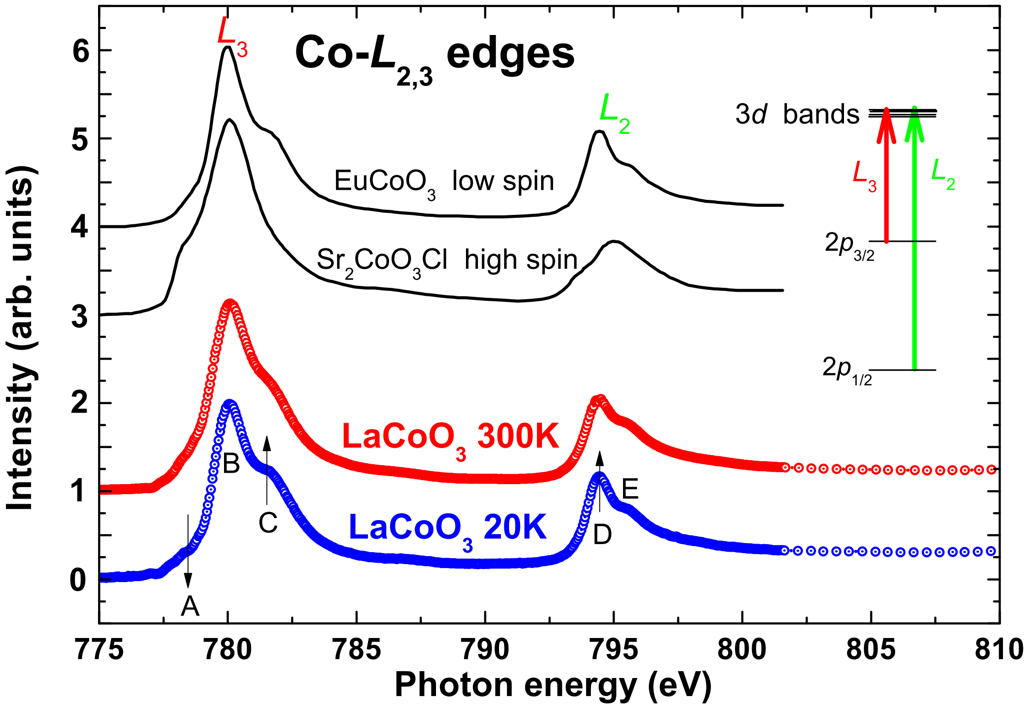

Figure 5.3: The Co-$L_{2,3}$ XAS of LaCoO$_3$ measured at 300 K and 20 K together with that of Co^{3+} HS (Sr$_2$CoO$_3$Cl [67]) and Co^{3+} LS (EuCoO$_3$ [67]) configuration for comparison. The spectra are vertically offset for clarity.

5.2 Effect of Ni-substitution on the local electronic structure

Now, we discuss the XAS spectra of Ni-substituted LaCoO$_3$ samples. The spin state, especially for Co ions, highly depends on the competition between J_{ex} and $10D_q$ (see Chapter 1). Since the substitution of Co by Ni changes the average bond-length (see Chapter 4), it implies a change of spin state in the LNCO system. In the last section, it was shown how the spectral shape changes at O-K and Co-$L_{2,3}$ XAS as the spin state is changing. Now, we can continue to study the doping-dependent effect.

5.2.1 Overview spectrum for the LCNO system

Figure 5.4 shows an overall XAS of LaCo$_{0.5}$Ni$_{0.5}$O$_3$. In this figure, we can see the transitions of $1s \rightarrow 2p$ at O-K, $2p \rightarrow 3d$ at Co-/Ni-$L_{2,3}$ and $3d \rightarrow 4f$ at La-$M_{4,5}$. From this, one can clearly see that the LCNO contains the elements O, Ni, Co and La, and no trace of other elements.

The detailed discussion of the XAS data at O-K, Co-$L_{2,3}$ and Ni-$L_{2,3}$ will be given for all studied samples in the following sections. Notably, the Ni-L_3 XAS data is seriously overlapping with the La-M_4 edge because their binding energies almost coincide. As will be shown in Section 5.2.4, it still turned out that it is possible to separate the weak Ni signal from the huge La background.

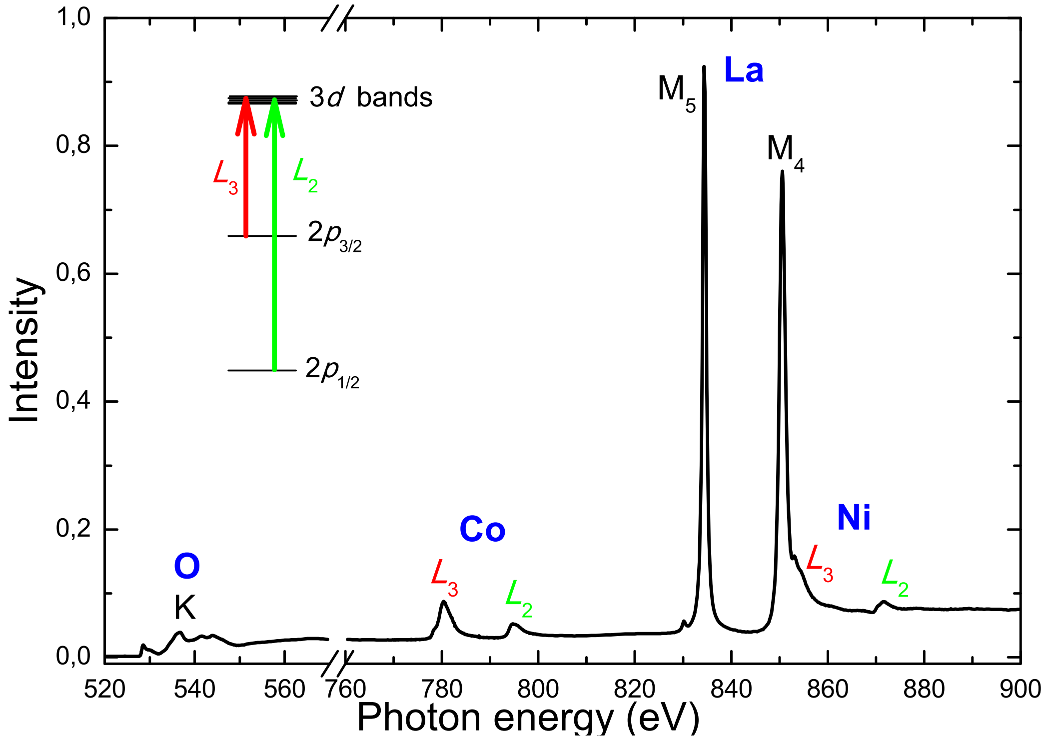

Figure 5.4: Overall scan of XAS from 520 eV to 900 eV of $LaCo_{0.5}Ni_{0.5}O_3$. In this scan range (soft x-ray range), one can observe the O-K, Co-$L_{2,3}$, La-$M_{4,5}$ and Ni-$L_{2,3}$ transitions.

5.2.2 O-*K* XAS

Figure 5.5 displays the doping-dependent O-K XAS spectra measured at 300 K in FY mode together with the spectra of $La_{1.5}Ca_{0.5}CoO_4$ and $La_{0.5}Ca_{1.5}CoO_4$ as an energy reference of Co^{4+} and Co^{3+} [89]. Here, we only show the pre-edge structure which is sensitive to spin-state redistributions, valence-state changes, and changes in the density of states near the Fermi level. When we dope 10% of Ni in this system, a small peak around 528.3 eV appears (peak O_A). A gradual increase in spectral weight of O_A was observed with the increase of Ni content. In the $x =$

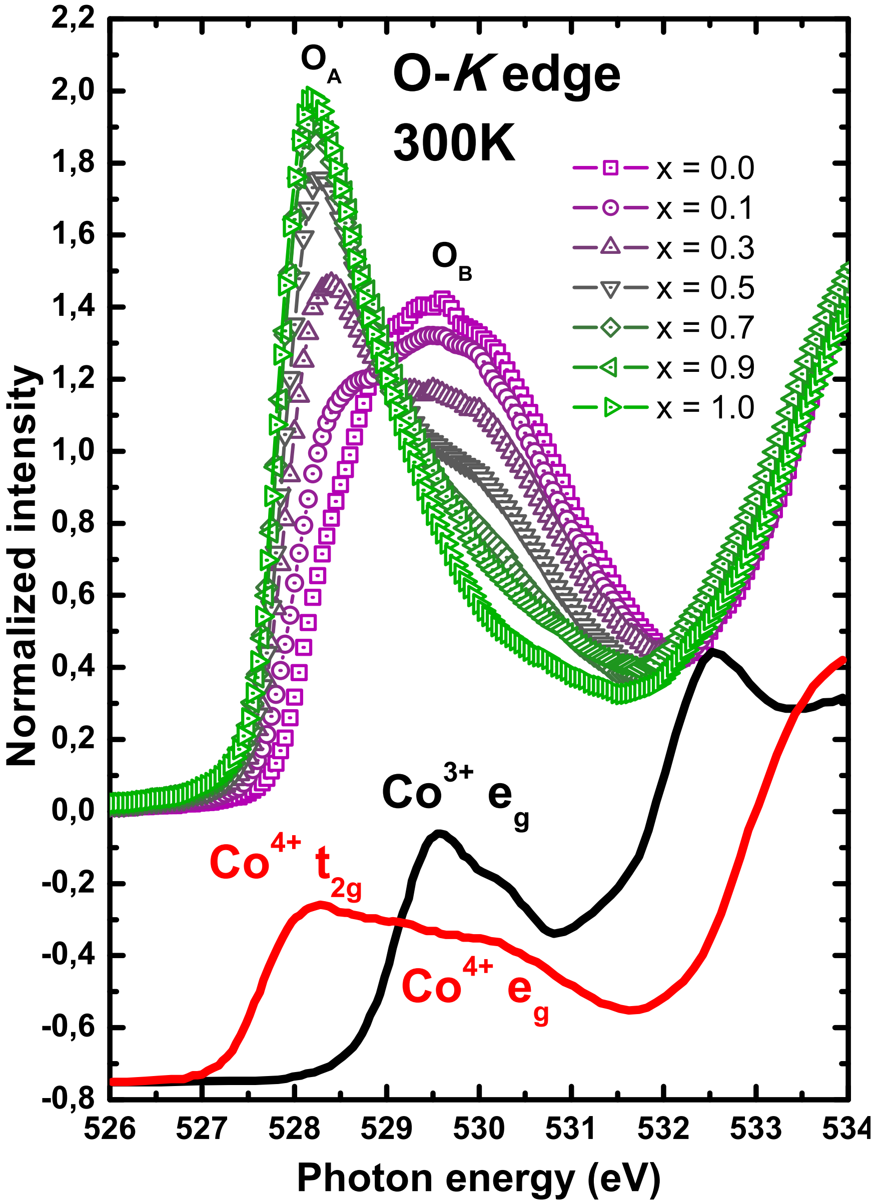

Figure 5.5: The doping dependent O-K spectra for all LaCo$_{1-x}$Ni$_x$O$_3$ compounds. The red and black solid lines (in the lower part in this figure) represent the spectrum of La$_{0.5}$Ca$_{1.5}$CoO$_4$ and La$_{1.5}$Ca$_{0.5}$CoO$_4$, respectively. Both spectra are used as an energy reference, and are taken from Ref. [89].

1.0 end member (LNO), a fully developed peak O$_A$ is observed which is obviously due to the hybridization between the Ni-3d and O-2p states. If one ignores the valence-state change for a moment, the substitution-induced spectral-weight transfer from the peak O$_B$ to the peak O$_A$ may be due to the Ni substitution and/or a spin-state redistribution (see Section 5.1). However, from the discussion in the previous chapter, one also has to take the Co^{4+} species into account since a valence-state change is possibly also present in the LCNO system. The O-K XAS spectra of La$_{1.5}$Ca$_{0.5}$CoO$_4$ and La$_{0.5}$Ca$_{1.5}$CoO$_4$ are plotted in Fig. 5.5 to display the peak positions of Co^{4+} e$_g$, Co^{4+} t$_{2g}$ and Co^{3+} e$_g$ bands. The peak position of the Co^{3+} e$_g$ band was already checked in previous sections. If one compares La$_{0.5}$Ca$_{1.5}$CoO$_4$ with LCNO, one can find that the peak of the Co^{4+} t$_{2g}$ band is also located around 528 eV. The peak position of Co^{4+} t$_{2g}$ almost coincides with the peak position of Ni^{3+}. All this indicates that the spectral-weight transfer may possibly also be caused by a valence-state change. Therefore, the substitution-induced spectral-weight transfer can be ascribed to the fact that the O-K pre-edge spectrum reflects not only a possible spin-state redistribution of Co^{3+} but also a valence-state change in Co [88, 89] and the corresponding Ni unoccupied states. From the discussion above, in the O-K XAS of LCNO, one knows that the high-energy peak can be assigned to the Co^{3+} e$_g$ and the Co^{4+} e$_g$ bands, and the low-energy peak can be assigned to the Co^{4+} t$_{2g}$, Co^{3+} t$_{2g}$ and Ni^{3+} bands. It seems impossible to “disentangle” the various contributions of different species in the O-K XAS. In order to examine the spin state and valence state quantitatively, one needs to perform XAS measurements at the Co- and Ni-$L_{2,3}$ edges. The results will be discussed in the next section.

Such a spectral-weight transfer with doping has been observed in several systems, for instance (LaSr)MO$_3$ (M = Mn, Fe and Co) [91, 92]. This spectral weight transfer may indicates a change in the electronic structure near the Fermi, in other words, the occupied of states above the Fermi level seems to move toward to the Fermi level. A simple model is presented in Fig. 5.6. It may help to explain the metal-insulator transition when $x \geq 0.4$ since it is increasingly easily for an electron to “jump” to the conduction band.

In order to quantitatively study the oxygen ligand hole and the hybridization between O and Co/Ni, we did some further analysis of O-K XAS. In Fig. 5.7 (a), we plot the O-K pre-edge structure after subtraction of the LaCoO$_3$ spectrum. In this figure, the change of spectral weight with Ni substitution can be more directly observed. One can see that the intensity of the high-energy peak (O$_B$) is linearly decreasing with doping level x (blue line in the Fig. 5.7 (c)). Meanwhile, the

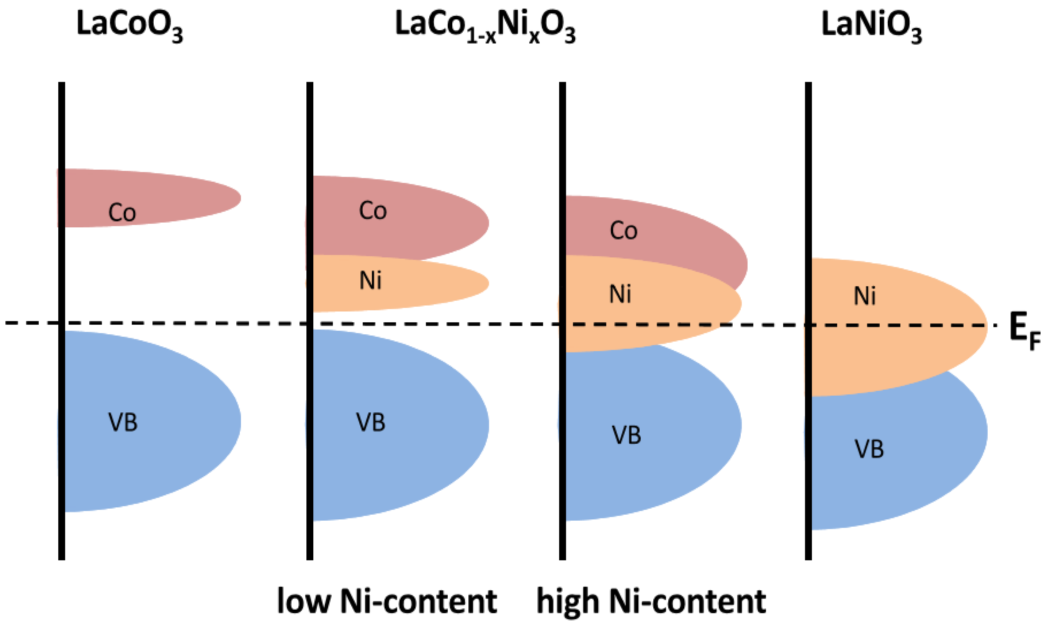

Figure 5.6: Simple model of the doping-dependent density of states around the E$_F$ (loosely based on the energy scheme of Fig. 3.1).

intensity of the low-energy peak is increasing with x(black line in the Fig. 5.7 (c)). With the increase of Ni content, the peak O$_A$ starts dominating in the O-K pre-edge. Interestingly, the increase of the oxygen ligand hole intensity near E$_F$ (feature A, black curve in Fig. 5.7 (c)) has a different slope for x below and above the metal-insulator phase transition. The ground state of LCNO system can be described as $|\Psi\rangle = \alpha|3d^n\rangle + \beta|3d^{n+1}\underline{L}\rangle$, and $\alpha^2 + \beta^2 = 1$. In O-K XAS, the integrated intensity of the pre-edge peak is proportional to β^2, *i.e.* proportional to the hybridization strength. In Fig. 5.7 (b), we show the integration intensity of the pre-edge of all studied samples as a function of Ni content. It clearly depicts that the hybridization strength slightly reduces as $x >$ 0.3. Comparing this finding with the average-bond-angle results, we find that the hybridization between O and Co/Ni reduces with the increase of average bond angle. This indicates that the t$_{2g}$ interaction is dominant in the LCNO system. From this observation, we can deduce that in the low Ni-content regime the ground state is more dominated

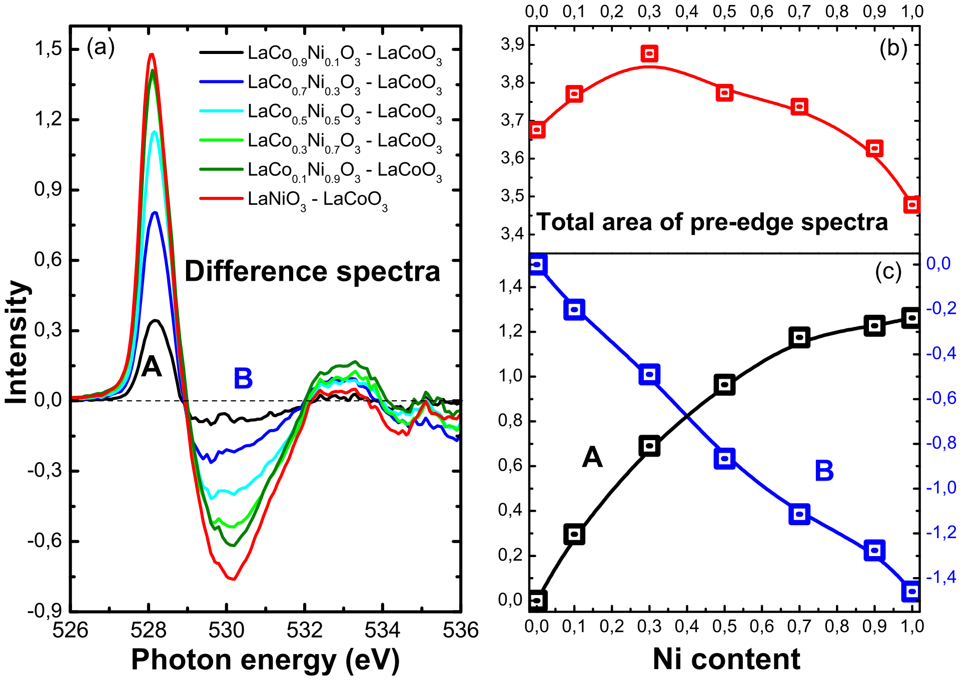

Figure 5.7: (a) Difference spectra of XAS for LCNO and LCO at O-K edge. (b) Integrated intensity of all studied samples as a function of doping level x. (c) The integration intensity of peak A and peak B in the difference spectra as a function of doping level x.

by the $|3d^{n+1}\underline{L}\rangle$ configuration.

5.2.3 Co-$L_{2,3}$ XAS

Figure 5.8 (a) displays the Co-$L_{2,3}$ XAS spectra measured at 300 K as a function of doping level x. As a guide for the valence states and spin state of Co ions, all LCNO XAS spectra are compared with simulated spectra of Co^{2+}, Co^{3+} HS, Co^{3+} LS, Co^{4+} LS and Co^{4+} HS. Peak g is characteristic for octahedral Co^{2+} HS. For all LCNO Co-L spectra, only the spectrum of $x = 0.0$ and 0.1 have a little structure at the low-energy side (grey area in the Fig. 5.8), indicating that there is a little oxygen deficiency in this two samples and no oxygen deficiency for other compositions ($x \geq 0.3$).

Very characteristic is the dominant peak B around 780 eV for Co^{3+}. First, we discuss the spin-state redistribution. There is a simple and useful way to determine the spin state in the mixed spin-state system. Comparing the calculated spectra for Co^{3+} LS and Co^{3+} HS, we see that the difference does not only show in the multiplet structure, but also

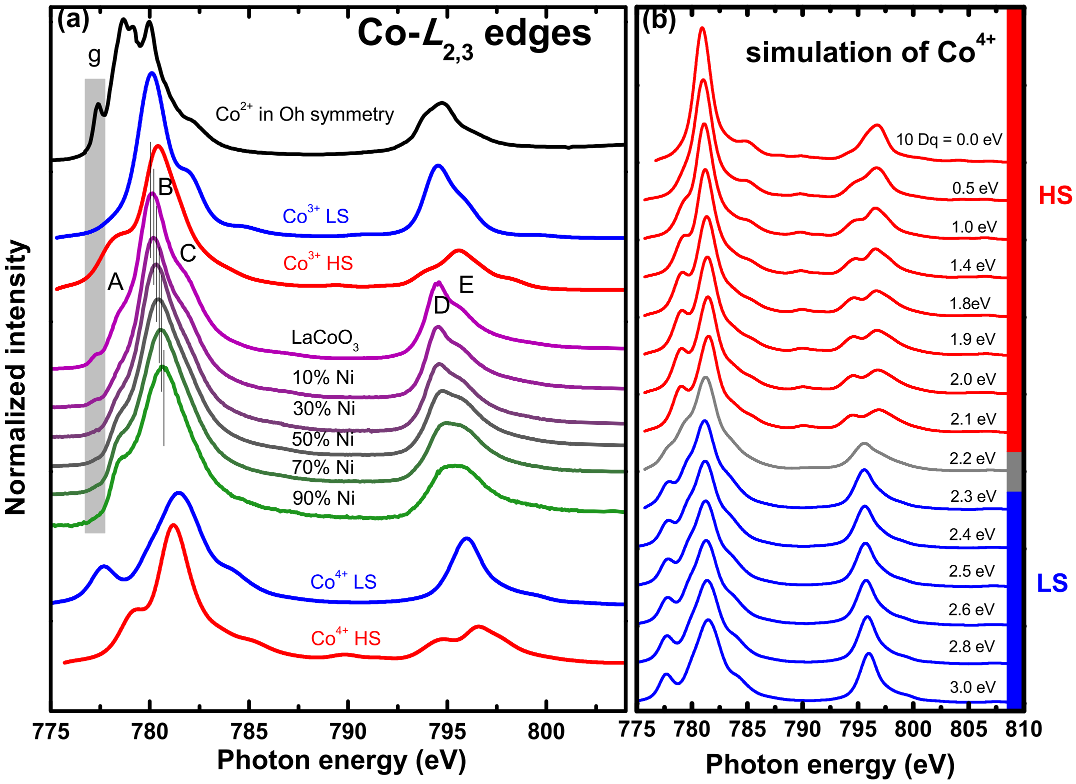

Figure 5.8: (a) The Co-$L_{2,3}$ XAS spectra of LaCo$_{1-x}$Ni$_x$O$_3$ together with the simulation spectra of Co^{3+} LS, Co^{3+} HS, Co^{4+} LS and Co^{4+} HS. (b) Simulation spectra of Co^{4+} in O$_h$ symmetry for different $10D_q$. Red area represents the HS state, blue area represents the LS state and grey area shows the mixture spin state. The spectra are vertically offset for clarity.

in the branching ratio. The branching ratio is defined as I(L_2)/I(L_3), where I(L_3) and I(L_2) is the intensity of L_3 and L_2, respectively. The LS has a higher intensity at the L_2 edge with a rather sharp peak E, that is, the branching ratio in the LS state is larger that that in the HS state. We have observed a branching ratio change in the Ni-substitution sample: the branching ratio for the 90% Ni sample is smaller than that of LaCoO$_3$. This suggests that there must be a spin-state redistribution in the LCNO system. More specifically, we clearly observe that the spectral weight of peak C reduces and that of peak A slightly increases, indicating that the spin state must change from LS to HS since the Co^{3+} LS has more (less) pronounced intensity in peak C (A) just like we see in Fig. 5.3. It is perhaps clearer to observe the LS to HS redistribution if we shift our attention to the L_2 edge. In the LCNO system, the intensity of peak

D reduces considerably with x from a peak to a shoulder, meanwhile the peak E is slightly increased. Since the structure D in the Co^{3+} LS spectrum is a sharp peak, not a shoulder, we can quickly conclude that the spin state of Co^{3+} is transferred from LS to HS with x. Next, we check for a change of the valence state. An energy shift was observed. It is perhaps most clear at Peak B. For each sample we put a black line in the peak B representing the center of gravity of the L_3 spectral weight, and we observe a shift of $\sim$ 0.4 eV for the 90% Ni sample compared to LaCoO$_3$. It is well known that XAS at the L edges is very sensitive to the valence state [93-95]. The energy difference between the $3d^6$ (Co^{3+}) and the $3d^5$ (Co^{4+}) configuration is ΔE = E($2p^6 3d^5 \rightarrow 2p^5 3d^6$) - E($2p^6 3d^6 \rightarrow 2p^5 3d^7$) $\approx U_{pd}$ - $U_{dd} \approx$ 1-2 eV. It means that the peak position is expected to shift toward higher energies by $\sim$ 1 eV if the nominal valence of Co changes from +3 to +4. Hence, the observation of an energy shift in our XAS data clearly indicates an increase in the formal valence of Co.

In order to study the change of valence state (energy shift) and the spin-state transition (spectral shape change) with Ni doping quantitatively, we have carried out theoretical simulations by utilizing the CTM4XAS program to simulate the XAS data. The detailed discussion will be presented in Section 5.2.5.

Possible spin state of Co^{4+} in the LCNO system

The possible spin states of Co^{3+} are well understood nowadays. The Co^{3+} IS only exists in the case of strong tetragonal distortion [14], and can be ruled out in the LCNO system since the local structure of LCNO is O$_h$. From the discussion above, one knows that there is some fraction of Co^{3+} turning to Co^{4+} upon Ni substitution. However, the possible spin states of high valence Co^{4+} are still unclear so far. For the high covalency of Co^{4+}, the charge-transfer energy is in the negative regime due to the stronger hybridization with the oxygen band. For this case, Potze *et al.* [96] have claimed that the ground state is dominated by a $\beta|\mathrm{d}^6\underline{L}\rangle$ state, leading to a Co^{4+} IS state in SrCoO$_3$. Indeed, a hypothetical state with completely transferred ligand hole would have the energy -7J_{ex}-14D_q, -10J_{ex}-4D_q and -10J_{ex}+6D_q for Co^{4+} LS, IS and HS, respectively. In this situation, IS would be the ground state instead of HS. But, as mentioned above, this simple consideration requires a very strong Co-O hybridization. In order to clarify the Co^{4+} IS issue experimentally, one can compare the total integrated intensity of the O-K pre-edge for all studied samples since the integrated intensity reflects the hybridization strengths (to a certain degree). The pre-edge area does not change very much, indicating that the hybridization strength will not be strongly modified compared to LCO. Second, electronic configuration calculations and calculation for the Tanabe-Sugano diagram of Co^{4+} in O$_h$ symmetry for different $10D_q$ have also been performed with the CTM4DOC program. The Tanabe-Sugano diagram is plotted in Fig. 5.9, and the most dominant electronic configurations for different $10D_q$ are listed in Table 5.1. From the Tanabe-Sugano diagram, one clearly sees that the ground state of Co^{4+} is either HS or LS. Further, if one checks the electronic configuration listed in Table 5.1, one can find that when $10D_q \leq 2.1$ eV the Co^{4+} HS state is dominant in the LCNO system. On the other hand, when the $10D_q$ is above 2.1 eV, the Co^{4+} HS will turn into Co^{4+} LS. A visualized picture of the electronic configurations of the Co^{4+} HS and LS states is displayed in Fig. 5.10. All this indicates that only Co^{4+} HS and LS states can exist in the O_h symmetry.

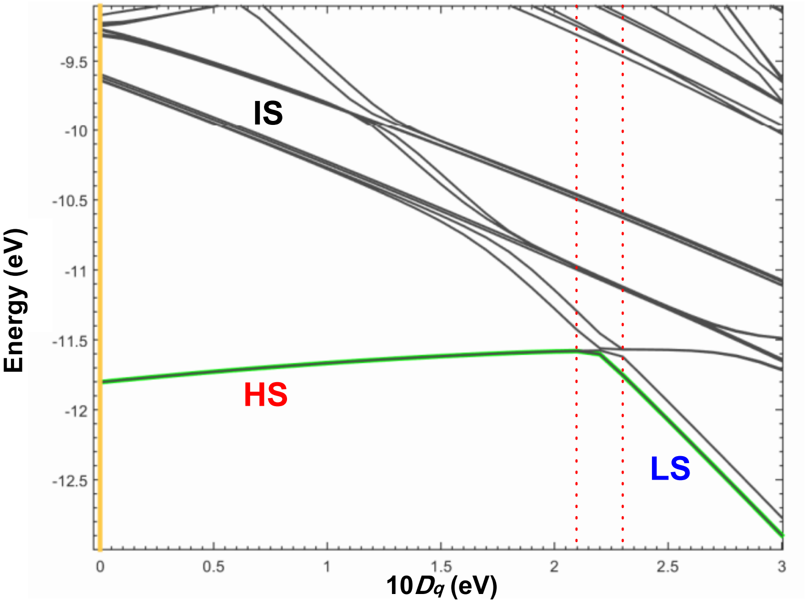

Figure 5.9: Tanabe-Sugano diagram for Co^{4+}.

Next, one has to clarify which species (Co^{4+} HS or Co^{4+} LS) may

	Strongest components of the electronic configuration of Co^{4+}					
$10D_q$	$\|t_{2g}{}^3e_g{}^2\rangle$	$\|t_{2g}{}^3e_g{}^3\underline{L}\rangle$	$\|t_{2g}{}^4e_g{}^2\underline{L}\rangle$	$\|t_{2g}{}^5e_g{}^0\rangle$	$\|t_{2g}{}^5e_g{}^1\underline{L}\rangle$	$\|t_{2g}{}^6e_g{}^0\underline{L}\rangle$
0.0 eV	50.59	35.81	13.50			
0.5 eV	51.29	33.18	15.40			
1.0 eV	51.72	30.55	17.52			
1.4 eV	51.81	28.46	19.39			
1.8 eV	51.53	26.31	19.39			
1.9 eV	51.33	25.73	22.06			
2.0 eV	50.97	25.09	22.66			
2.1 eV	49.90	24.12	23.20			
2.2 eV	15.41			24.38	32.78	
2.3 eV				36.38	47.76	5.76
2.4 eV				37.29	48.27	6.14
2.5 eV				37.82	48.30	6.49
2.6 eV				38.23	48.18	6.83
2.8 eV				38.87	47.73	7.54
3.0 eV				39.37	47.10	8.31

Table 5.1: Electronic configuration of Co^{4+} in O$_h$ symmetry for different crystal-field energy $10D_q$. All parameters for this calculations are the same as I used in calculating the XAS spectrum which is shown in the Fig. 5.8 (b).

be stable in the LCNO system, or whether both are. The simulated spectrum of the Co^{4+} LS shows a clear peak at lower energy ($\sim$ 775.5 eV), but no peak appears around this energy for all compositions of the LCNO family. It clearly indicates that Co^{4+} LS does not exist in the LCNO system. Accordingly, one can summarize that the Co^{4+} HS is the dominant Co^{4+} species in the LCNO system.

5.2.4 Ni-$L_{2,3}$ XAS

La background

The raw Ni-$L_{2,3}$ XAS spectra are shown in the left of Fig. 5.11. As we already saw in the overview scan of LaCo$_{0.5}$Ni$_{0.5}$O$_3$ (see Fig. 5.4), a strong absorption peak at 3 eV below the Ni-L_3 absorption peak is due to the La-M_4 absorption edge. The La-M_4 signal is shown by the LaCoO$_3$ spectrum (black line) in the left of Fig. 5.11. In order to obtain the pure Ni-L_3 peak, we subtract the pure La-M_4 peak from the raw Ni-$L_{2,3}$ XAS spectra. The resulting spectra (net Ni XAS spectra) are shown in the right of Fig 5.11 for all doping levels x. To the best of our knowledge,

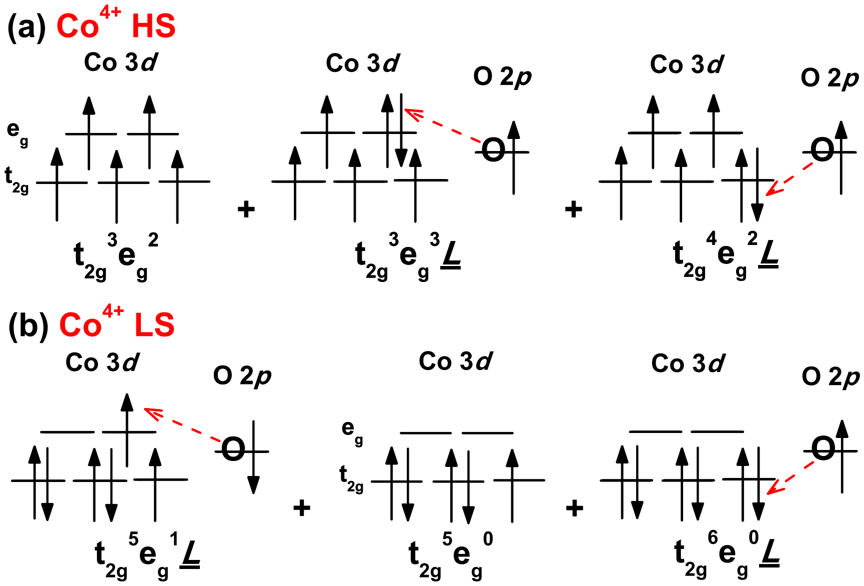

Figure 5.10: Schematic electronic configuration for the Co^{4+} HS and Co^{4+} LS. In the sketches for the dynamics processes involving ligand holes the respective states after the hopping process depicted by the arrow is shown.

this is the first observation of XAS at Ni-$L_{2,3}$ for the LCNO system.

Evolution of Ni-$L_{2,3}$ XAS

Figure 5.12 displays the normalized XAS spectra at Ni-$L_{2,3}$ measured at 300 K as a function of doping level x. In the Ni-$L_{2,3}$ XAS, one can observe a gradual change upon increasing the Ni content. The spectral weight of the high-energy component both at the L_3 edge (peak L) and the L_2 edge (peak N) increases rapidly with x, becoming the dominant feature for $x > 0.5$. In the low doping range ($x \leq 0.5$), one can observe that both the L_3 and L_2 edges split into two peaks (K and L in L_3; M and N in L_2), and gradually merge into one peak with shoulder in the high Ni-content region. The increasing low-energy peak (K) from LaNiO$_3$ to LaCoO$_3$ can be understood as follows: (i) Contribution of Ni^{3+} HS: The electronic structure of the rare-earth nickel perovskites RNiO$_3$ is dependent on lattice distortions, in particular the Ni-O-Ni bond angle (see Chapter 1). When the Ni-O-Ni bond angle is close to 180°, the metallic phase is favored. On the other hand, the insulating phase is stabilized when the Ni-O-Ni bond angle decreases. Piamonteze *et al.* [97] have reported that the ground state of Ni is transferred from an

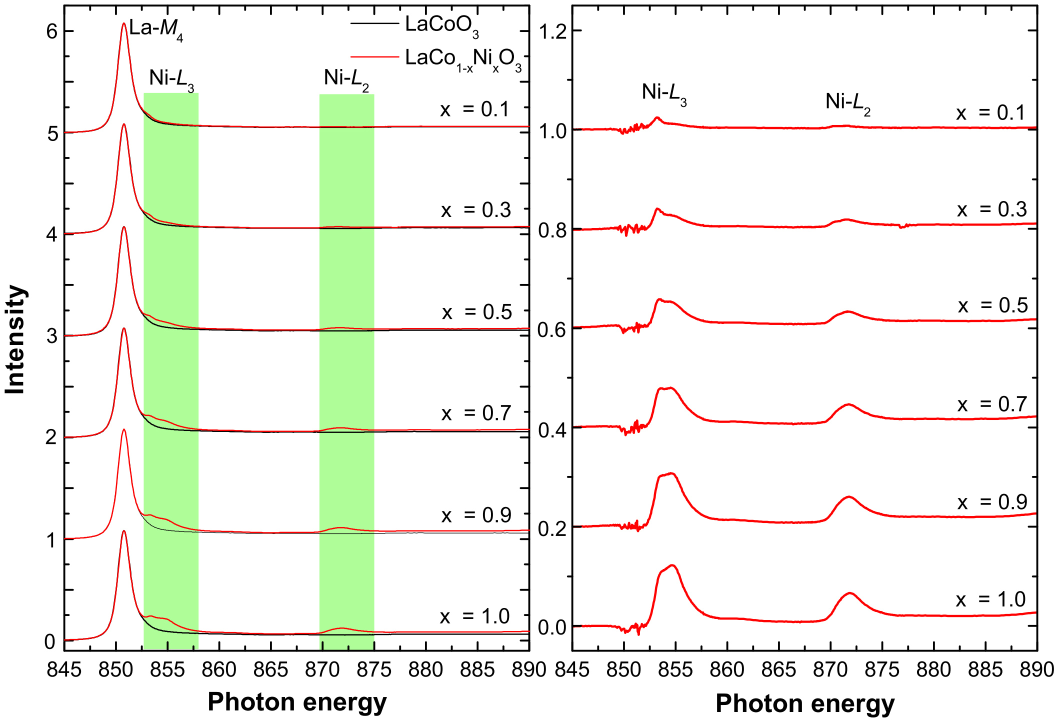

Figure 5.11: Left: Raw data of LaCo$_{1-x}$Ni$_x$O$_3$ at Ni-$L_{2,3}$ together with pure La-M_4 peak taken from LaCoO$_3$. Right: Subtracted XAS spectra of Ni-$L_{2,3}$ for LaCo$_{1-x}$Ni$_x$O$_3$. The spectra are vertically offset for clarity.

essentially LS state to a mixed-spin state (LS + HS) from the metallic to the insulating phase. In the mixed-spin state, a decrease of the crystal field splitting leads to a double-peaked structure at both the L_3 and L_2 edge. Since the bond angle is reduced by about 1% compared to LaNiO$_3$ and since a larger energy-splitting has been observed in the low Ni-content sample, we can give a quick conclusion that the spin state of Ni is also gradually changed from LS in LaNiO$_3$ to a mixed-spin state in LaCo$_{0.9}$Ni$_{0.1}$O$_3$. (ii) Contribution of Ni^{2+}: Ni ions tend to trap electrons from Co ions, introducing Ni^{2+} + Co^{4+} due to the large electronegativity of Ni. One electron is transferred from Co^{3+} HS to Ni^{3+} HS, resulting in the existence of Co^{4+} HS and Ni^{2+}. The existence of Co^{4+} HS is confirmed by the Co-$L_{2,3}$ XAS. Therefore, we also have to take into account the species of Ni^{2+}. In order to obtain more detailed information on the local electronic structure of Co and Ni, theoretical simulations have been performed to fit the experimental data and will be discussed in the next section.

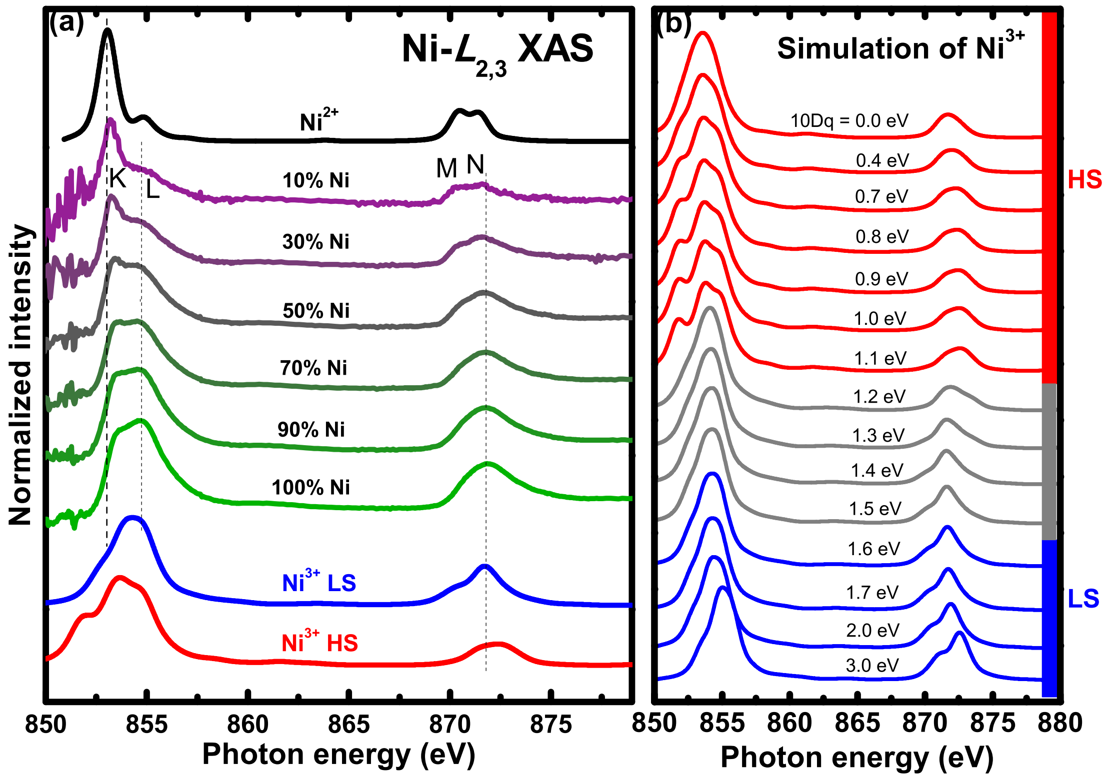

Figure 5.12: (a) The Ni-$L_{2,3}$ XAS spectra of LaCo$_{1-x}$Ni$_x$O$_3$ together with the simulation spectra of Ni^{2+}, Ni^{3+} LS, and Ni^{3+} HS. (b) Simulation spectra of Ni^{3+} in O$_h$ symmetry for different $10D_q$. Red area represents the HS state, blue area represents the LS state and grey area shows the mixture spin state. The spectra are vertically offset for clarity.

5.2.5 Doping-dependent valence-state change and spin-state redistribution

As we have seen above, the multiplet structures for different valence states and spin states are very different. This different structure makes it possible for us to extract detailed information on valence and spin states. If one wants to determine the valence and spin state, one can superimpose the calculated spectra of different species in a proper ratio to simulate the experimental XAS. To demonstrate how this analysis method works, I use LaCo$_{0.5}$Ni$_{0.5}$O$_3$ as an illustrative example. Based on the above discussions in Sections 5.2.3 and 5.2.4, one already knows that it contains Co^{3+} HS, Co^{3+} LS and Co^{4+} HS at the Co sites, and Ni^{2+}, Ni^{3+} LS and Ni^{3+} HS at the Ni sites. One can directly superimpose

	Strongest components of the electronic configuration of Ni^{3+}				
$10D_q$	$\vert t_{2g}{}^5 e_g{}^2\rangle$	$\vert t_{2g}{}^5 e_g{}^3 \underline{L}\rangle$	$\vert t_{2g}{}^4 e_g{}^3\rangle$	$\vert t_{2g}{}^6 e_g{}^1\rangle$	$\vert t_{2g}{}^6 e_g{}^2 \underline{L}\rangle$
0.0 eV	56.32	27.81	8.45		
0.4 eV	59.10	27.49	6.48		
0.7 eV	60.71	27.04	5.42		
0.8 eV	61.18	26.86	5.12		
0.9 eV	61.62	26.67	5.22		
1.0 eV	62.04	26.48	5.38		
1.1 eV	62.43	26.27	5.54		
1.2 eV	24.22	10.19		33.46	29.00
1.3 eV	12.96	5.46		43.42	35.73
1.4 eV	7.61	3.23		48.29	38.78
1.5 eV	4.90	2.10		50.90	40.21
1.6 eV	3.40			52.47	40.89
1.7 eV	2.50			53.54	41.20
2.0 eV	1.24			55.49	41.25
2.1 eV	1.12			55.96	41.13
2.4 eV	1.01			57.16	40.62
3.0 eV	0.85			59.14	39.30

Table 5.2: Electronic configuration of Ni^{3+} in O$_h$ symmetry for different crystal-field energies $10D_q$. All number shown in this table are in %.

calculated spectra[1] in a proper ratio of Co^{3+} LS, Co^{3+} HS and Co^{4+} HS to simulate the Co-$L_{2,3}$ XAS spectrum and in a proper ratio of Ni^{3+} HS, Ni^{3+} LS and Ni^{2+} to simulate the Ni-$L_{2,3}$ XAS spectrum. The simulation results for LaCo$_{0.5}$Ni$_{0.5}$O$_3$ are depicted in Fig. 5.13, and the simulations show that the XAS shape in this case is a mixture of 38% Co^{3+} HS + 42% Co^{3+} LS + 20% Co^{4+} HS configuration at the Co site, 16% Ni^{3+} HS + 66% Ni^{3+} LS + 18% Ni^{2+} configuration at the Ni site.[2] This finding of a mixed valence state at Co and Ni is new and interesting, and is in contrast to previous reports [98-100].

Previous works [101] have reported that the spin state of the Ni ions in LaNiO$_3$ is LS. The electronic configuration of Ni is t$_{2g}^6$e$_g^1$ (LS) because the very small value for the charge-transfer energy Δ causes strong hybridization between O-2 p_σ and Ni^{3+} e$_g$ orbitals and thus an itinerant

---

[1] The calculated spectra of Co^{3+} LS, Co^{3+} HS, Co^{4+} HS, Ni^{2+}, Ni^{3+} LS and Ni^{3+} HS are already shown in Figs. 3.4, 5.8 and 5.12, and all calculated spectra are consistent with previous works [14, 13].

[2] In this simulation, I used the simulated spectrum of Co^{3+} LS taken from Fig. 3.4 with $10D_q$ =1.5 eV, that of Co^{3+} HS taken from Fig. 3.4 with $10D_q$ =0.9 eV, that of Co^{4+} HS taken from Fig. 5.8 (b) with $10D_q$ =1.4 eV, that of Ni^{3+} LS taken from Fig. 5.12 (b) with $10D_q$ =1.7 eV, that of Ni^{3+} HS taken from Fig. 5.12 with $10D_q$ =0.8 eV and that of Ni^{2+} taken from Fig. 3.5 (b3).

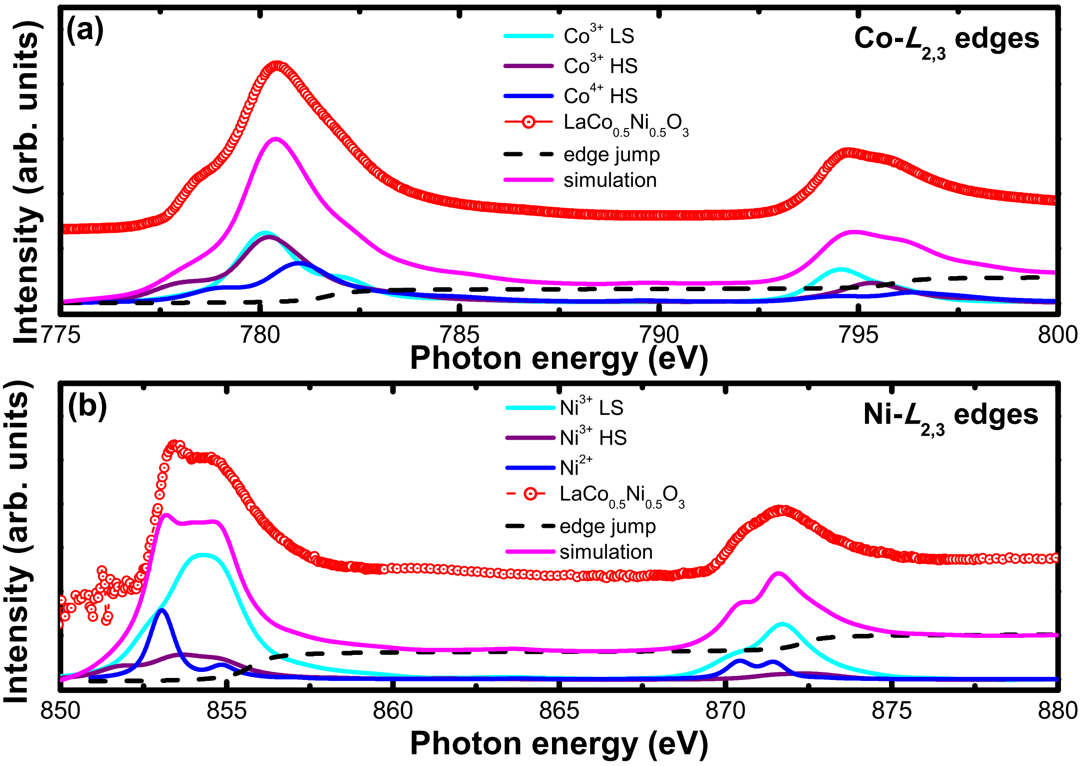

Figure 5.13: Comparison of experimental spectrum with simulated spectrum at (a) Co- and (b) Ni-$L_{2,3}$ XAS spectrum. Red circles represent the experimental data and the solid magenta line represents the simulated spectrum. In the Co XAS data, the cyan line, purple line and blue line represent the Co^{3+} LS, Co^{3+} HS and Co^{4+} HS, respectively. In the Ni XAS data, the cyan line, purple line and blue line represent the Ni^{3+} LS, Ni^{3+} HS and Ni^{2+}, respectively.

nature of the e$_g$ electrons ($d^7 \rightarrow d^8\underline{L}$). In other words, the strong covalency will stabilize the low-spin state for Ni^{3+} in O$_h$ symmetry. Indeed, in our calculations of the electronic configuration for Ni^{3+} LS with Δ = 1.0 eV, the ligand-hole component is very strong ($\sim$ 40%, see Table 5.2). However, according to the multiplet calculation of Ni^{3+} LS in O$_h$ symmetry, we find that the calculated spectrum has less spectral weight in peak K (see Fig. 5.12 (b)) compared to experimental data. Hence, it is plausible that still a few % of Ni^{3+} HS are contained in LaNiO$_3$.

In order to study the valence change and spin-state redistribution with Ni substitution, the same method as used for the LaCo$_{0.5}$Ni$_{0.5}$O$_3$ case (Fig. 5.13) has been applied to all LCNO compounds. I found that the average valence of Co and Ni increases linearly with doping level x from Co$^{+2.97}$ to Co$^{+3.34}$ and from Ni$^{+2.7}$ to Ni$^{+3.0}$, respectively. Meanwhile, the spin state is gradually redistributed from LS to HS for Co and from HS to LS for Ni. The values of valence state and spin state for all compositions are summarized in Table 5.3.

Valence state

	x= 0.0	x= 0.1	x= 0.3	x= 0.5	x= 0.7	x= 0.9	x= 1.0
Co	+2.97	+3.01	+3.10	+3.20	+3.28	+3.34	
Ni		+2.70	+2.78	+2.82	+2.91	+2.96	+3.0

Spin state

	x= 0.0	x= 0.1	x= 0.3	x= 0.5	x= 0.7	x= 0.9	x= 1.0
Co^{2+} HS	3%	2%	0%	0%	0%	0%	0%
Co^{3+} HS	29%	28%	33%	38%	39%	40%	0%
Co^{3+} LS	68%	67%	57%	42%	33%	26%	0%
Co^{4+} HS	0%	3%	10%	20%	28%	34%	0%
Ni^{3+} HS	0%	19%	18%	16%	8%	5%	3%
Ni^{3+} LS	0%	51%	60%	66%	83%	91%	97%
Ni^{2+}	0%	30%	22%	18%	9%	4%	0%

Table 5.3: Valence-state and spin-state configurations, derived from XAS and multiplet calculations, as a function of Ni content,

5.3 Temperature effects

The temperature is also a critical factor which influences the sample structure. According to neutron and x-ray diffraction, the average bond length and average bond angle decreases significantly with decreasing temperature in LCO [102-104] compared to LNO sample. In this case, one could expect that the spin-state transition may be more pronounced in the low Ni-content samples. Next, we will discuss the effect of temperature on LaCo$_{1-x}$Ni$_x$O$_3$.

5.3.1 Temperature-dependent O-*K* spectra

The temperature-dependent O-*K* XAS spectra measured at 20 K and 300 K are shown in Fig. 5.14. We first compare the two end member samples, *i.e.*, $LaCoO_3$ and $LaNiO_3$. Similar to the discussions in Section 5.1, one already sees a significant change in spectral weight at $LaCoO_3$ O-*K* XAS caused by the temperature-dependent spin-state transition. For the other end member $LaNiO_3$, however, we observed no change in the spectral shape between 20 K and 300 K. This strongly implies that there is no spin-state transition of Ni in $LaNiO_3$.

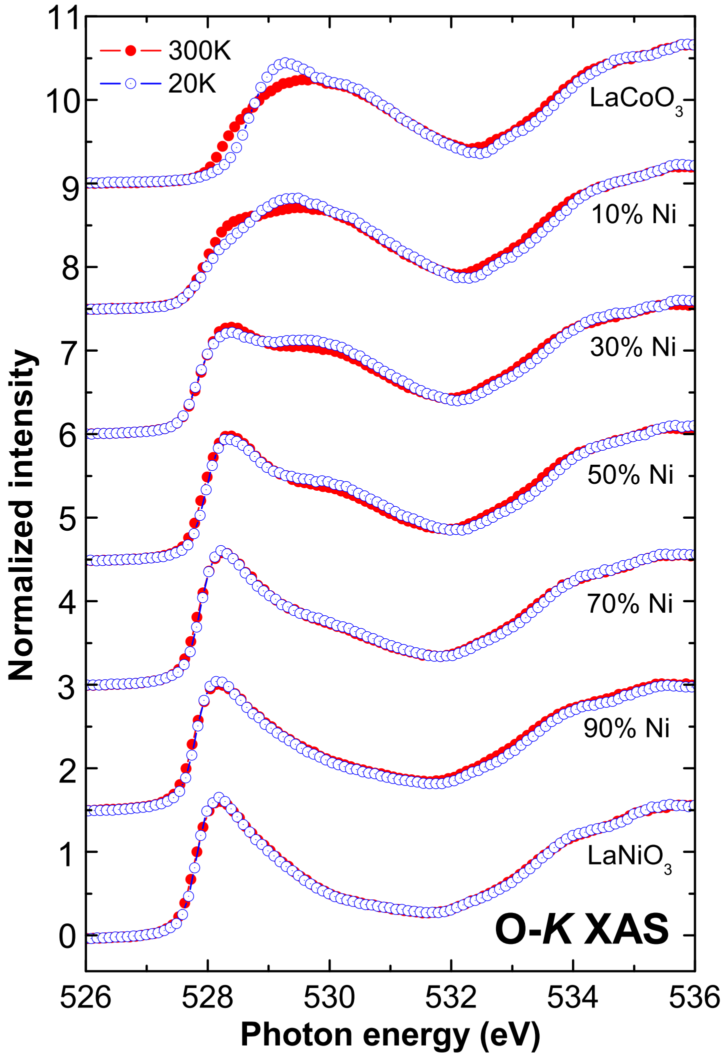

Figure 5.14: Temperature-dependent O-*K* XAS spectra of $LaCo_{1-x}Ni_xO_3$. The spectra are vertically offset for clarity.

Next, we discuss the Ni-doping system. One can clearly observe a spectral weight transfer up to $x \leq 0.5$ similar to what is observed for the LaCoO$_3$ sample. It indicates that a spin-state transition can be induced with temperature in the low Ni-content regime. In contrast, the spin state will be fixed when the Ni content exceeds 50 % in the LCNO system since we barely see any changes in the spectral shape. However, it is difficult to separate the contribution of Co from that of Ni at the O-K edge. Hence, we need temperature-dependent XAS measurements at the Co- and the Ni-$L_{2,3}$ edges as well to clarify the temperature-dependent spin-state transition.

5.3.2 Temperature-dependent spin-state transitions

Figure 5.15 shows the temperature-dependent XAS spectra at (a) the Co- and (b) the Ni-$L_{2,3}$ edges. At the Co sites, a spin-state transition is clearly observed up to $x \leq 0.5$. This is consistent with the observation at the O-K edge, where the spin-state transition only appears in the low Ni-content regime. Notably, the energy of the main peak does not change with temperature, meaning there is no change in the valence state. In contrast to the Co result, we see no changes in the spectral shape of the Ni spectra between low and high temperature for all doping levels x. It strongly implies that there is no spin-state transition at the Ni sites. The main reason which causes the different behavior at the Co and the Ni site is: The $\langle TM\text{-O}\rangle$ decreases with decreasing temperature, leading to an increase in the crystal field. If one examines the change on the electronic configuration as a function of $10D_q$ for Co^{3+} (Table 3.2) and Ni^{3+} (Table 5.2), one can find that the spin state of Co^{3+} is more sensitive to a change of $10D_q$.[3] Since the Co ion is more sensitive than the Ni ion to the changes of the crystal field, it suggests that the decreasing temperature will induce a spin-state transition from HS to LS only for Co^{3+}. Further, according to neutron and x-ray diffraction measurements [25, 102-104], the average-bond-length $\langle TM\text{-O}\rangle$ and the average-bond-angle $\langle TM\text{-O-}TM\rangle$ will change significantly in LaCoO$_3$ but will barely change in LaNiO$_3$ with decreasing temperature. This clearly implies that the structure will not exhibit a significant change for the high Ni-content sample. The temperature-dependent XAS measurements are consistent with neutron and x-ray diffraction results.

---

[3] For Co^{3+}, the spin state will be easily changed from HS to LS if $10D_q$ changes from 1.2 eV to 1.3 eV. However, for Ni^{3+}, the HS will totally transfer to LS only if $10D_q$ changes from 1.1 eV to 1.6 eV.

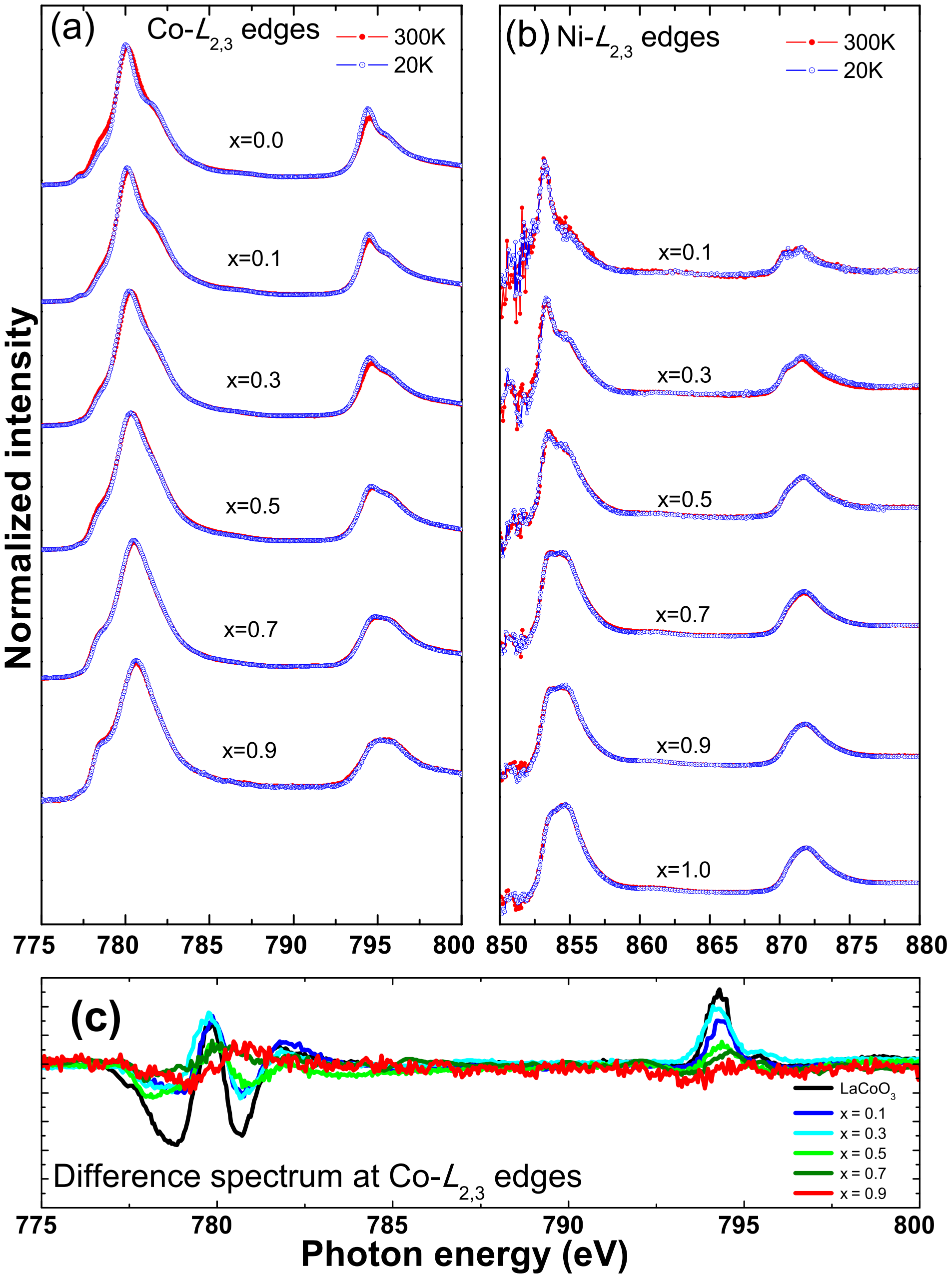

Figure 5.15: Temperature-dependent XAS spectra at (a) Co- and (b) Ni-$L_{2,3}$ edges for all LaCo$_{1-x}$Ni$_x$O$_3$ compounds. (c) shows the difference spectra at the Co-$L_{2,3}$ edges. In the difference spectra, one can clearly observe that the spectral shape barely changes when $x \geq 0.5$, especially at the L_2 edge. The temperature-dependent spectra of Co and Ni are vertically offset for clarity.

In order to determine the spin-state transition quantitatively, the multiplet calculations have also been performed to fit the low temperature XAS spectra at the Co- and the Ni-$L_{2,3}$. The results will be shown in the following section together with the results of the doping-dependent spin-state redistribution.

5.4 Summary of XAS measurements

5.4.1 Spin-state and valence-state change

According to the XRD refinement, we have observed a change in average bond length ($\langle TM\text{-O}\rangle$) (leading to a change in the crystal-field energy $10D_q$) and average bond angle ($\langle TM\text{-O-}TM\rangle$). The structural change may induce a spin-state redistribution. On the other hand, a substitution of Co by Ni with its larger electronegativity will give rise to a partial electron transfer from Co to Ni ($\text{Co}^{3+} + \text{Ni}^{3+} \rightarrow \text{Co}^{3+\delta} + \text{Ni}^{3-\delta}$). The spin-state change and valence-state change upon Ni substitution was confirmed by XAS measurements. Figure 5.16 (a) - (c) summarizes the change of valence state and spin state as a function of Ni content. From the viewpoint of LaCoO$_3$, the HS spin state component Co^{3+} slightly increases with increasing Ni content. In contrast to Co ions, the LS spin state component of Ni^{3+} slightly increases with increasing Ni content. Further, upon Ni substitution, XAS results clearly indicate a mixed-valence state for both Co and Ni ions, and both the valence of Co and Ni increase monotonically with the Ni content x ($\text{Co}^{+2.97} \rightarrow \text{Co}^{+3.34}$ and $\text{Ni}^{+2.70} \rightarrow \text{Ni}^{+3.0}$). Besides the Ni substitution, the temperature is also a critical factor which influences the structure of the compound. Temperature-dependent XAS measurements imply that there is a spin-state transition only at the Co ions. Figure 5.16 (b) shows the spin-state transition of Co with temperature. Remarkably, the temperature-dependent spin-state transition of Co is suppressed in the highly Ni-doped regime. This behavior is similar to that of the strained LaCoO$_3$ thin films, where the Co^{3+} HS component is “clamped” by the applied strain. [15, 105, 106]

The resistance measurements are also consistent with the XAS results. There is a metal-insulator transition around $x = 0.4$. The small or even negative charge-transfer energy is important for the metallicity. The $3d$ level of highly oxidized transition-metal ions such as Co^{4+} and Ni^{3+} is deep and close to the O $2p$ level. Therefore, LCNO with more Co^{4+} and Ni^{3+} ($x > 0.4$) favors a metallic state.

5.4.2 Average radius

In Chapter 4, we have seen that the average bond length increases with increasing x and decreases again when $x > 0.5$. At that point, it was

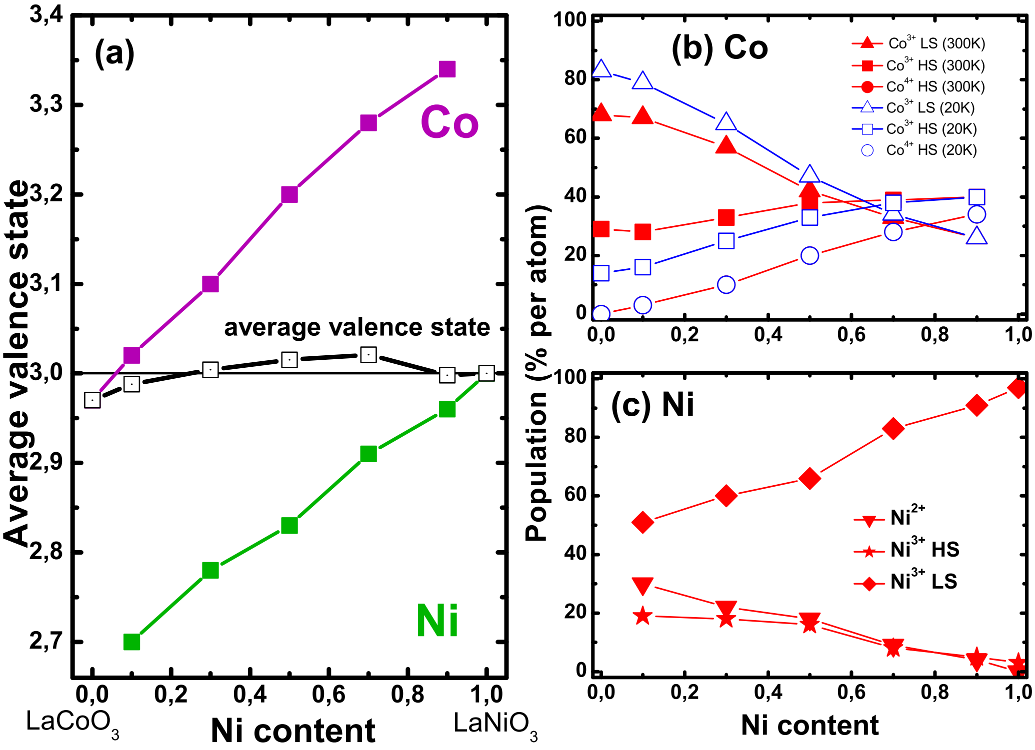

Figure 5.16: (a) The valence-state change for Co and Ni as a function of Ni content. The average valence state for all compositions is close to +3, indicating a good stoichiometry of oxygen. (b) The doping-dependent spin-state redistribution and temperature-dependent spin-state transition at the Co sites. (c) The doping-dependent spin-state redistribution at the Ni sites.

perhaps a little difficult to understand why the average bond length decreases again in the high Ni-content regime. Here, since one already knows the fraction of all different species in the LCNO system derived from the XAS data (see Table 5.3), one can simply calculate the average radius of the central *TM* ion for all compositions using Table 4.2. Figure 5.17 shows the average radius of the central *TM* ion calculated in this way as a function of the Ni content. This plot clearly shows an increase in the low Ni-content regime and a decrease in the high Ni-content regime. It is consistent with the XRD results shown in Fig. 4.3. The reason for the decrease of the average bond length in the high Ni-content regime is: At the Co site, the fraction of Co^{3+} HS (with larger radius) barely changes with increasing x, meaning that the average radius of Co (Co^{3+} HS + Co^{3+} LS + Co^{4+} HS) is almost a constant in the high Ni-content regime. In contrast to the Co ions, the fraction of Ni^{3+} LS (with smaller radius) increases rapidly, meaning that the average radius of Ni (Ni^{2+} + Ni^{3+} LS + Ni^{3+} HS) decreases with increasing x in the high Ni-content regime.

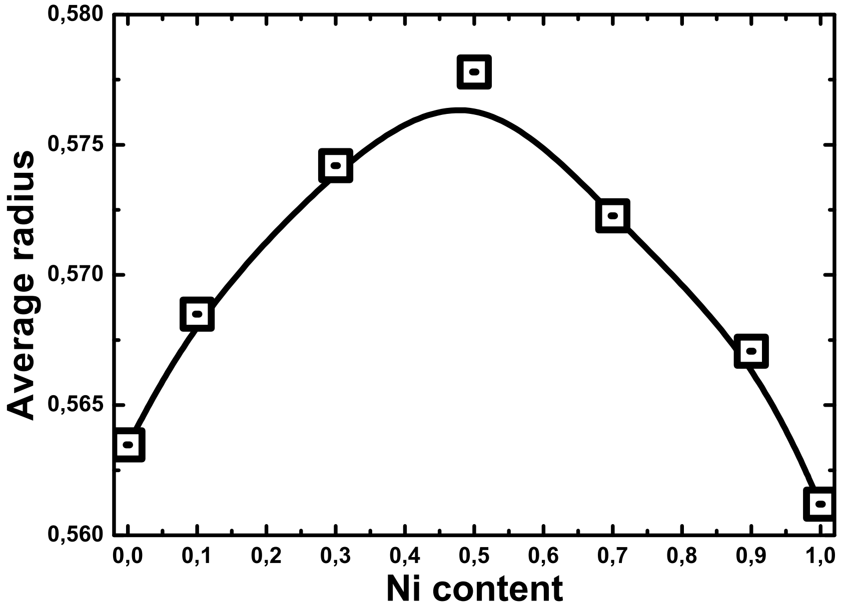

Figure 5.17: Average radius of the central *TM* ion derived from the XAS data.

5.4.3 Possible hopping processes

For a further study of the magnetic behavior, we need to clarify the hopping processes. According to the multiplet calculations, different species possess different "fingerprints" in XAS spectra. XAS measurements provide a time-averaged picture, so if electron hopping leads to different species, all of them will show up in XAS, superimposed and in intensities corresponding to the dwell times. So, based on the XAS measurements, we can check how many and what species exist in the studied sample. In the discussion above, we have deduced that LCNO contains Co^{3+} LS, Co^{3+} HS, Co^{4+} HS, Ni^{2+} HS, Ni^{3+} LS and Ni^{3+} HS. One can build some simple models of electron donors/acceptors, and then combine them to discuss possible electron-hopping processes. Here, I concentrate mainly on the FM interactions and some AFM interactions are mentioned. Figure 5.18 lists all simple models for electron donors and acceptors.

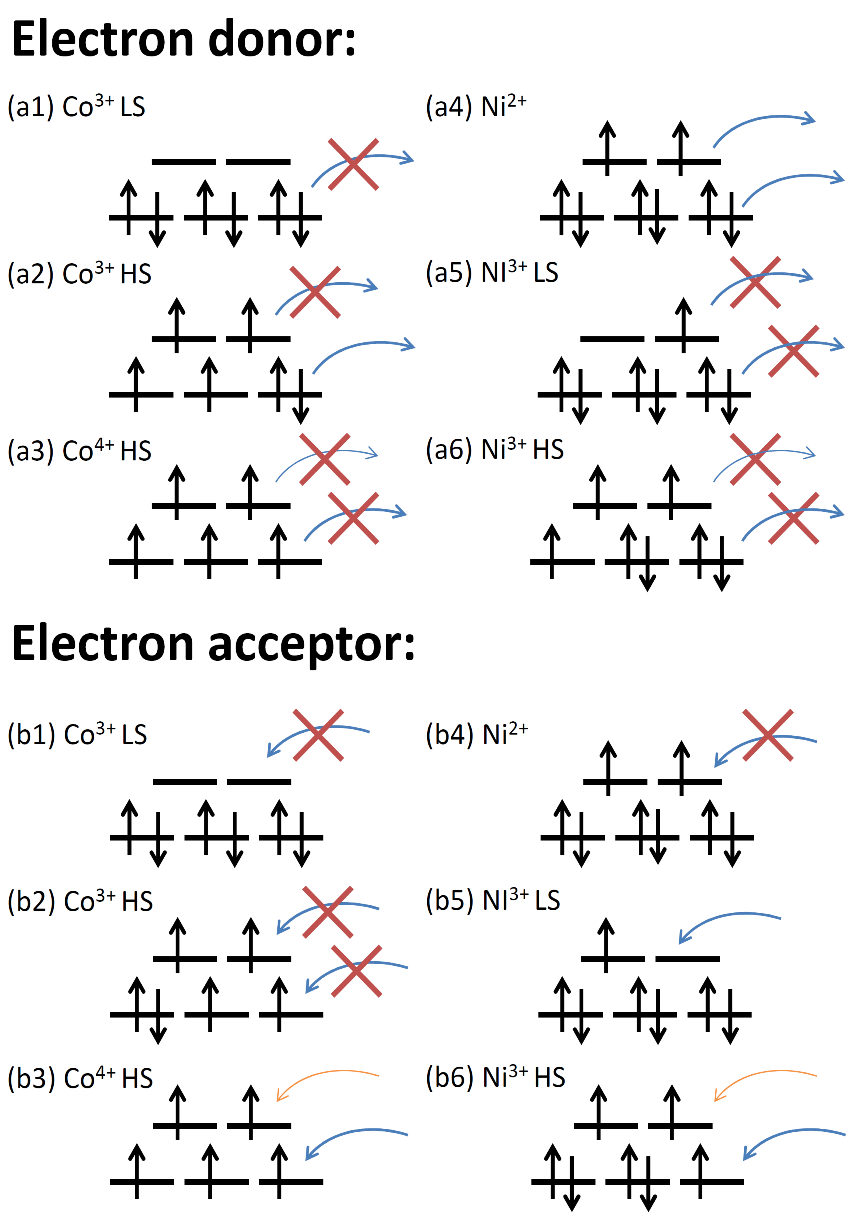

Figure 5.18: Simple models of electron donors and electron acceptors for different species. Blue lines represent a ferromagnetic interaction and the orange lines represent an anti-ferromagnetic interaction.

Firstly, we discuss the electron-donor models.

- (a1): Co^{3+} LS: All electrons are in the t$_{2g}$ level. If one electron is transferred from Co^{3+} LS t$_{2g}$ to other species, it results in a Co^{4+} LS. This hopping process is impossible since we did not observe any features of Co^{4+} LS in Co-$L_{2,3}$ XAS.

- (a2): Co^{3+} HS: There are four electrons in t$_{2g}$ and two electrons in e$_g$. If one electron hops from a Co^{3+} HS e$_g$ to another species, this will result in a Co^{4+} IS. However, as discussed above, Co^{4+} IS is not stable in O$_h$ symmetry. So, this hopping process can be ruled out. On the other hand, if one electron hops from t$_{2g}$ to another species, this creates a Co^{4+} HS. This hopping behavior is possible since we have observed Co^{4+} HS in the LCNO system.

- (a3): For Co^{4+} HS, there is no possibility for electrons to hop to other species since no Co^{5+} exists in the LCNO system.

- (a4): There are two possible hopping channels for Ni^{2+}. The first is that one e$_g$ electron moves to other species resulting a Ni^{3+} LS, and the second is that one t$_{2g}$ electron transfers out giving rise to Ni^{3+} HS.

- (a5) and (a6): There is no option for an electron to move to other species from Ni^{3+} because it will create a Ni^{4+} in the LCNO system.

Then, we examine the electron-acceptor models.

- (b1) and (b2): It is impossible for Co^{3+} to receive one electron because there is no observation of Co^{2+} in the LCNO system (apart from the slight contribution for $x < 0.3$ caused by a small oxygen deficiency, see Section 5.2.3).

- (b3): It will be an excited state if one electron hops to the Co^{4+} HS e$_g$ band, and this interaction is an AFM interaction. On the other hand, electrons can hop to the Co^{4+} HS t$_{2g}$ levels, creating a Co^{3+} HS (see Fig. 5.10 (a)).

- (b4): It is impossible for electrons hopping to Ni^{2+} because it will create a Ni^{1+} in the LCNO system which is not observed.

- (b5): Electrons are likely transferring to the Ni^{3+} LS e$_g$ bands, and leave a Ni^{2+}.

- (b6): Electrons can hop to the Ni^{3+} HS t$_{2g}$ bands, leading to Ni^{2+}. However, it will be a excited state if electrons hop to the Ni^{3+} HS e$_g$ bands, and this is an AFM interaction.

Combining the electron-donor models and electron-acceptor models, it turns out that the possible hopping paths for FM interaction (blue lines in Fig. 5.19) in LCNO are Co^{3+} HS $\leftrightarrow$ Co^{4+} HS via t$_{2g}$, Co^{3+} HS $\leftrightarrow$ Ni^{3+} HS via t$_{2g}$, Ni^{2+} HS $\leftrightarrow$ Co^{4+} HS via t$_{2g}$, Ni^{2+} $\leftrightarrow$ Ni^{3+} LS via e$_g$ and Ni^{2+} $\leftrightarrow$ Ni^{3+} HS via t$_{2g}$, and that some possible hopping paths for AFM interaction (orange lines in Fig. 5.19) are Ni^{2+} $\leftrightarrow$ Ni^{3+} HS via e$_g$ and Ni^{2+} $\leftrightarrow$ Co^{4+} HS via e$_g$. All these possible hopping paths are summarized in Fig. 5.19.

After understanding the valence states, spin states, and possible hopping paths, we can next turn to investigate the ferromagnetic behavior in the LCNO system by utilizing XMCD measurements.

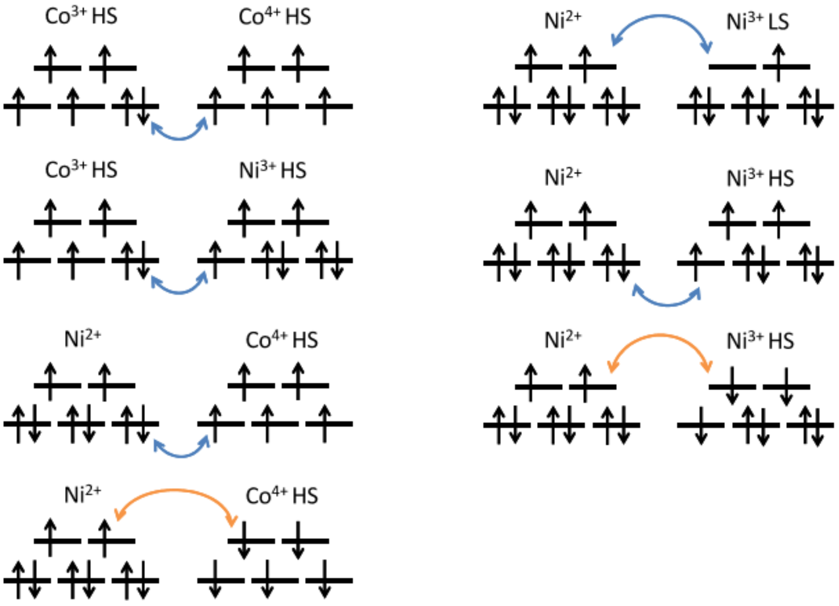

Figure 5.19: Simple possible hopping paths deduced from XAS analysis. Blue lines represent the ferromagnetic interaction and the orange lines represent the anti-ferromagnetic interaction. The anti-ferromagnetic interaction between Co^{3+} HS - Co^{3+} HS and Ni^{3+} HS - Ni^{3+} HS is not shown in this figure.

Chapter 6

Results III: Magnetic properties in $LaCo_{1-x}Ni_xO_3$ – SQUID and XMCD results

The nature of the magnetic properties in the LCNO system has been investigated for decades. However, the magnetic interaction is still a puzzle in this system. A very direct way to probe the ferromagnetic interaction is by XMCD measurements. In this chapter, the XMCD results are given to understand the magnetic properties in the LCNO system. To our knowledge, this work is the first one to report on XMCD measurements for LCNO. Part of the reason is that it is particularly difficult to extract an XMCD signal at the Ni-$L_{2,3}$ edges due to the huge La background.

6.1 SQUID measurements

In order to determine the ferromagnetic transition temperature T_C, temperature-dependent magnetization measurements (M(T)) with field cooling (FC) have been done in the temperature range of 5 K to 300 K. All M(T) measurements were performed by Dr. D. Fuchs[1]. Figure 6.1 exhibits the M(T) results for all LCNO compounds, and only the results in the temperature range of 0 K to 100 K are plotted. The T_C's for all LCNO samples were determined by the minimum of the derivative

---

[1] Institut für Festkörperphysik, Karlsruher Institut für Technologie

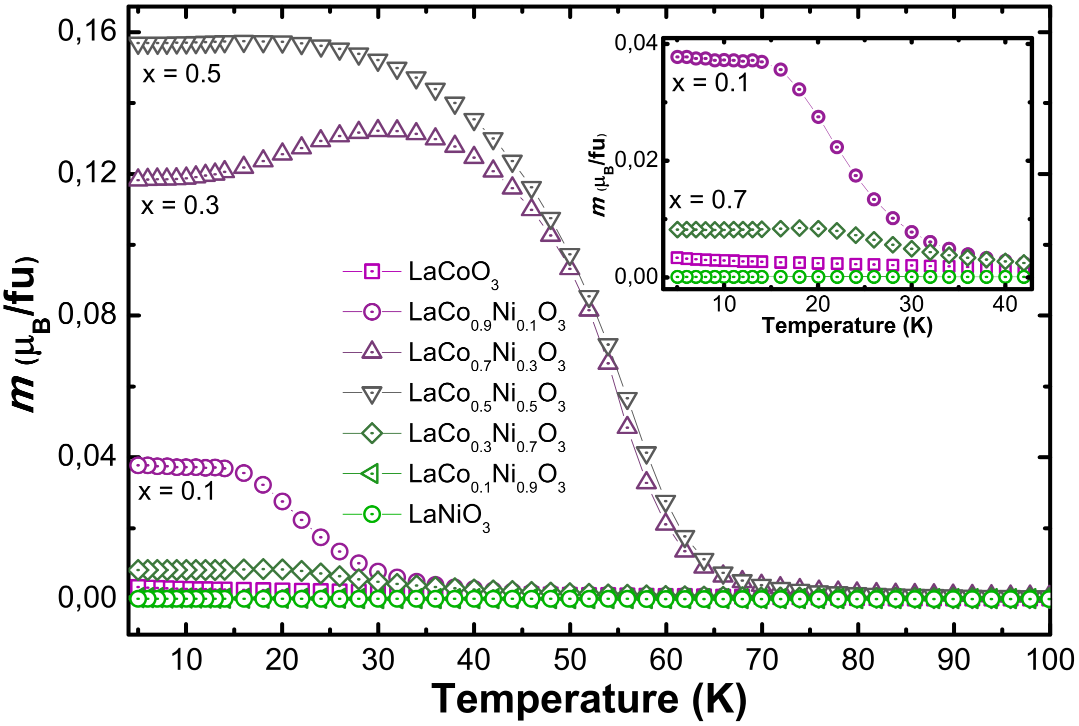

Figure 6.1: Temperature dependence of the FC magnetization (M-T) for all studied samples at H = 100 Oe. A magnified version of the data in the lower left corner is shown in the inset.

dM/dT and are displayed in Table 6.1.

x	0.0	0.1	0.3	0.5	0.7	0.9	1.0
T$_C$	N	20 K	54 K	57 K	25 K	N	N

Table 6.1: The values for the ferromagnetic transition temperature T$_C$ derived from the FC curves. “N” means there was no ferromagnetic transition observed.

6.2 XMCD measurements

In order to resolve the magnetism issue and get insights into the individual spin and orbital moments of Co and Ni in the LCNO system, element-specific XMCD measurements were carried out on all studied samples at 10 K with a magnetic field $B = \pm 4$ T. The measurement temperature is well below any of the T$_C$'s observed, and the applied

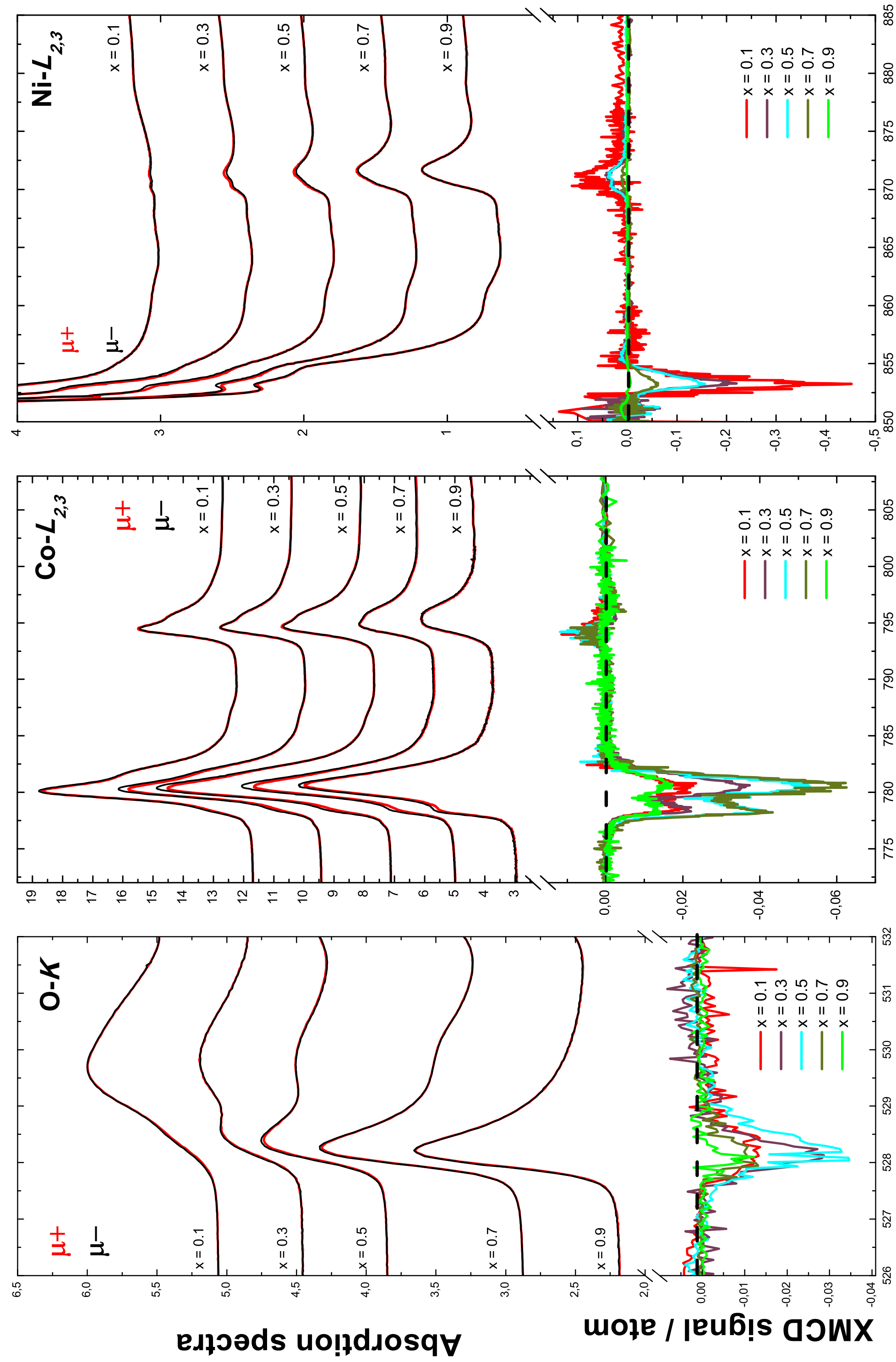

Figure 6.2: XMCD results together with XAS spectra of (a) O-K, (b) Co-$L_{2,3}$ and (c) Ni-$L_{2,3}$. The XAS spectra are vertically offset for clarity.

magnetic field is sufficient to saturate the spin moment. XMCD measurements were performed in the total-electron yield mode at the Co-L, Ni-L, and O-K edges with a degree of circular polarization of about 80% (see Chapter 2). In Fig. 6.2, I present the XMCD results at the O-K, Co-$L_{2,3}$, and Ni-$L_{2,3}$ edges together with the XAS spectra for all studied samples. The huge background at the Ni-L_3 edge, due to La-M_4, was already observed for XAS (Chapters 3 and 5) but will make XMCD even more difficult. Still, it turned out possible to extract XMCD spectra even there.

6.2.1 XMCD at Co- and Ni-$L_{2,3}$ edges

At first sight, one can observe that the XMCD shape does not change at both the Co- and Ni-L edges for all LCNO samples, meaning that the character of the ferromagnetic interaction behavior does not change for any of the samples. In order to qualitatively analyze the ferromagnetic character in LCNO system, simulations of XMCD spectra have also been performed by utilizing the CTM4XAS program. Figure 6.3 displays the simulated XMCD spectra for all species (Co^{3+} LS, Co^{3+} HS, Co^{4+} LS, Co^{4+} HS, Ni^{3+} LS, Ni^{3+} HS and Ni^{2+}). The parameters for the XMCD calculations are the same as those used for calculating the XAS spectra. As mentioned in the XRD and XAS parts, the change of bond length $\langle TM\text{-O}\rangle$ will change the crystal-field energy ($10D_q$). So, for XMCD calculations, I also have simulated the XMCD spectra in a certain range of $10D_q$ values, to be able to fit all LCNO systems. Figure 6.4 shows the XMCD results at Co- and Ni-$L_{2,3}$ of LaCo$_{0.5}$Ni$_{0.5}$O$_3$ together with the simulated spectra of Co^{3+} HS ($10D_q$ = 0.9 eV), Co^{4+} HS ($10D_q$ = 1.4 eV), Ni^{2+}, Ni^{3+} LS ($10D_q$ = 1.7 eV) and Ni^{3+} HS ($10D_q$ = 0.8 eV) for comparison. We observe that the XMCD signal is largely negative at both the Co- and Ni-L_3 edges, meaning that the Co and Ni spins are aligned ferromagnetically. I first discuss the Co XMCD results. Since both Co^{3+} HS and Co^{4+} HS have a net spin moment (Co^{3+} HS: S = 2; Co^{4+} HS: S = 5/2), one needs to clarify which species (Co^{3+} HS or Co^{4+} HS) participates in the ferromagnetic interaction, or whether both do. At the L_3 edge, one can see a double-peaked structure (peak a and b). In the simulated spectra of Co^{3+} HS and Co^{4+} HS, one also can observe a double-peaked structure (although for both simulations, the low-energy peak has a much smaller intensity than the experimental

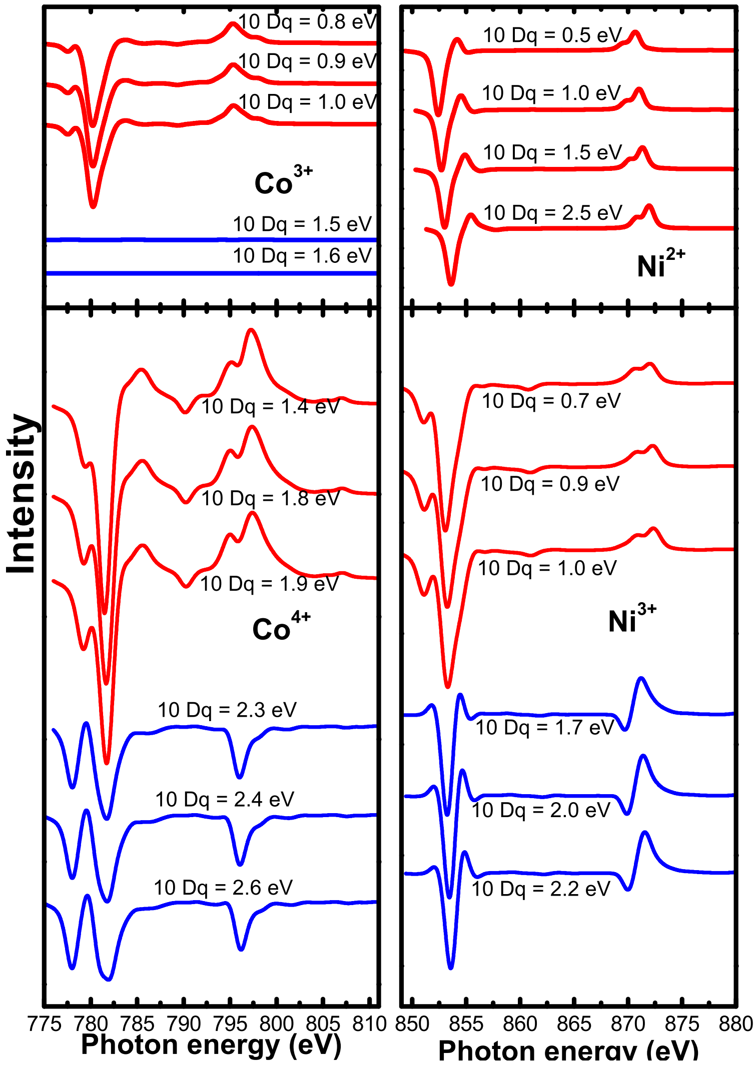

Figure 6.3: Simulations of XMCD spectrum for all species. Red and blue line represent the HS and LS state, respectively. The adopted parameters for XMCD calculations are the same as used in the XAS calculations. The spectra are vertically offset for clarity.

peak a). However, if one compares the peak energy (peak a and b) of the simulated spectra with the experimental results, it is obvious that only the simulated Co^{3+} HS spectrum can describe the experimental XMCD to a reasonable degree. At the L_2 edge, we only observe a single positive peak (peak c) in the experimental XMCD. This spectral shape at the L_2 edge is totally different from that of the Co^{4+} HS simulated spectrum which shows double-peak structure at the L_2 edge. Based on the discussion above, it is most likely that among the Co species, predominantly the Co^{3+} HS ions participate in the ferromagnetic interaction in LCNO. Interestingly, the XMCD signal of Co is very small at L_2 edge, which, according to sum rule analysis, indicating that the ratio of orbital to spin moment must be large.

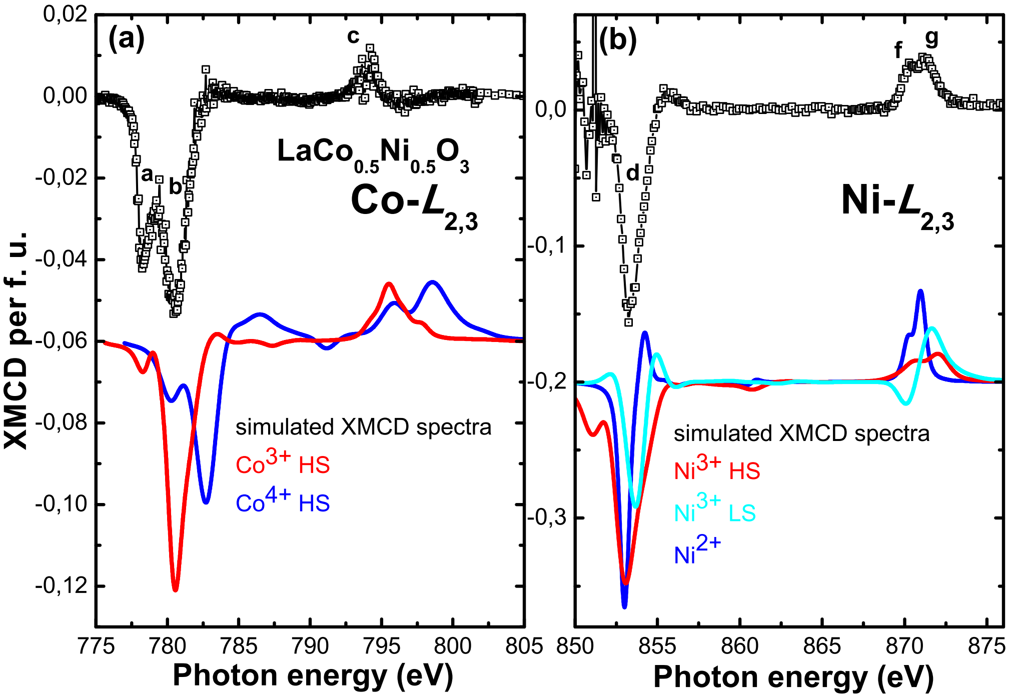

Figure 6.4: XMCD data at (a) Co-$L_{2,3}$ and (b) Ni-$L_{2,3}$ of LaCo$_{0.5}$Ni$_{0.5}$O$_3$ together with calculated XMCD spectra for different species.

Turning now to Ni, there are three different cases: Ni^{3+} HS ($S = 3/2$), Ni^{3+} LS ($S = 1/2$) and Ni^{2+} ($S = 1$). In order to clarify which species participates most strongly in the ferromagnetic interaction, the experimental XMCD results are also discussed together with the simulated spectra of Ni^{2+}, Ni^{3+} LS, and Ni^{3+} HS. In Fig. 6.4, one can find that the calculated XMCD of Ni^{3+} with $10D_q = 0.8$ eV fits the experimental data well. If one compares the simulation with the experiment (Fig. 6.4 (b)), all structures (peak d, peak f and peak g) can be reproduced. On the other hand, the spectral shape of Ni^{2+} seems to fit the experimental data almost as well (although the widths of the features generally appear too small), so perhaps a superposition of the two species might describe the experiment best. Two observations, however, indicate that Ni^{2+} is unlikely to be an important contribution to the ferromagnetic interaction here: first, the Ni^{3+} HS / Ni^{2+} ratio changes strongly with x (see Table 5.16), yet the XMCD shape remains almost the same for all x; and second, according to Fig. 5.19, Ni^{2+} would be able to interact ferromagnetically with Co^{4+} HS but the latter does not contribute to Co-L XMCD. Therefore, we can deduce that the XMCD data is predominantly due to Ni^{3+} HS. Combining this result for Ni with the one for Co above, one can conclude that the ferromagnetic interaction is caused by Co^{3+} HS and Ni^{3+} HS. Considering the electronic configuration of these species, a "double-exchange-like" mechanism between the two seems to be at work.

6.2.2 XMCD at the O-*K* edge

It is useful to perform the XMCD measurements also at the O-K edge since the magnetic interaction is mediated by O ions. The O-K XMCD data for all LCNO samples are shown in Fig. 6.2 (a). One can observe a strong negative XMCD peak with an intensity that amounts to several percent of the total XAS intensity of the t$_{2g}$ region. The O-K MCD signal is mainly attributed to the 3d orbital moment on the neighboring sites (*i.e.* Co or Ni ions) interacting through the p-d hybridization [107]. That is, the t$_{2g}$ feature in O-K edge XMCD reflects the transfer of a t$_{2g}$ electron's orbital moment from Co or Ni to the O site. Because of the absence of spin-orbit splitting for the 1s core level, the O-K XMCD spectra show merely the orbital moment but are insensitive to the spin moment. Hence, the integral area of the O-K XMCD is directly proportional to the orbital moment. Since the XMCD results are negative indicating a positive magnetic moment ($m_{orb} > 0$), the orbital magnetic moment of O 2p is parallel to that of Co/Ni 3d.

6.3 Ferromagnetic interaction

In the previous chapter, we already determined all possible electron hopping paths (see Fig. 5.19). Here, we can further combine the XMCD data with XAS results to understand the ferromagnetic interaction in the LCNO system. Based on the XMCD measurements at Co-$L_{2,3}$ and Ni-$L_{2,3}$, we know now that the ferromagnetism is a "double-exchange-like" interaction between Ni^{3+} HS and Co^{3+} HS. O-K, moreover, confirmed that the ferromagnetic interaction between the TM ions is mediated by

O and seems to occur mainly via t_{2g} orbitals.[2] A hopping process consistent with all these observations is shown in Fig. 6.5.

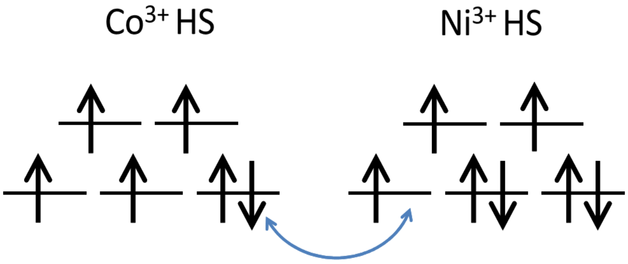

Figure 6.5: Double-exchange like ferromagnetic interaction between Ni^{3+} HS and Co^{3+} HS.

6.4 Spin and orbital moment

To quantify the elemental spin (m_{spin}) and orbital (m_{orb}) moments of Co and Ni, we applied the established XMCD sum rules to our XMCD data following the analysis process shown in Section 2.4.3. The orbital $m_{orbital}$, spin m_{spin} and the total magnetic moment m_{total} per formula unit (f. u.) of Co and Ni are plotted in Fig. 6.6 (a), and the total magnetic moment (m_{total}) is also plotted together with the magnetization measurement by SQUID for comparison in Fig. 6.6 (b). We find that the curve of total magnetic moment of Co and Ni ions behaves similarly for XMCD and SQUID and that the maximum magnetic moment appears in the range of $x = 0.3$ to 0.5. It clearly indicates that one needs both Co^{3+} HS and Ni^{3+} HS in the system in sufficient quantities in order to ensure long-range ferromagnetic interaction and order in the LCNO system. Notably, there is a magnetic-moment discrepancy between SQUID and XMCD for the $x = 0.1$ sample. We already know that there is a slight oxygen deficiency in this sample, leading to a certain amount of Co^{2+} in $LaCo_{0.9}Ni_{0.1}O_3$ sample. Since the probing depth of TEY measurement is only $\sim$ 10 nm and the Co^{2+} is presumably most concentrated in the

---

[2] On the other hand, an orbital moment on e_g states in O-K might be quenched and hard to see.

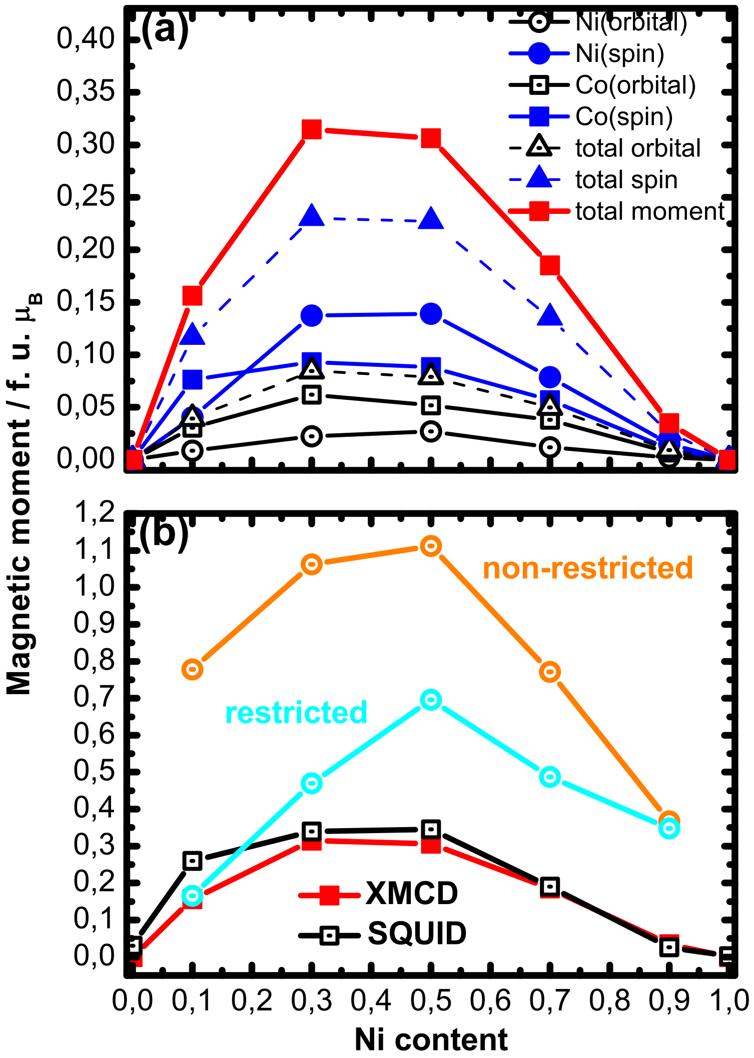

Figure 6.6: (a) shows the individual spin and orbital moment derived from XMCD by using sum rules. (b) The total moment derived from XMCD spectra and SQUID measurement is compared. In this figure, the spin moments derived from two simple theoretical models (non-restricted and restricted model, see text) are also shown.

surface, we get a relatively reduced total moment compared to the bulk SQUID measurements.

Since the XMCD results indicate that the ferromagnetic interaction is induced by a double-exchange-like between Ni^{3+} HS and Co^{3+} HS, we can consider a simple ferromagnetic model of mixing Ni^{3+} HS and Co^{3+} HS, and the equation

$$\mu_{eff} = 4.9 \cdot [(1-x) \cdot (Co^{3+}_{HS})_{popul}] + 3.8 \cdot [x \cdot (Ni^{3+}_{HS})_{popul}] \tag{6.1}$$

provides the total effective spin moment. Here, "$(\mathrm{Co}^{3+}_{HS})_{popul}$" and "$(\mathrm{Ni}^{3+}_{HS})_{popul}$" represents the population of Co^{3+} HS and Ni^{3+} HS in % per atom, respectively, and can be found in Fig. 5.16 (b) and (c). The prefactors 4.9 and 3.8 are the effective spin moment ($\mu_{eff} = 2\sqrt{S(S+1)}$) of Co^{3+} HS ($S = 2$) and Ni^{3+} HS ($S = 3/2$). Assuming that all Co^{3+} HS and Ni^{3+} HS ions participate in the magnetic interaction, one can calculate the effective moment by simply putting the total number of Co^{3+} HS and Ni^{3+} HS into Eqn. 6.1, and the results are plotted in Fig. 6.6 (b) as the trace labeled "non-restricted". For this simple model, one can see that the total spin moment is in the right ballpark but somewhat overestimated. Since the number of Co^{3+} HS ions is sometimes much larger than that of the Ni^{3+} HS ions and since both the Co^{3+} HS and Ni^{3+} HS ions are equally important, one should consider another model case, in which the number of "ferromagnetically active" Co^{3+} HS ions and Ni^{3+} HS ions are the same: neither one can exceed the other. In this case, the numbers of active Co^{3+} HS and Ni^{3+} HS ions are "restricted", meaning that the larger number must be reduced to the smaller one. So in Eqn. 6.1, one calculates the values for (1-x)·$(\mathrm{Co}^{3+}_{HS})_{popul}$ and for x·$(\mathrm{Ni}^{3+}_{HS})_{popul}$, and uses the smaller one in both instances. The results are also plotted in Fig. 6.6 (b) (named "restricted"). One finds that the total spin moment for the restricted case is closer to the actual XMCD results.[3] The fact that the observed moment is still overestimated in the model indicates that not even all Ni^{3+} HS can participate, see comment in Footnote 3. Despite their simplicity and the overestimated numbers the models essentially do capture the evolution of the magnetic moment with Ni doping. Based on this discussion, it means that if the number of Ni^{3+} HS ions can be enhanced, the total magnetic moment will be increased in the LCNO system.

---

[3] In the theoretical calculation, I only can calculate the total spin moment. It is different from XMCD measurements since XMCD measurement can determine the spin and orbital moment individually. In this case, if one compares the cyan curve ("restricted") with the blue triangles (total spin moment) in Fig. 6.6 (a), one can find that the restricted case overestimates the total magnetism. The reason is that not all Ni^{3+} HS is located in sites where there is optimal ferromagnetic interaction. So the populations of the "interacting species" are, in reality, still a little smaller than the "total populations" of the same species.

6.5 Summary of XMCD measurements

To our knowledge, this is the first observation of XMCD in the LCNO system. The XMCD technique provides a direct way to determine the spin and orbital moment of Co and Ni individually. I have observed a strong XMCD signal at both the Co- and Ni-$L_{2,3}$ edges. The XMCD signal is largely negative at both the Co- and Ni-L_3 edges, meaning a ferromagnetic alignment of the Ni and Co species. According to the multiplet calculations, the ferromagnetic interaction in the LCNO system is confirmed and can be attributed to a double-exchange-like mechanism between Co^{3+} HS and Ni^{3+} HS. Further, the XMCD signal also has been observed at O-K in the t$_{2g}$ region. This observation directly implies that the O mediates the exchange hopping between the TM ions. A simple, “restricted” model based on the population of the two interacting species already captures the essence of the evolution of the magnetism with x in the LCNO series.

Chapter 7

Conclusions and future directions

7.1 Summary

In the mixed transition-metal oxide family $\mathrm{LaCo}_x\mathrm{Ni}_{1-x}\mathrm{O}_3$, both end members (parent compounds) are not ferromagnetic: the Co ions in LCO are mostly LS state with $S = 0$, and LNO is the sole paramagnet within the RNO family of antiferromagnets. LaCoO_3, on the other hand, is already very close to ferromagnetism (applying a little strain is enough to obtain FM ordering). The goal of this thesis was to investigate the nature of the ferromagnetism that occurs in the mixed compounds.

To this end, a series of mixed compounds $\mathrm{La(Co,Ni)O}_3$ was synthesized for various values of x. The synthesis was successfully performed by the sol-gel method.

The physical properties of $\mathrm{La(Co,Ni)O}_3$ are highly dependent on the local structure, *i.e.* the average bond length $\langle TM\text{-O}\rangle$ and the bond angle $\langle TM\text{-O-}TM\rangle$. In order to systematically investigate the real structure, the local electronic structure, and the ferromagnetic properties in $\mathrm{LaCo}_{1-x}\mathrm{Ni}_x\mathrm{O}_3$, x-ray diffraction and x-ray spectroscopies have been performed.

According to the XRD measurements, I found that the substitution of Co by the (in general) larger Ni will change the unit-cell volume, the average bond length $\langle TM\text{-O}\rangle$, and the average bond angle $\langle TM\text{-O-}TM\rangle$. The $\langle TM\text{-O}\rangle$ increases from 1.9310 Å for $x = 0.0$ to 1.9390 Å for $x = 0.5$ and then decreases to 1.9318 Å for $x = 1.0$. On the other hand, the $\langle TM\text{-O-}TM\rangle$ slightly decreases from 163.7° to 163.5° between $x = 0.0$ and 0.5, and then significantly increases to 165.7° for $x = 1.0$. These structural changes will induce spin-state redistributions and valence-state changes, leading to a metal-insulator transition and to ferromagnetism.

From XAS, doping-dependent spin-state redistributions and valence-state changes have been observed. By multiplet calculations, we have quantified the populations and spin states for all the species. A mixed valence of both the Co and the Ni ion was found in LCNO, and both the Co and the Ni valence were found to increase continuously with increasing Ni content x. For the doping-dependent spin-state redistribution, the Co^{3+} HS component slightly increases and the Ni^{3+} LS component decreases with increasing x. Furthermore, temperature-dependent spin-state transitions were also observed in LCNO, but only at the Co sites. For $x \leq 0.5$, a fraction of Co^{3+} HS is transferred to LS with decreasing temperature. On the other hand, for $x > 0.5$, the Co^{3+} HS component is almost "clamped" (remains almost constant) even for low temperatures.

To the best of our knowledge, the XMCD at the Co- and the Ni-$L_{2,3}$ edges was the first observation in the $LaCo_{1-x}Ni_xO_3$ system. The XMCD results together with multiplet simulations, and using the quantified Co and Ni species identified before in XAS, allowed us to sequentially exclude possible exchange path candidates for the ferromagnetic interaction. In the end, it was possible to clearly show that ferromagnetic interaction occurs only when and if Co^{3+} HS and Ni^{3+} HS are simultaneously present in sufficient fractions. It suggests a double-exchange-like interaction between Co^{3+} HS and Ni^{3+} HS via t_{2g} levels in LCNO. Perhaps surprisingly, other components present such as Co^{4+} HS with $S = 5/2$ do not participate in the ferromagnetic interaction. Further, according to the O-K XMCD, I also found that the FM interaction is mediated by the O via t_{2g} orbitals.

7.2 Outlook

7.2.1 Enhanced ferromagnetism behavior in $LaCo_{1-x}Ni_xO_3$

Based on this study, the nature of magnetism in LCNO system is very different from that in LCO epitaxial thin films. Unlike what might be assumed at first glance, one cannot just expand the ferromagnetism model of LCO (sufficient fraction of Co^{3+} HS can induce the ferromagnetic interaction) to explain the magnetic interaction in the LCNO system. Instead, the ferromagnetism in LCNO is induced by the interaction between Co^{3+} HS and Ni^{3+} HS. Especially the latter is in very short supply for a range of Ni doping levels, and not even all of Co^{3+} HS and Ni^{3+} HS can participate in the magnetic interaction yet both species are needed in sufficient quantities to support ferromagnetism. This opens a possible avenue for improving the ferromagnetic behavior in LCNO: if one can increase the fraction of Ni^{3+} HS in LCNO (perhaps along with an increase of Co^{3+} HS as well to get all Ni^{3+} HS involved), an enhanced magnetic moment is expected.

7.2.2 Promising cases

$PrCo_{0.5}Ni_{0.5}O_3$ vs. $LaCo_{0.5}Ni_{0.5}O_3$

Similarly to the epitaxial $LaCoO_3$ thin films, ferromagnetism is also induced by growing $PrCoO_3$ on a substrate that applies tensile strain on the film. One may speculate that the spin-state transition to LS for low temperature is again suppressed, leaving enough Co^{3+} HS to support ferromagnetism.[108] Hence, one can expect that the substitution of Co by Ni also induces a ferromagnetic interaction in polycrystalline or bulk $PrCo_{0.5}Ni_{0.5}O_3$ (PCNO). However, in contrast to LCNO, the ionic radius of Pr is smaller than that of La. It will change the average bond angle, leading to a change in the magnetic behavior. Figure 7.1 shows the XAS measurement at the Co-$L_{2,3}$, Ni-$L_{2,3}$, O-K and Pr-$M_{4,5}$ edges for LCNO (black open circle) and PCNO (red solid line). In order to confirm the valence state of Pr, the simulated spectrum of Pr is also plotted together with experimental data. According to the simulation, the Pr-$M_{4,5}$ XAS is in a standard shape corresponding to Pr^{3+} meaning an isovalent replacement of La by Pr in the PCNO system. Figure 7.1 (a) and (b) show the Co- and Ni-$L_{2,3}$ XAS, respectively. We find that there is more Co^{3+} LS and Ni^{3+} LS in the PCNO system. More Co^{3+} and Ni^{3+} LS will weaken the ferromagnetic interaction. Remarkably, I did not observe an XMCD signal at the O-K edge. Instead, a significant XMCD signal appeared at Pr-$M_{4,5}$ edges. This finding suggests that the ferromagnetic interaction is not anymore mediated through O ligands. Instead, Pr now participates strongly in the ferromagnetic interaction, completely changing its character.

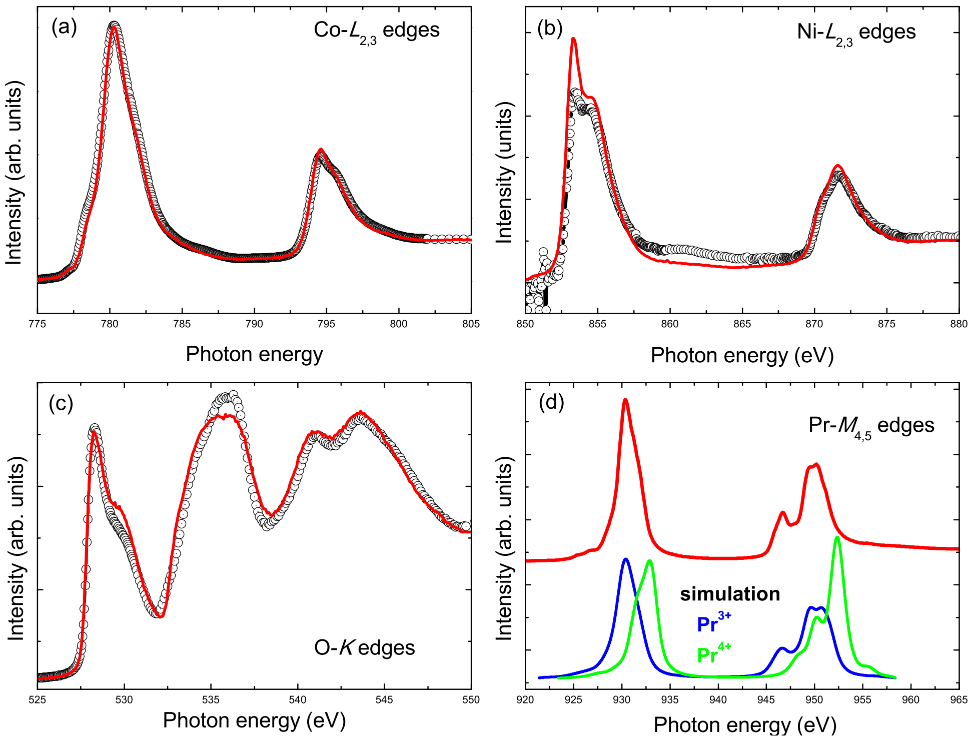

Figure 7.1: XAS measurements of $LaCo_{0.5}Ni_{0.5}O_3$ (black open circle) and $PrCo_{0.5}Ni_{0.5}O_3$ (red solid line) at (a) Co-$L_{2,3}$, (b) Ni-$L_{2,3}$, (c) O-K and (d) Pr-$M_{4,5}$. In the Pr-$M_{4,5}$, we also show the simulation spectrum of Pr^{3+} and Pr^{4+} for comparison. According to the simulation spectrum, it is certain that the valence state of Pr in PCNO system is indeed Pr^{3+}.

$La_{0.85}Ba_{0.15}Co_{0.7}Ni_{0.3}O_3$ vs. $La_{0.85}Ba_{0.15}Co_{0.7}Ni_{0.3}O_3$

Surprisingly, Co^{4+} HS does not seem to take any part in the ferromagnetic interaction in LCNO even though Co^{4+} HS has a very large theoretical spin moment (S = 5/2). In order to understand what the role is that Co^{4+} HS plays in the LCNO system, we doped Ba at the A-site to increase the concentration of Co^{4+} HS. Figure 7.2 shows the XAS measurement at Co-$L_{2,3}$ edges for LCNO (black line) and $La_{0.85}Ba_{0.15}Co_{0.7}Ni_{0.3}O_3$ (LBCNO) (red line). According to the discussion of energy shifts at the Co-$L_{2,3}$ edges in the Chapter 5.2,3, we know that the energy shift implies a valence-state change. Since the main peak energy of LBCNO shifts toward the high-energy side compared to LCNO, this indicates that the Co^{4+} fraction has indeed increased in LBCNO sample. Interestingly, the XMCD measurements (not shown) at the Co-L edge in the LBCNO

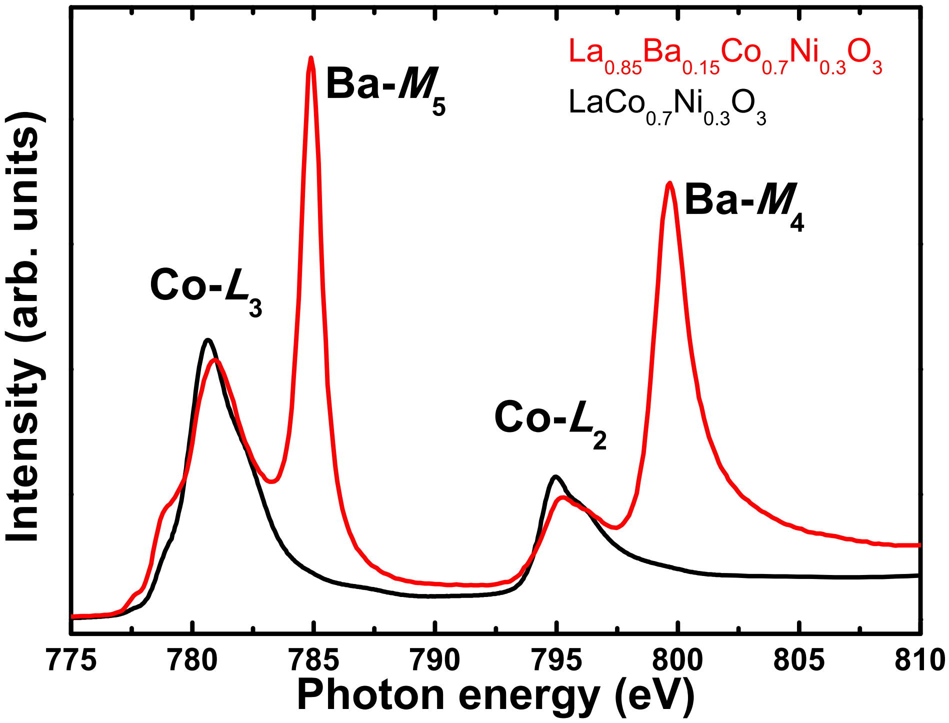

Figure 7.2: XAS measurements of $La_{0.85}Ba_{0.15}Co_{0.7}Ni_{0.3}O_3$ (red line) and $LaCo_{0.7}Ni_{0.3}O_3$ (black line) at Co-$L_{2,3}$ edges. The main peak energy of $La_{0.85}Ba_{0.15}Co_{0.7}Ni_{0.3}O_3$ shifts toward high energy side meaning more Co^{4+} ions in this sample.

sample imply a ferromagnetic interaction that is different from that for the LCNO sample.

In both cases, a fundamental change of magnetic character is observed by these substitutions, even though they might seem minimal at first: isovalent substitution of La by Pr; a small amount of Ba for La. Both systems seem to offer great potential for further, in-depth, and detailed studies of ferromagnetic interaction in novel transition-metal oxides.

Acknowledgements

At the end of this PhD thesis, I give my thanks and appreciation to
- Prof. Dr. H. v. Löhneysen, for enabling this work at the IFP and for being the Reviewer,
- Prof. Dr. M. Le Tacon, for his continuing support at the IFP and for being the Co-Reviewer,
- Dr. S. Schuppler, for delivering the knowledge of the WERA beamline and for valuable input and discussions,
- Dr. M. Merz, for his support and many valuable discussions, for instance on multiplet calculations, and for performing structure refinements,
- Dr. P. Nagel, for introducing me to WERA, for his valuable input, for instance on all beamline aspects, and for his support and many discussions,
- Dr. D. Fuchs, for introducing me to the sol-gel method and for performing SQUID and XRD measurements,
- PD Dr. E. Goering and MPI-IS Stuttgart for the excellent XMCD end station at WERA,
- the Mechanical and the Electronics Workshop at IFP (heads: Mr. Schlenker, Mr. Walz) for their fast and excellent work, and for the reliable delivery of LHe,
- the Electron Spectroscopy Group and the IFP for the good and helpful atmosphere,
- the ANKA Synchrotron Facility and KNMF for the provision of beamtime,
- and my wife Ya-Wen Yang for everything.

Bibliography

[1] J. Zaanen, G. A. Sawatzky, and J. W. Allen, *Phys. Rev. Lett.*, **55**, 418 (1985).

[2] Kichizo Asai, Peter Gehring, Henry Chou, and Gen Shirane, *Phys. Rev. B*, **40**, 10982 (1989).

[3] S. Yamaguchi, Y. Okimoto, and Y. Tokura, *Phys. Rev. B*, **55**, R8666 (1997)

[4] Masatoshi Imada, Atsushi Fujimori, and Yoshinori Tokura, *Rev. Mod. Phys.*, **70**, 1039 (1998).

[5] C. Zobel, M. Kriener, D. Bruns, J. Baier, M. Grüninger, T. Lorenz, P. Reutler, and A. Revcolevschi, *Phys. Rev. B*, **66**, 020402(R) (2002).

[6] Suzanne R. English, J. Wu, and C. Leighton, *Phys. Rev. B*, **65**, 220407(R) (2002).

[7] D. P. Kozlenko, N. O. Golosova, Z. Jirák, L. S. Dubrovinsky, B. N. Savenko, M. G. Tucker, Y. Le Godec, and V. P. Glazkov *Phys. Rev. B*, **75**, 064422 (2007).

[8] N. B. Ivanova, S. G. Ovchinnikov, M. M. Korshunov, I. M. Eremin, N. V. Kazak, *Physics-Uspekhi*, **52**, 789 (2009).

[9] Kichizo Asai, Osamu Yokokura, Nobuhiko Nishimori, Henry Chou, J. M. Tranquada, G. Shirane, Sadao Higuchi, Yuichiro Okajima, and Kay Kohn, *Phys. Rev. B*, **50**, 3025 (1994).

[10] D. N. H. Nam, K. Jonason, P. Nordblad, N. V. Khiem, and N. X. Phuc, *Phys. Rev. B*, **59**, 4189 (1999).

[11] D. N. H. Nam, R. Mathieu, P. Nordblad, N. V. Khiem, and N. X. Phuc, *Phys. Rev. B*, **62**, 8989 (2000).

[12] N. X. Phuc, N. V. Kheim, D. N. H. Nam, *J. Magn. Magn. Mater*, **242-245**, 754 (2002).

[13] M. Merz, P. Nagel, C. Pinta, A. Samartsev, H. v. Löhneysen, M. Wissinger, S. Uebe, A. Assmann, D. Fuchs, and S. Schuppler, *Phys. Rev. B*, **82**, 174416 (2010)

[14] M. W. Haverkort, Z. Hu, J. C. Cezar, T. Burnus, H. Hartmann, M. Reuther, C. Zobel, T. Lorenz, A. Tanaka, N. B. Brookes, H. H. Hsieh, H.-J. Lin, C. T. Chen, and L. H. Tjeng, *Phys. Rev. Lett.* **97**, 176405 (2006).

[15] C. Pinta, D. Fuchs, M. Merz, M. Wissinger, E. Arac, H. v. Löhneysen, A. Samartsev, P. Nagel, and S. Schuppler, *Phys. Rev. B* **78**, 174402 (2008).

[16] A. Posadas, M. Berg, H. Seo, A. de Lozanne, A. A. Demkov, D. J. Smith, A. P. Kirk, D. Zhernokletov, and R. M. Wallace, Appl. Phys. Lett., **98**, 053104 (2011).

[17] D. Fuchs, C. Pinta, T. Schwarz, P. Schweiss, P. Nagel, S. Schuppler, R. Schneider, M. Merz, G. Roth, and H. v. Löhneysen, *Phys. Rev. B*, **75**, 144402 (2007).

[18] S. M. Zhou, L. Shi, J. Y. Zhao, L. F. He, H. P. Yang, and S. M. Zhang, *Phys. Rev. B*, **76**, 172407 (2007).

[19] Y. Wang and H. J. Fan, J. Appl. Phys., **108**, 053917 (2010).

[20] K. Sreedhar, J. M. Honig, M. Darwin, M. McElfresh, P. M. Shand, J. Xu, B. C. Crooker, and J. Spalek, *Phys. Rev. B*, **46**, 6382 (1992).

[21] X. Q. Xu, J. L. Peng, Z. Y. Li, H. L. Ju, and R. L. Greene, *Phys. Rev. B*, **48**, 1112 (1993).

[22] J. K. Vasiliou, M. Hornbostel, R. Ziebarth, and F. J. di Salvo, *J. Solid State Chem.*, **81**, 208 (1989).

[23] P. Lacorre, J. B. Torrance, J. Pannetier, A. I. Nazzal, P. W. Wang, T. C. Huang, and R. L. Siemens, *J. Solid State Chem.*, **91**, 225 (1991).

[24] J. B. Torrance, P. Lacorre, A. I. Nazzal, E. J. Ansaldo, and Ch. Niedermayer, *Phys. Rev. B*, **45**, 8209(R) (1992).

[25] J. L. García-Muñoz, J. Rodríguez-Carvajal, P. Lacorre, and J. B. Torrance, *Phys. Rev. B*, **46**, 4414 (1992).

[26] M. L. Medarde, *J. Phys.: Condens. Matter*, {bf9, 1679 (1997).

[27] M. Medarde, P. Lacorre, K. Conder, F. Fauth, and A. Furrer, *Phys. Rev. Lett.*, **80**, 2397 (1998).

[28] K. Okazaki, T. Mizokawa, A. Fujimori, E. V. Sampathkumaran, M. J. Martínez-Lope, and J. A. Alonso, *Phys. Rev. B*, **67**, 073101 (2003).

[29] G. Catalan, Phase Transitions, **81**:7-8, 729 (2008).

[30] J. A. Alonso, J. L. García-Muñoz, M. T. Fernández-Díaz, M. A. G. Aranda, M. J. Martínez-Lope, and M. T. Casaia, *Phys. Rev. Lett.*, **82**, 3871 (1999).

[31] J. A. Alonso, M. J. Martínez-Lope, M. T. Casaia, J. L. García-Muñoz, and M. T. Fernández-Díaz, *Phys. Rev. B*, **61**, 1756 (2000).

[32] M. Medarde, C. Dallera, M. Grioni, B. Delley, F. Vernay, J. Mesot, M. Sikora, J. A. Alonso, and M. J. Martínez-Lope, *Phys. Rev. B*, **80**, 245105 (2009).

[33] J. A. Alonso, M. J. Martiínez-Lope, I. A. Presniakov, A. V. Sobolev, V. S. Rusakov, A. M. Gapochka, G. Demazeau, and M. T. Fernández-Díaz, *Phys. Rev. B* **87**, 184111 (2013).

[34] M. Viswanathan and P. S. Anil Kumar, *Phys. Rev. B* **80**, 012410 (2009).

[35] K. Asai, O. Yokokura, N. Nishimori, H. Chou, J. M. Tranquada, G. Shirane, S. Higuchi, Y. Okajima, and K. Kohn, *Phys. Rev. B*, **50**, 3025 (1994).

[36] M. Itoh, I. Natori, S. Kubota, and K. Motoya, *J. Magn. Magn. Mater.*, **140-144**, 1811 (1995).

[37] S. Mukherjee, R. Ranganathan, P. S. Anilkumar, and P. A. Joy, *Phys. Rev. B*, **54**, 9267 (1996).

[38] D. Hammer, J. Wu, and C. Leighton, *Phys. Rev. B*, **69**, 134407 (2004).

[39] T. Wu, G. Wu, X. H. Chen, *Solid State Communications*, **145**, 293 (2008).

[40] P. Lacorre, J. B. Torrance, J. Pannetier, A. I. Nazzal, P.W. Wang, and T.C. Huang, J. Solid State Chem., **91**, 225 (1991).

[41] J. Blasco, J. García, *Phys. Rev. B*, **51**, 3569 (1995).

[42] J. Pérez, J. García, J. Blasco, J. Stankiewicz, *Phys. Rev. Lett.*, **80**, 2401 (1998).

[43] J. Androulakis, N. Katsarakis, J. Giapintzakis, J. Appl. Phys., **91**, 9952 (2001).

[44] J. Androulakis, N. Katsarakis, Z. Viskadourakis, J. Giapintzakis, J. Appl. Phys., **93**, 5484 (2003).

[45] Tôru Kyômen, Ryutaro Yamazaki, Mitsuru Itoh, *Phys. Rev. B*, **68**, 104416 (2003).

[46] M. T. Escote, C. H. Westphal, and R. F. Jardim, *J. Appl. Phys.*, **87**, 5908 (2000).

[47] http://www.anka.kit.edu/766.php

[48] P. Willmott, *An Introdcution to Synchrotron Radiation: techniques and applications*, Wiley (2011).

[49] C. T. Chen and F. Sette, *Rev. Sci. Instrum*, **60**, 1616 (1989).

[50] J. Stöhr, Magnetism, Springer (2006).

[51] M. O. Krause. Atomic radiative and raidationless yields for K and L shells. J. Phys. Chem. Ref. Data, **8**, 307 (1979).

[52] J. L. Erskine and E. A. Stern, Calculation of the $\mathrm{M}_{2,3}$ magnetooptical absorption spectrum of ferromagnetic nickel, *Phys. Rev. B*, 12, 5016 (1975).

[53] G. Schütz, W. Wagner, W. Wilhelm, P. Kienle, R. Zeller, R. Frahm, and G. Materlik, Absorption of circularly polarized x rays in iron, *Phys. Rev. Lett.*, 58, 737 (1987).

[54] C. T. Chen, Y. U. Idzerda, H.-J. Lin, N. V. Smith, G. Meigs, E. Chaban, G. H. Ho, E. Pellegrin, and F. Sette, *Phys. Rev. Lett.* **75**, 152 (1995).

[55] B. T. Thole, P. Carra, F. Sette, and G. van der Laan, *Phys. Rev. Lett.* **68**, 1943 (1992).

[56] M. Altarelli, *Phys. Rev. B* **47**, 597 (1993)

[57] P. Carra, B. T. Thole, M. Altarelli, and X. Wang, *Phys. Rev. Lett.* **70**, 694 (1993).

[58] A. Ankudinov and J. J. Rehr, *Phys. Rev. B* **51**, 1282 (1995).

[59] J. Stöhr and H. König, *Phys. Rev. Lett.* **75**, 3748 (1995).

[60] G. Y. Guo, *Phys. Rev. B* **57**, 10295 (1998).

[61] E. C. Stoner, Proc. Roy. Soc. (London) A, **154**, 656 (1936); E. C. Stoner, Proc. Roy. Soc. (London) A, **165**, 372 (1938)

[62] H. W. Brinks, H. Fjellvag, A. Kjekshus, and B. C. Hauback, Journal of Solid state Chemistry, **147**, 464 (1999).

[63] M. T. Escote, A. M. L. da Silva, J. R. Matos, and R. F. Jarkim, Journal of Solid state Chemistry, **151**, 298 (2000).

[64] J. Rodríguez-Carvajal, *FullProf program package*, CPD Newsl. **26**, 12 (2001).

[65] F. M. F. de Groot, J. Electron Spectrosc. Relat. Phenom. **67**, 529 (1994).

[66] A. Tanaka and T. Jo, J. Phys. Soc. Jpn. **63**, 2788 (1994).

[67] Z. Hu, Hua Wu, M. W. Haverkort, H. H. Hsieh, H. -J. Lin, T. Lorenz, J. Baier, A. Reichl, I. Bonn, C. Felser, A. Tanaka, C. T. Chen, and L. H. Tjeng, *Phys. Rev. Lett.* **92**, 207402 (2004).

[68] T. Mizokawa, H. Namatame, A. Fujimori, K. Akeyama, H. Kondoh, H. Kuroda, and N. Kosugi, *Phys. Rev. Lett.*, **67**, 1638 (1991).

[69] R. D. Cowan, *The theory of atomic structure and spectra*, University of California Press, Berkeley, 1981.

[70] M. Abbate, J. C. Fuggle, A. Fujimori, L. H. Tjeng, C. T. Chen, R. Potze, G. A. Sawatzky, H. Eisaki, and S. Uchida, *Phys. Rev. B* **47**, 16124 (1993).

[71] T. Saitoh, T. Mizokawa, A. Fujimori, M. Abbate, Y. Takeda, and M. Takano, *Phys. Rev. B*, **55**, 4257 (1997)

[72] T. Burnus, Z. Hu, M. W. Haverkort, J. C. Cezar, D. Flahaut, V. Hardy, A. Maignan, N. B. Brookes, A. Tanaka, H. H. Hsieh, H.-J. Lin, C. T. Chen, and L. H. Tjeng, *Phys. Rev. B* **74**, 245111 (2006).

[73] S. I. Csiszar, M. W. Haverkort, Z. Hu, A. Tanaka, H. H. Hsieh, H.-J. Lin, C. T. Chen, T. Hibma, and L. H. Tjeng, *Phys. Rev. Lett.* **95**, 187205 (2005).

[74] C. Mitra, Z. Hu, P. Raychaudhuri, S. Wirth, S. I. Csiszar, H. H. Hsieh, H.-J. Lin, C. T. Chen, and L. H. Tjeng, *Phys. Rev. B* **67**, 092404 (2003).

[75] E. Stavitski and F. M. F. de Groot, Micron, **41**, 687 (2010).

[76] M. U. Delgado-Jaime, K. Zhang, J. Vura-Weis, and F. M. F. de Groot, J. Synchrotron Rad., **23**, 1264 (2016).

[77] B. T. Thole and G. van der Laan, Europhys. Lett. **4**, 1083 (1987).

[78] B. T. Thole, G. van der Laan, and P. H. Butler, Chem. Phys. Lett. **149**, 295 (1988).

[79] G. van der Laan, B. T. Thole, G. A. Sawatzky, and M. Verdaguer, *Phys. Rev. B*, **37**, 6587 (1988).

[80] F. M. F. de Groot, J. C. Fuggle, B. T. Thole, and G. A. Sawatzky, *Phys. Rev. B*, **42**, 5459 (1990).

[81] F. M. F. de Groot, J. Electron Spectrosc. Relat. Phenom., **62**, 111 (1993).

[82] F. M. F. de Groot, Coord. Chem. Rev., **249**, 31 (2005).

[83] http://abulafia.mt.ic.ac.uk/shannon/ptable.php

[84] R. D. Shannon, Acta Crystallogr, **32**, 751 (1976).

[85] T. Wu, G. Wu, and X. H. Chen, *Solid State Communications*, **145**, 293 (2007).

[86] D. Sarma, N. Shanthi, and P. Mahadevan, *Phys. Rev. B*, **54**, 1622 (1996).

[87] F. M. F. de Groot, Coordination Chemistry Reviews, **249**, 31 (2005).

[88] S. Medling, Y. Lee, H. Zheng, J. F. Mitchell, J. W. Freeland, B. N. Harmon, and F. Bridges, *Phys. Rev. Lett.*, **109**, 157204 (2012).

[89] M. Merz, D. Fuchs, A. Assmann, S. Uebe, H. v. Löhneysen, P. Nagel, and S. Schuppler, *Phys. Rev. B*, **84**, 014436 (2011).

[90] S. Medling, Y. Lee, H. Zheng, J. F. Mitchell, J. W. Freeland, B. N. Harmon, and F. Bridges, *Phys. Rev. Lett.*, **109**, 157204 (2012).

[91] M. Abbate, F. M. F. de Groot, J. C. Fuggle, A. Fujimori, O. Strebel, F. Lopez, M. Domke, G. Kaindl, G. A. Sawatsky, M. Takano, Y. Takeda, H. Eisaka, and S. Uchida, *Phys. Rev. B* **46**, 4511 (1992).

[92] A. R. Moodenbaugh, B. Nielsen, Sharadha Sambasivan, D. A. Fischer, T. Friessnegg, S. Aggarwal, R. Ramesh, and R. L. Pfeffer, *Phys. Rev. B* **61**, 5666 (2000).

[93] C. T. Chen and F. Sette, *Phys. Scr.*, T **T31**, 119 (1990).

[94] C. Mitra, Z. Hu, P. Raychaudhuri, S. Wirth, S. I. Csiszar, H. H. Hsieh, H.-J. Lin, C. T. Chen, and L. H. Tjeng, *Phys. Rev. B*, **67**, 092404 (2003).

[95] Burnus, Z. Hu, H. H. Hsieh, V. L. J. Joly, P. A. Joy, M. W. Haverkort, H. Wu, A. Tanaka, H.-J. Lin, C. T. Chen, and L. H. Tjeng, *Phys. Rev. B*, **77**, 125124 (2008).

[96] R. H. Potze, G. A. Sawatzky, and M. Abbate, *Phys. Rev. B*, **51**, 11501 (1995).

[97] C. Piamonteze, F. M. F. de Groot, H. C. N. Tolentino, A. Y. Ramos, N. E. Massa, J. A. Alonso, and M. J. Martínez-Lope, *Phys. Rev. B*, **71**, 020406(R) (2005).

[98] V. Kumar, R. Kumar, D. K. Shukla, S. Gautam, K. H. Chae, and R. Kumar, J. Appl. Phys., **114**, 073704 (2013).

[99] V. Kumar, R. Kumar, D. K. Shukla, S. K. Arora, I. V. Shvets, K. Singh, and R. Kumar, Material Chemistry and Physics, **147**, 617 (2014).

[100] T. Kyomen, R. Yamazaki, and M. Itoh, *Phys. Rev. B*, **68**, 104416 (2003).

[101] J. B. Goodenough and J.-S. Zhou, J. Mater. Chem. **17**, 2394 (2007)

[102] I. A. Nekrasov, S. V. Streltsov, M. A. Korotin, and V. I. Anisimov, *Phys. Rev. B*, **68**, 235113 (2003).

[103] P. G. Radaelli and S.-W. Cheong, *Phys. Rev. B*, **66**, 094408 (2002).

[104] A. M. Durand, D. P. Belanger, C. H. Booth, F. Ye, S. Chi, J. A. Fernandez-Baca, and M. Bhat, J. Phys.: Condens. Matter, **25**, 382203 (2013).

[105] D. Fuchs, C. Pinta, T. Schwarz, P. Schweiss, P. Nagel, S. Schuppler, R. Schneider, M. Merz, G. Roth, and H. v. Lhneysen, *Phys. Rev. B*, **75**, 144402 (2007).

[106] D. Fuchs, E. Arac, C. Pinta, S. Schuppler, R. Schneider, and H. v. Lhneysen, *Phys. Rev. B*, **77**, 014434 (2008).

[107] J. Igarashi and K. Hirai, *Phys. Rev. B* **50**, 17820 (1994).

[108] Virat V. Mehta, Shameek Bose, Jodi M. Iwata-Harms, Elke Arenholz, C. Leighton, and Y. Suzuki, *Phys. Rev. B*, **87**, 020405(R) (2013).